DEVELOPMENT OF 2-3 MM PROTON MINIBEAMS AS A NEW FORM OF GRID RADIOTHERAPY

A Dissertation
Presented to
The Academic Faculty

By

Serdar Charyyev

In Partial Fulfillment
of the Requirements for the Degree
Doctor of Philosophy in the
School of Mechanical Engineering
Department of Nuclear and Radiological Engineering

Georgia Institute of Technology

August 2019

DEVELOPMENT OF 2-3 MM PROTON MINIBEAMS AS A NEW FORM OF GRID RADIOTHERAPY

Approved by:

Dr. C.-K. Chris Wang, Advisor
School of Mechanical Engineering
Georgia Institute of Technology

Dr. Anna Erickson
School of Mechanical Engineering
Georgia Institute of Technology

Dr. Nolan Hertel
School of Mechanical Engineering
Georgia Institute of Technology

Dr. Mark Artz
Department of Radiation Oncology
University of Florida

Dr. Liyong Lin
Department of Radiation Oncology
Emory University

Dr. Mark McDonald
Department of Radiation Oncology
Emory University

Date Approved: June 3, 2019

When you buy something, you're not paying money for it. You're paying with the hours of your life you had to spend earning that money. The difference is that life is one thing money can't buy. Life only gets shorter, and it is pitiful to waste one's life and freedom that way.

Jose Mujica

Dedicated to my Father

Izbasar Charyyev

ACKNOWLEDGEMENTS

I would first like to thank my advisor, Dr. C.-K. Chris Wang, for his strong support and guidance during my Ph.D. years. His insights have been pivotal in my development and confidence as a researcher.

I would like to thank my Ph.D. Dissertation Reading Committee for partaking in this academic journey with me. I thank each of them for their patience and giving me much needed support.

To my lab-mate, Gregory Szalkowski, thanks for the fun and support. I greatly look forward to having you as a colleague in the years ahead.

To my parents, Tavus and Izbasar, and my siblings, Suray and Batyr, I could never fully express my gratitude for all of their love and sacrifice. Their prayers, understanding and support have meant more than they can imagine.

I am blessed to have Seher, love of my life, and my daughter, Sara, who have been my strongest motivation to complete this task. It has been bumpy at times, but your confidence in me has enhanced my ability to get through it all and succeed in the end. Thank you and I love you.

TABLE OF CONTENTS

LIST OF TABLES

LIST OF FIGURES

SUMMARY

In this study, we investigated, computationally and experimentally, the feasibility of a new form of proton GRID therapy based on an array of proton minibeams developed at the existing proton therapy clinics. The diameter of the proton minibeams is in the range of 2-3 mm. The purpose of this new form of proton GRID therapy is to further enhance normal tissue sparing during the treatment. The optimal design of the proton minibeam array is based on the figures-of-merit (FOM) parameters including the peak-to-valley dose ratio (PVDR), dose rate at the Bragg peak and the unwanted neutron dose. Using Monte Carlo code TOPAS we simulated proton pencil-beams that mimic those available at cyclotron-based clinical facilities. We achieved parallel beams of 2-3 mm diameter using physical collimator made of dense materials such as brass and tungsten. The beams are produced via the open holes of the collimator. The spatial pattern of the beam array follows the hexagonal arrangement. We optimized the proton minibeam design by considering different combinations of parameters including beam size, collimator material, center-to-center (c-t-c) distance, phantom to collimator distance (air gap), and collimator thickness (t). Verification measurements of the PVDRs using radiochromic films and neutron dose using WENDI-II neutron detector were conducted at two proton therapy facilities: the University of Florida Proton Therapy Institute (UFPTI) and the Emory Proton Therapy Center (EPTC). The results show that using the existing proton pencil beam scanning (PBS) technique, the optimized proton minibeams can achieve high PVDR values at the entrance of the water phantom and at the same time maintain clinically acceptable dose rates at the tumor depth. Even though the neutron dose increases by 20-30 folds (on average) with the use of a collimator, it is still less than the neutron dose produced with double scattered proton beam and measures in the order of a few mSv. Accordingly, the results suggest that it is feasible to develop an array of proton minibeams at the existing proton therapy clinics to further enhance normal tissue sparing during the treatment.

CHAPTER 1
INTRODUCTION AND BACKGROUND

1.1 GRID Therapy

GRID radiation therapy is a spatially fractionated radiation therapy (SFRT) which was first developed in Germany by Alban Kohler in 1909 to minimize adverse radiation effects to the skin when irradiating deep-seated tumors [1]. In this technique, special collimator is utilized to collimate broad x-ray radiation into multiple beams in a grid-like array, Figure 1.1.

Conventionally, the aim in SFRT, when performed with X-rays, is to spare normal tissue by depositing the dose in spatially fractionated manner and to de-bulk very large tumors for purposes of shrinking the malignancy or palliation. When SFRT is performed with protons, on top of the normal tissue sparing, it is also possible to deliver homogeneous dose to the tumor volume for an effective tumor kill and control.

The aim in SFRT is to spare normal tissue by depositing the dose in spatially fractionated manner, but at the same time deliver homogeneous dose to the tumor volume. One of the metrics of how good the aim of SFRT is achieved is a quantity called peak-to-valley-dose ratio (PVDR), discussed in more detail in Chapter 3. It has been shown that high PVDR and low valley doses are necessary to spare normal tissue [2]. The homogeneity of the dose necessitates the PVDR value of one in the tumor volume; even though this is open to discussion because a good tumor control has been achieved even with heterogeneous dose distribution [3, 4].

More than two decades later, unaware of Kohler's work, Dr. Liberson of U.S. Marine Hospitals in New York used GRID therapy to treat small animals and some inoperable tumors and also noticed increased skin tolerance [5].

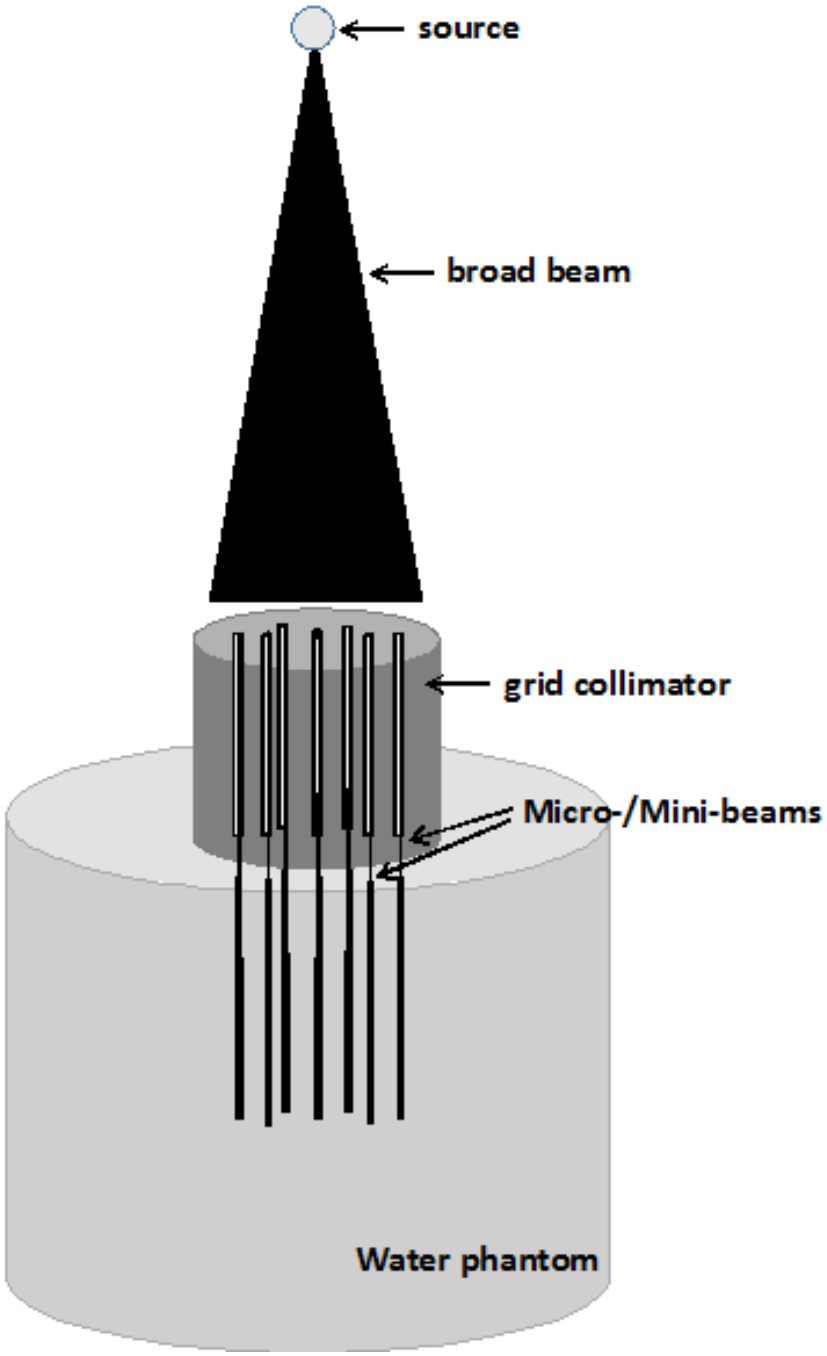

Figure 1.1: GRID irradiation.

Pioneering work in GRID therapy involved using perforations of different shapes (circular, rectangular, oval) ranging from few millimeters to a centimeter width opened in lead sheets [6, 7]. These investigations addressed only one problem associated with orthovoltage treatments of that time: skin sparing. Therefore, GRID therapy was disparaged.

With the advent of megavoltage radiotherapy and the introduction of linear accelerators (Linacs) into clinical practice in the 1970s, skin sparing was no longer a major problem, but this time radiotherapy was confronted with new challenges: normal tissue tolerance of other organs like lung, brain and intestines [8]. These new challenges revived GRID therapy. A group of researchers developed a grid therapy concept that could be used with megavoltage radiotherapy [9]. They used a specially designed Cerrobend grid matrix which can be fitted into the tray holder of commercially available Linacs. Using 6 MV or 25 MV photons, they treated 72 patients with advanced bulky tumors ($\geq$8 cm diameter) for palliative response. They proved GRID therapy is an effective method of delivering large single doses for palliative treatment.

1.2 Radiobiology of GRID Therapy

Basis for using small and spatially-fractionated radiation beams to achieve higher normal tissue sparing is associated with the dose-volume effect, a finding which sets forth an idea that normal tissue can tolerate higher doses when smaller tissue volumes are irradiated. This phenomenon has been known since 1960s, when Zeman et al. investigated possible hazards of heavy cosmic rays to astronauts' brain. They irradiated mice brain with energetic deuterons and evaluated threshold dose to produce necrotic lesions. The dose required to produce a threshold lesion in the mouse brain increased from 300 Gy with a beam of 1 mm diameter to 11 000 Gy with a beam of 25 μm diameter [10].

Several other investigations are remarkable in showing that the tolerance of organs to radiation increases with decreasing beam sizes. Experiments on rats [11, 12, 13], pigs [14, 15] and dogs [16] have demonstrated the dose-volume effect. Figure 1.2 (A) shows data for

pig skin, where, acute skin ulceration and dermal thinning are the biological end-points. As shown, dose tolerance rises steeply for source diameters below 8 mm. Figure 1.2 (B) shows data for rat spinal cord. In this case, white matter necrosis is the end-point. Data shows that there is a steep increase in dose tolerance if the segment of irradiated cord length is below 10 mm [14].

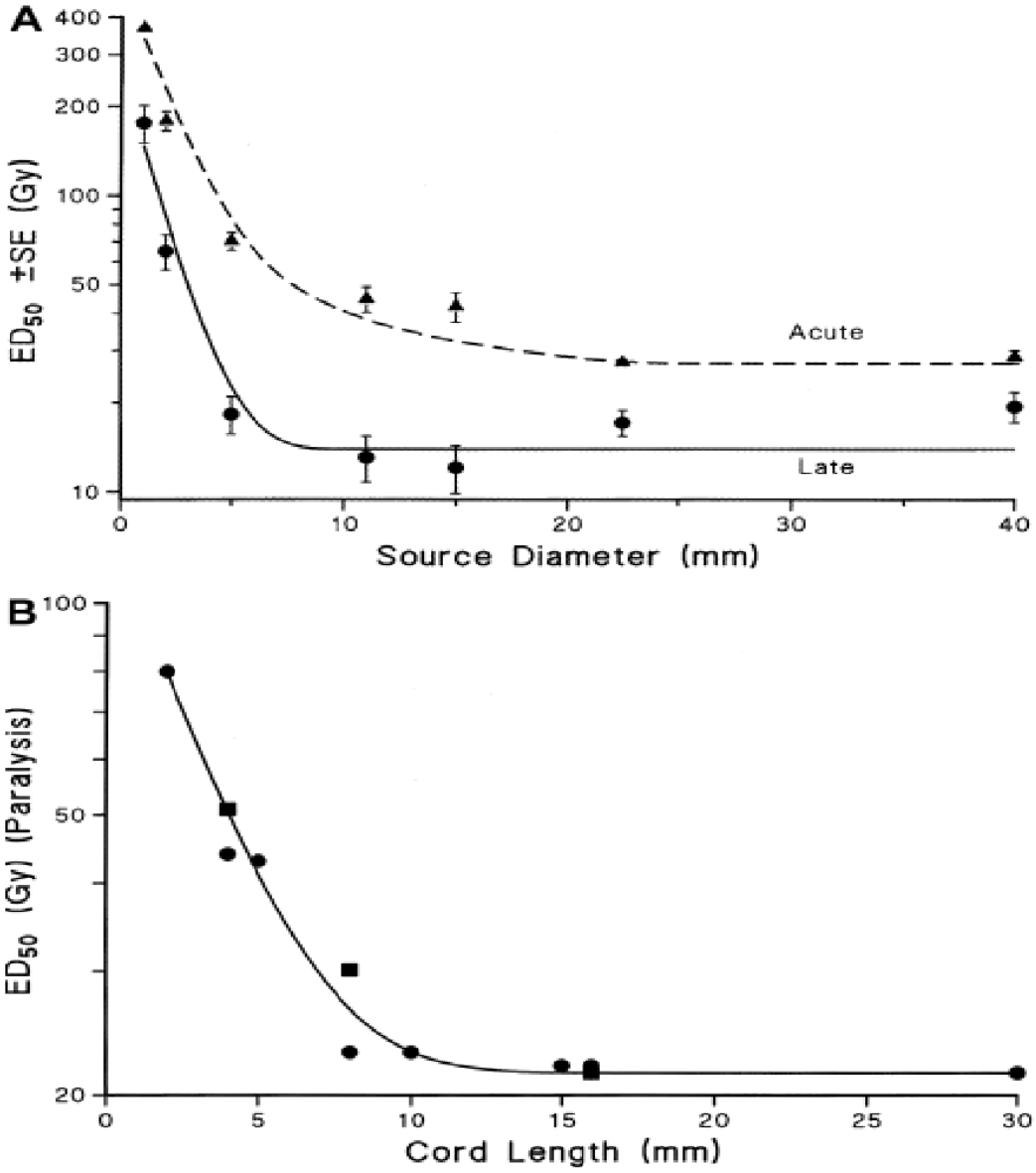

Figure 1.2: (A) Data for pig skin. Acute skin ulceration and dermal thinning are biological end-points. (B) Data for rat spinal cord. Paralysis is the end-point. ED_{50} is the radiation dose at which the biological end-points are observed in 50% of the treated animals.

The biological processes responsible for the dose-volume effect are still being investigated, with several possible causes.

One of the explanations supports that there is a limited migration capability of undamaged cells, about 2 mm. That is, the undamaged cells can migrate short distances and replace the nearby dead cells [14, 17, 18].

Another possible explanation for the dose-volume effect is the stem-cell depletion hypothesis: for each organ it exists a limiting critical volume, which can be repopulated by a single surviving stem cell and for which damage can be repaired by re-population [19].

A special type of bystander effect might be responsible for increased survival of the cells receiving high dose of radiation, when nearby cells receive a low dose [20].

In addition to mentioned hypotheses, several other studies support differential effects of microbeam irradiation on the vasculature of the tumors and of normal tissues [21, 22], existence of differential regulation of genetic pathways involved in microbeam and broad beam irradiation [23] and even, seemingly, the change of genetic profile of cells and tissues after microbeam irradiation [24].

While the biological basis of the dose-volume effect is not fully understood, there is a motivation for researchers to further exploit its benefits in the form of GRID therapy.

1.3 Microbeam, Minibeam and Conventional GRID Radiation Therapy

As a direct consequence of what has been discussed in the Section 1.2, beam sizes generated for SFRT vary greatly from 25 μm to 1 cm, depending on how they are generated and/or what is being treated. To help review the published studies for various forms of SFRT, it is convenient to divide the studies into three sub categories: microbeam radiation therapy (MRT), minibeam radiation therapy (MBRT) and conventional SFRT (GRID).

MRT was initiated in the first half of 1990s in Brookhaven National Laboratory (BNL) and later developed at the European Synchrotron Radiation Facility (ESRF) after mid-1990s. MRT uses an array of synchrotron radiation microbeams of width 25-100 μm sep-

arated by 100-300 μm center-to-center (c-t-c) distances [25]. Beams of these sizes offer maximal use of the dose-volume effect. Healthy tissue sparing is outstanding with MRT [26]. High flux of synchrotron radiation allows very high dose rates, up to several hundreds of Grays per second. Despite these advantages, to prevent smearing from cardiosynchronous or pulmonary pulsations, very high radiation fluxes are necessary. These high fluxes are achievable with synchrotron based facilities, a practical limitation for clinical implementation. Furthermore, very high technical precision is required to deliver desired dose to the tumor using beams of order of microns.

Therefore, as an extension to MRT, researchers from BNL proposed MBRT [27]. MBRT uses minibeams of width 0.2-1 mm separated by 1-4 mm c-t-c distances. Despite higher healthy tissue damage as compared to MRT, entrance doses of up to several hundred Grays were tolerated in rat brain [27, 28]. In another front, using MBRT, researches have shown gain of three-fold in mean survival time of 9L gliosarcoma bearing-rats with respect to control group [29]. SFRT using beams of sizes of several millimeters to 1 cm, so-called conventional GRID, has been performed historically as discussed previously [1, 5, 6, 7].

1.4 Spatially fractionated radiation therapy with protons

SFRT using protons is a fairly new technique. While no human studies have been conducted with such a technique, animal studies as well as studies on proton beam designs have been widely reported [30, 31, 32, 33, 34, 35, 36, 37, 38, 39, 40, 41, 42]. Protons offer negligible dose deposition at the distal end of the tumor owing to the fact that they have limited range. Due to multiple the Coulomb scattering in the medium, protons can produce homogeneous dose distribution in the tumor, even though they are spatially separated at shallower depths. Owing to their ballistic properties, less integral dose and well-defined regions of high and low dose can be achieved with protons. Denser ionizations and complex DNA damage in Bragg peak region characterized by higher relative biological effectiveness (RBE) are just some of the biological advantages of protons. All of these and others make protons

attractive candidate for SFRT.

SFRT studies with protons at micrometer range, so-called microbeam radiation therapy with protons, pMRT, have been done and the results comparable to those of X-ray MRT have been obtained [30, 31].

Studies on proton beam sizes of 0.3-0.7 mm, have also been published in the last 4-5 years. Prezado and Fois performed an extensive Monte Carlo (MC) simulation study and showed the proof-of-concept of the minibeam radiation therapy with protons, pMBRT, of 0.7 mm width [32]. Experimental dosimetry studies were performed in U.S.A using 0.3 mm pristine proton minibeams from synchrotron and in Europe using 0.4-0.7 mm wide proton minibeams [33, 34]. The latter is noteworthy, because it was one of the earliest, if not first, experimental studies performed with a cyclotron accelerated protons by a commercially available machine. Very recently, an animal study with Fischer 344 rats showed that proton minibeams of width 0.4 mm produced by cyclotron spares normal rat brain [35].

New trending technique in SFRT with protons is utilizing the spot scanning ability of cyclotron based machines readily available in clinics. Dosimetry studies with such technique demonstrated that pencil beams can be used to create grid-like pattern [36, 37, 38, 39, 40]. All of these studies, except for De Marzi et al. [41], and Charyyev et al. [40], use pencil beams from the existing proton therapy machines without additional collimation. Despite the efforts [39], beam size achievable with pencil beams from proton machine without any additional collimation is around 1 cm; as such, additional collimation is required to obtain even smaller beam sizes and to maximize the dose-volume effect.

The first attempt to show that the use of physical collimator to obtain minibeams from proton pencil beams was semi-successful [41]; it was successful in terms of achieving the desired PVDR values, unsuccessful because the dose rate was too low to be practical for clinical use. We postulate that using millimeter minibeams will still significantly improve normal tissue tolerance as evidenced by literature [35] and at the same time retain a dose rate high enough for clinical use. Therefore, the findings of this investigation may lead to

a new form of proton-minibeam-based GRID therapy.

CHAPTER 2

RESEARCH OBJECTIVES AND APPROACH

The main objective of this study is to develop and to test an array of proton minibeams of 2-3 mm diameter based on the existing proton pencil beam scanning (PBS) system. What is meant here with 2 and 3 mm diameter, is really the diameter of the holes opened in the physical collimator. The end goal is to implement these minibeams as a new form of GRID therapy at the existing proton therapy clinics.

The scope of this work is fundamentally similar to the existing GRID therapy methods in that it uses grid-like pattern for spatial fractionation. However, there are considerable differences of the proposed work from the state of the art. Specifically, they include: the employment of 2-3 mm minibeams, the use of proton pencil beam, the use of physical collimator having a hexagonal pattern of open holes, and the use of proton beams from cyclotron based proton therapy machines.

To further enhance normal tissue sparing, beam sizes, in theory, should be as small as possible, but sizes of 2-3 mm were deemed optimal for several reasons: a) beamlet width should not be smaller than the setup error and beam-delivery accuracy, b) cardiopulmonary pulsations of a patient interfere with dose distribution, c) it is easier to produce millimetric beamlets as compared to micrometric beamlets, d) dose rate will be higher and treatment time will be shorter with 2-3 minibeams as compared to microbeams, e) from proton beam economy viewpoint, less protons will be wasted and less collimator material is activated, i.e. less production of unwanted neutrons, and f) for very narrow beams, the entrance dose becomes substantially high, so much so that it greatly exceeds the Bragg peak dose. This effect is due to reduction in in-scatter leading to a loss of charged particle equilibrium [42]. This effect essentially nullifies the desirable dose profile of protons with depth.

Since full width at half maximum (FWHM) of currently available proton therapy ma-

chines is in the range of 1-2 cm at isocenter [36], additional collimation will be required to obtain minibeams of 2-3 mm. Therefore, the task of designing and optimizing the collimator with respect to the figures-of-merit (FOM) quantities gains the utmost importance in this project.

The FOM quantities include the peak-to-valley dose ratio (PVDR), the dose rate at the Bragg peak and the unwanted neutron dose. Each of these quantities will be affected by design parameters like collimator material, hole diameter (beamlet width), beam energy, center-to-center (c-t-c) distance, collimator thickness (t) and phantom to collimator distance (air gap). The design parameters picked for initial consideration in this study and their values are summarized in Table 2.1.

Table 2.1: Proton minibeam design parameters used in this study and their corresponding values.

Parameter	Values
Collimator material	Tungsten, Brass
Collimator hole diameter (d)	2 mm and 3 mm
Center-to-center distance (c-t-c)	4, 6, 8 mm for 2 mm hole
	6, 9, 12 mm for 3 mm hole
Beam energy	100, 120 and 150 MeV
Phantom to collimator distance (air gap)	5, 7, 10 and 20 cm
Collimator thickness	3.25 and 6.5 cm

Since the set of design parameters shown in Table 2.1 involves complex geometry, we deem it necessary to employ the Monte Carlo code TOPAS to carry out the design calculations. The plan was to use the results obtained from the MC calculations to reduce the number of design parameter combinations, which will then be used for experimental verification.

The main tasks of this project are:

1. To assess the PVDRs of the proposed proton minibeams at different depths in water phantom
    (a) To use the TOPAS code to simulate the hexagonal array of proton minibeams and to obtain the PVDRs at different depths in a solid water phantom
    (b) To assess how the simulated PVDR results vary with varying physical parameters for a single energy layer and Spread-Out-Bragg-Peak (SOBP) scenario
    (c) To perform verification measurements of the simulated PVDR results with the IBA universal nozzle (Ion Beam Applications SA, Louvain-la-Nueve, Belgium) and the ProBeam (Varian Medical Systems, Inc., Palo Alto, CA) PBS systems
2. To assess the dose rate of the proton minibeams at the Bragg peak
    (a) To use the simulated results to determine the dose ratio of the collimated minibeam to the uncollimated beam at the Bragg peak, and to assess how it varies with physical parameters for a single energy layer
    (b) To perform a verification measurement of the dose ratio with the IBA and the ProBeam PBS systems
3. To assess the additional unwanted neutron dose produced by the physical collimator
    (a) To use the TOPAS code to simulate the proton minibeam setup and to calculate the ambient neutron dose equivalent ($H^*(10)$) per proton treatment dose
    (b) To assess how the ambient neutron dose equivalent changes with varying physical parameters for a single energy layer and SOBP scenario
    (c) To measure the ambient neutron dose equivalent with WENDI-II neutron rem meter at the Emory University's proton therapy center

The details for each of the three tasks are presented, respectively, in Chapters 3, 4, and 5.

CHAPTER 3

ASSESSMENT OF PEAK-TO-VALLEY DOSE RATIOS

This chapter first describes the computation and the measurement methods used to assess the PVDRs of the proposed proton minibeams in a water phantom. It then presents and discusses the results obtained from both methods.

3.1 Peak-to-valley dose ratio

The peak-to-valley dose ratio is a relevant metric of how good a GRID therapy can be achieved. It can be illustrated by Figure 3.1.

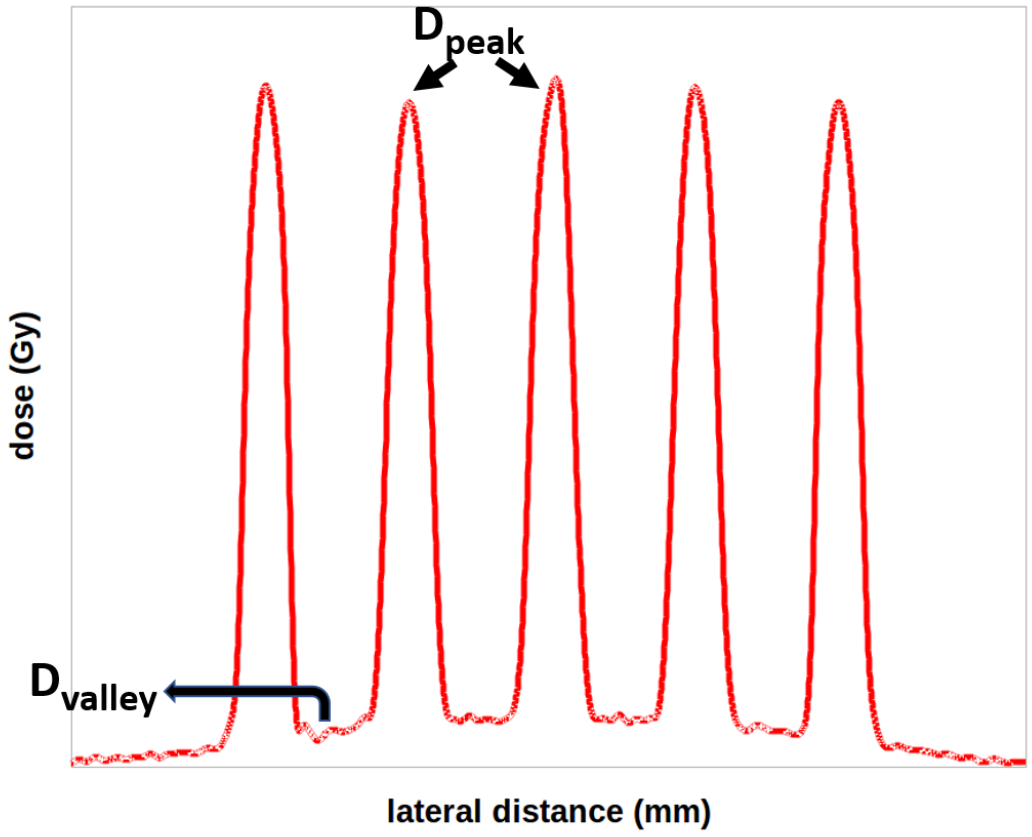

Figure 3.1: The lateral dose profile of an array of minibeams.

As shown, the lateral dose profile of an array of minibeams in GRID therapy at a given depth consists of areas of high dose, i.e. peaks, (corresponding to open holes) and areas of low dose, i.e. valleys (corresponding to areas blocked by septa). The distance between two neighboring peaks is called center-to-center (c-t-c) distance. The PVDR is defined as the ratio of the peak dose (D_{peak}) to the valley dose (D_{valley}), i.e. $PVDR = \frac{D_{peak}}{D_{valley}}$.

In a radiotherapy treatment, it desirable to have high PVDRs anywhere outside the tumor volume and to have a PVDR approaching unity in the tumor volume. Since the PVDR depends on physical parameters like energy of the beam, diameter of the hole in the collimator, c-t-c distance, collimator thickness and air gap, lateral profiles of the minibeams were simulated after passing through the collimator at different depths in a water phantom and the dependence of PVDR on each of the mentioned physical parameters was reported.

3.2 Monte Carlo simulations with TOPAS

3.2.1 TOPAS

In this study, a Monte Carlo particle transport code, TOol for PArticle Simulation (TOPAS), version 3.1.p2, was used to simulate the proton transport [43]. TOPAS was created through collaboration of the researchers at SLAC National Accelerator Laboratory, Massachusetts General Hospital and the University of California at San Francisco for proton therapy applications. Now, it is available for use in all areas of radiation therapy research.

TOPAS uses Geant4 libraries with an easy to use parameter system file to make advanced Monte Carlo simulations of all forms of radiotherapy easier to use for medical physicists. Parameters like geometry, source definition, scoring, time features and many more can be controlled via simple text files without the need to write complex C++ code. Explanation of a sample parameter file in detail and input parameters used in this project are included in Appendices A and B.

3.2.2 Proton pencil beam source

TOPAS accurately predicts dose distributions in a variety of geometries in the energy range which was used in this project and it has been validated numerous times [44, 45]. Modeling the proton source is one of the most important tasks in this project. Even though the profile of the beam changes after passing through the collimator, it is crucial to model the proton source before the collimator as accurately as possible for the most reliable results. Pencil beam characteristics like spatial beam spread, angular divergence, coefficient of correlation and energy spread were modeled according to the methods described by Huang et al [46].

The source parameters were extracted and tuned at the nozzle exit with a series of six different commissioning measurements. The geometry of the source plane is set up such that the source is on the positive z-axis and isocenter is at origin. We can parametrize the source model at the source plane at any location along the z-axis. The parameters required to define the source in x-direction are: the spatial beam spread distribution (beam spot size), σ_x, the angular spread distribution (beam divergence), $\sigma_{x\theta}$, and the coefficient of correlation, ρ_x. The same set of parameters is needed for the y-direction.

According to Courant-Snyder's particle transportation theory [47], the σ-matrix of a beam's parameters at any location Z along the beam path, neglecting dissipation and diffusion processes, can be described as in Equation 3.1.

$$\begin{bmatrix} \sigma_x^2 & \rho_x\sigma_x\sigma_{x\theta} \\ \rho_x\sigma_x\sigma_{x\theta} & \sigma_{x\theta}^2 \end{bmatrix}_{z=Z} = \begin{bmatrix} 1 & -Z \\ 0 & 1 \end{bmatrix} \begin{bmatrix} \sigma_x^2 & \rho_x\sigma_x\sigma_{x\theta} \\ \rho_x\sigma_x\sigma_{x\theta} & \sigma_{x\theta}^2 \end{bmatrix}_{z=0} \begin{bmatrix} 1 & -Z \\ 0 & 1 \end{bmatrix}^T \tag{3.1}$$

which implies that the variance of the spot size along the beam path should satisfy the Equation 3.2.

$$\sigma_x^2(Z) = \sigma_x^2(0) - 2\rho_x(0)\sigma_x(0)\sigma_{x\theta}(0)Z + \sigma_{x\theta}^2(0)Z^2 \tag{3.2}$$

Therefore, one needs to know σ_x, $\sigma_{x\theta}$, ρ_x at Z=0 (isocenter) to get σ_x at any Z. In order to

do that, the spot profile information of both IBA and ProBeam systems were obtained.

3.2.3 Pencil beam model of the IBA

For the IBA, the spot profiles at six locations in air along the Z-axis (455, 330, 200, 100, 0 and -100 mm) were acquired using a scintillation detector (Lynx IBA dosimetry, Germany) with 0.5-mm resolution for proton energies from 100 to 220 MeV in 10-MeV increments. By fitting the spot size from measurements with Equation 3.2, σ_x, $\sigma_{x\theta}$, and ρ_x at Z=0 (isocenter) were derived.

To obtain the coefficient of correlation, ρ_x , at any Z, the following equation, Equation 3.3, can be used which follows directly from the Equation 3.1

$$\rho_x(Z) = \frac{\rho_x(0)\sigma_x(0) - \sigma_{x\theta}(0)Z}{\sigma_x(Z)} \tag{3.3}$$

Even though the $\sigma_{x\theta}$ slightly increases in air due to multiple Coulomb scattering, we approximated the $\sigma_{x\theta}$ as constant in air between the nozzle exit and the phantom surface and utilized it with that assumption in Equation 3.3.

Even though a single beam was simulated through the collimator, the collimator had all 45 perforations in place to allow some of the beam particles to pass through other holes.

The beam energy spread of the source was also described by a Gaussian distribution with standard deviation, sigma, defined in terms of a percentage of the mean energy value, adjusted to reproduce the measured depth-dose distribution in water. Beam energy spread is unitless and the coding in TOPAS is given as:

$$\begin{aligned} &fEnergySpread = BeamEnergySpread * fEnergy/100.; \\ &p.kEnergy = CLHEP :: RandGauss :: shoot(fEnergy, fEnergySpread); \end{aligned} \tag{3.4}$$

So, for example, if a spread of 0.2 MeV is required with an energy of 153 MeV, the

beam energy spread should be set to:

$$0.2MeV/153MeV * 100 = 0.13 \tag{3.5}$$

The beam energy spread for the energy values used in this project is given in Table 3.1. The choice of these energies was based on the availability in the clinical machine on which these measurements were performed and also the wide range of depths those energies cover.

Table 3.1: Beam energy spread for the energy values used in this project, UFPTI

Beam energy in MeV	Beam Energy Spread
100	0.7116
120	0.6687
150	0.6291

For PVDR simulations, relative dosimetry was performed and therefore number of protons per monitor unit (MU) was not considered.

3.2.4 Pencil beam model of the ProBeam

The pencil beam of the ProBeam system, was modeled using the same technique that was used for the IBA system. The Emory's ProBeam machine is a newer machine and has different phase space parameters (σ_x, $\sigma_{x\theta}$, and ρ_x) and energy spread than that of the IBA's. The energy spread values for the ProBeam are as shown in Table 3.2.

Table 3.2: Beam energy spread for the energy values used in this project, EPTC

Beam energy in MeV	Beam Energy Spread
100	1.2214
120	1.0939
150	0.8403

3.2.5 Geometry

The geometric configuration included in TOPAS to simulate the experimental setup is shown in Figure 3.2.

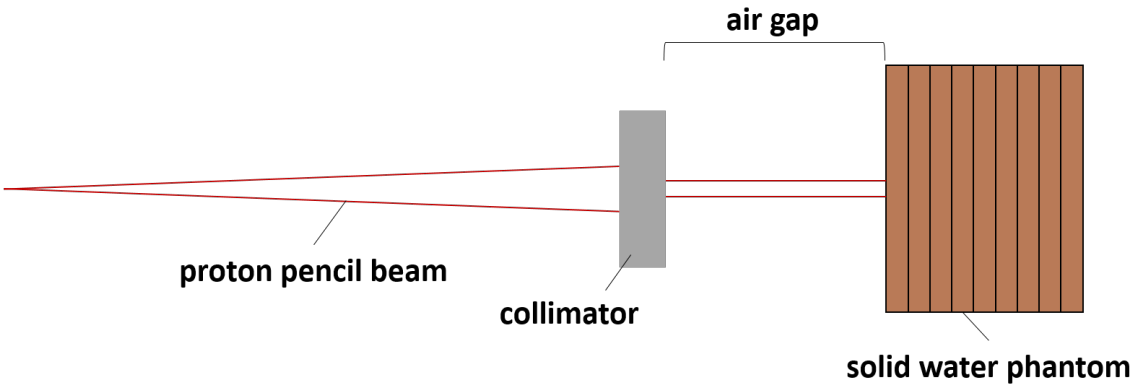

Figure 3.2: The geometric configuration used in TOPAS simulations.

As summarized in Table 2.1, the thickness of the collimator is either 3.25 or 6.5 cm. Air gap varies as 5, 7, 10 or 20 cm. Solid water phantom is a cube which measures 30 x 30 x 30 cm^3 in x, y and z directions respectively.

Figure 3.3a shows the cross-sectional and side (Figure 3.3b) views of the collimator. The collimator was designed out of dense material and the spatial pattern of the holes follows a hexagonal arrangement. Simulations were run with c-t-c distances of 4, 6, 8 mm for 2 mm hole and 6, 9, 12 mm for 3 mm hole. The collimator materials include brass and

tungsten.

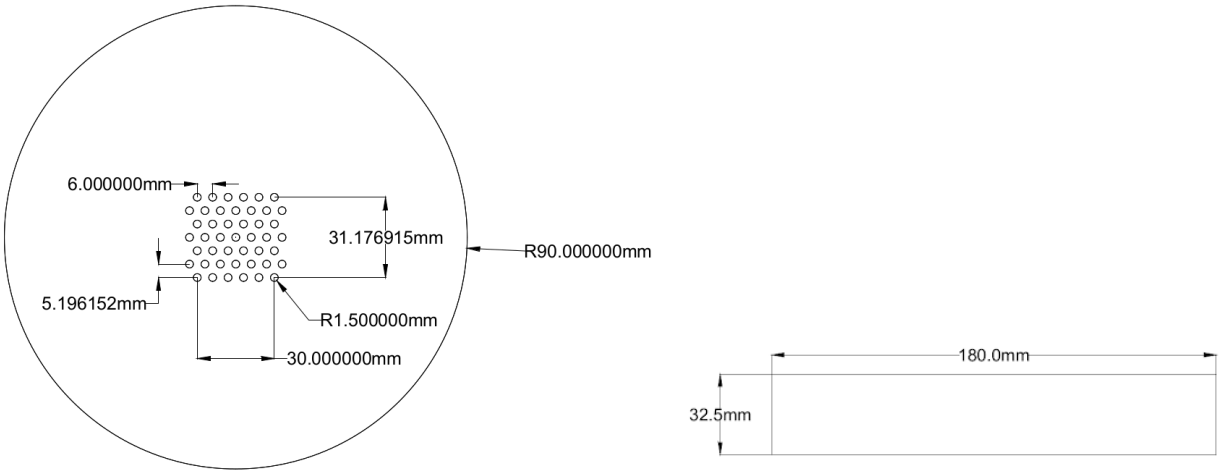

(a) Cross-sectional view (b) Side view

Figure 3.3: Cross-sectional and side views of the collimator

3.2.6 Scoring

The volume scorer "$DoseToMedium$" tool within TOPAS was used to score the dose distribution in the water phantom. This tally gives the sum of energy deposits divided by mass in units of Gray (Gy). The tally volume is a rectangular prism with measurements 10 x 10 x 15 cm^3 and divided into 200 x 200 x 150 components in x, y and z directions, respectively, to give the scoring resolution of 0.5 x 0.5 x 1 mm^3 pixels. The tally volume was placed in the water phantom such that both of the surfaces coincide. TOPAS designation for the tally volume was "$Parallel$" as not to cause any simulation run errors. Since the statistics was poor for low particle histories, to ensure errors are below 5%, 100 million proton histories were simulated on a multiprocessor Linux workstation. The statistical uncertainty in PVDR calculations in simulations was obtained by propagating the error in peak dose and valley dose used in equation $PVDR = \frac{D_{peak}}{D_{valley}}$. Using error propagation equation for division, Equation 3.8, the percent error at entrance and the Bragg peak was obtained 3 %

and below 0.1% respectively.

$$\sigma_{PVDR} = PVDR * ((\frac{\sigma_{D_{peak}}}{D_{peak}})^2 + (\frac{\sigma_{D_{valley}}}{D_{valley}})^2) \tag{3.6}$$

3.2.7 Other simulation details

The default physics list, "$g4em - standard - opt4$","$g4h - phy - QGSP - BIC - HP$","$g4decay$","$g4ion - binarycascade$","$g4h - elastic - HP$","$g4stopping$", in TOPAS was used in the simulation without modification.

TOPAS fully allows the multi-threading capability of Geant4. By default, TOPAS will occupy just one CPU thread. However, in our simulations the number of threads was set to forty eight, because we ran the simulations with 48-core computing structure.

The TOPAS parameter file for this study is provided in the Appendix B.

3.3 Verification measurements with EBT3 film

The verification measurements of a few selected design parameter values were performed at the University of Florida Proton Therapy Institute (UFPTI) with IBA proton therapy PBS unit and at the Emory Proton Therapy Center (EPTC) with ProBeam proton therapy PBS unit. Even though our preliminary results from TOPAS show that tungsten collimator offers higher PVDRs, we decided to use brass collimator for our verification measurements for the following reasons: a) it is significantly easier to machine small holes in brass, b) brass is considerably cheaper than tungsten, c) less neutrons will be produced in brass and, d) brass is lighter than tungsten. Similarly, we decided to use 3 mm (instead of 2 mm) holes because: a) it is easier to drill a 3 mm hole and, b) it is easier to read out and analyze dose distributions from 3 mm minibeams. A collimator thickness of 3.25 cm was chosen for the experiment, because the IBA proton therapy unit has a snout capable of holding the aperture of that particular thickness. For other thicknesses, more custom machine work would have to be done, but this would increase the cost of the collimator. Figure 3.4 shows

the brass collimator. As shown, it consists of a total of 45 holes, plus a hole for possible single-hole experiment for later use, arranged in a hexagonal pattern. The c-t-c distance is 6 mm.

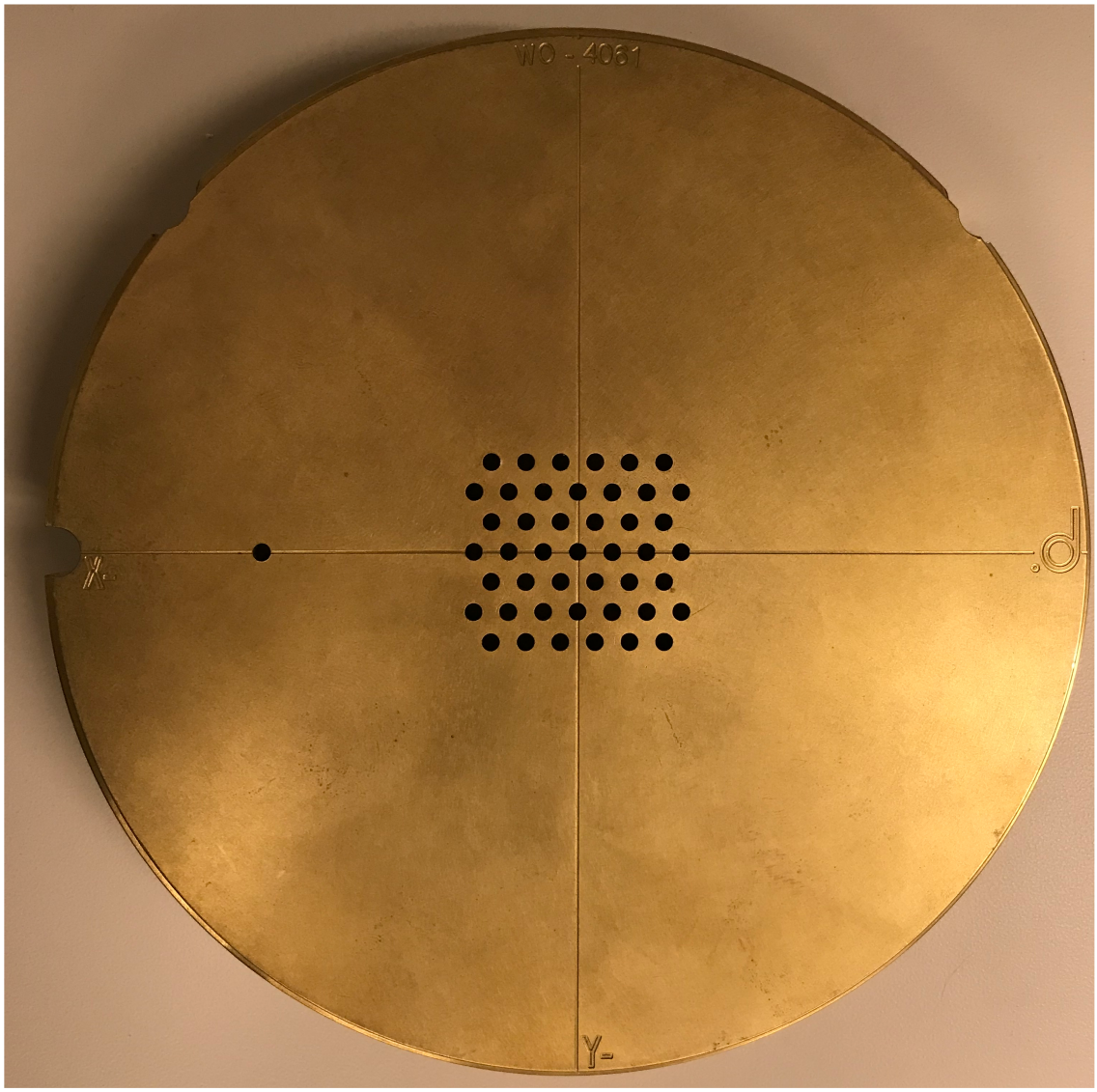

Figure 3.4: Manufactured brass collimator.

The setup from simulations was carefully reproduced. Relative dosimetry of PVDR was performed with Gafchromic EBT3 film (Ashland Advanced Materials, Bridgewater, NJ). Brass collimators were designed by DotDecimal (.decimal, Sanford, FL), precision manufacturer of patient-specific custom beam shaping devices for proton, electron, and photon therapies.

3.3.1 Gafchromic EBT3 film

Gafchromic EBT3 self-developing dosimetry film has been developed specifically for radiotherapy applications for the measurement of the absorbed doses of ionizing radiation [48].

Dosimetry of the PVDRs of the minibeams is inherently challenging due to the requirement of high spatial resolution. Ionization chambers, gold-standards in radiation therapy, do not have the spatial resolution to resolve the peak and the valley doses. Hence, film dosimetry is one of the two options, the other being cross-calibrated diamond detectors, for both absolute and relative dosimetry of minibeams [42].

The structure of EBT3 film, shown in Figure 3.5, is comprised of an active layer, 28 microns thick, sandwiched between two 125-micron matte-polyester substrates. The active layer has components like marker dye, stabilizers and other components to give the film its almost energy-independent response. EBT3 film is nearly tissue equivalent and can resolve features down to 25 microns. Moreover, the film develops in real-time without post-exposure treatment.

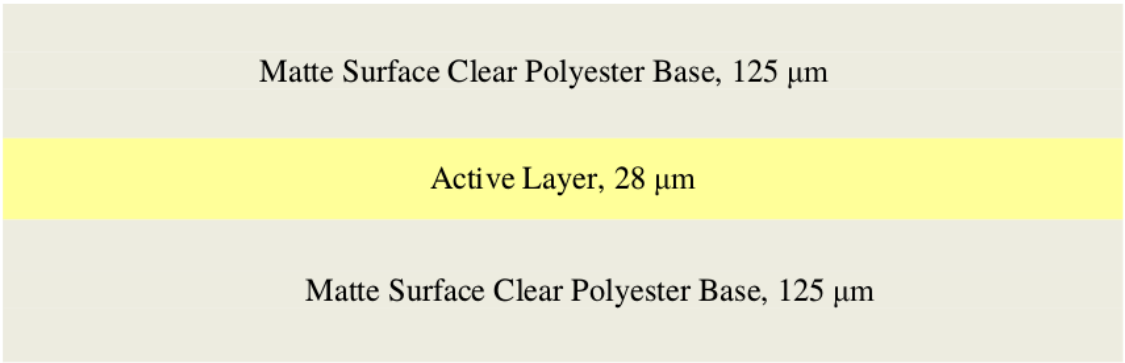

Figure 3.5: Structure of GAFChromic EBT3 Dosimetry Film.

The dynamic dose range of the film is 0.1-20 Gy. However, for optimum performance, a dose range of 0.2-10 Gy is advised. As such, this range was used in film irradiation for this project. Irradiated EBT3 films were analyzed using FilmQA Pro software.

3.3.2 FilmQA Pro

FilmQA Pro is a sophisticated, quantitative analysis tool designed to make quality assurance (QA) of intensity-modulated radiation therapy (IMRT) practical. The software can effectively help to scan the films and to calculate the dose maps.

Six film stripes were irradiated with a known dose and used together with an unirradiated stripe to produce a calibration curve. The curve was fit to a function having the form as in Equation 3.8.

$$d_x(D) = \frac{a+b}{(D-c)} \tag{3.7}$$

where $d_x(D)$ is the optical density of the film in scanner channel x at dose D, and a, b, c are the equation parameters to be fitted. The calibration curve of this form has many advantages: simple to invert and determine density as a function of dose, or dose as a function of density; fewer calibration points are necessary; the curve behaves similarly to the physical reality of the film.

3.3.3 Radiotherapy Plan

For measurements at the UFPTI, a total of 161 spots (approximately 12 and 14 spots in x and y direction respectively) with 7 mm and 6.0622 mm interspot spacing in x and y direction respectively were planned with RayStation treatment planning system (RaySearch Laboratories, Stockholm, Sweden) to obtain a uniform iso-energy layer of field size of 8 x 8 cm^2 at isocenter. The plans were normalized to deliver 3 Gy at the surface of the water phantom, which was situated at the isocenter.

The PBS gantry was set at 0 degrees and the snout was positioned in such a way that the air gap (distance between the distal end of the collimator and the surface of the water phantom) could be measured 7 cm, 10 cm and 20 cm for three different measurements. There was a latch built in the snout which made it easy to snugly slide the brass collimator in, as shown in Figures 3.6 and 3.7.

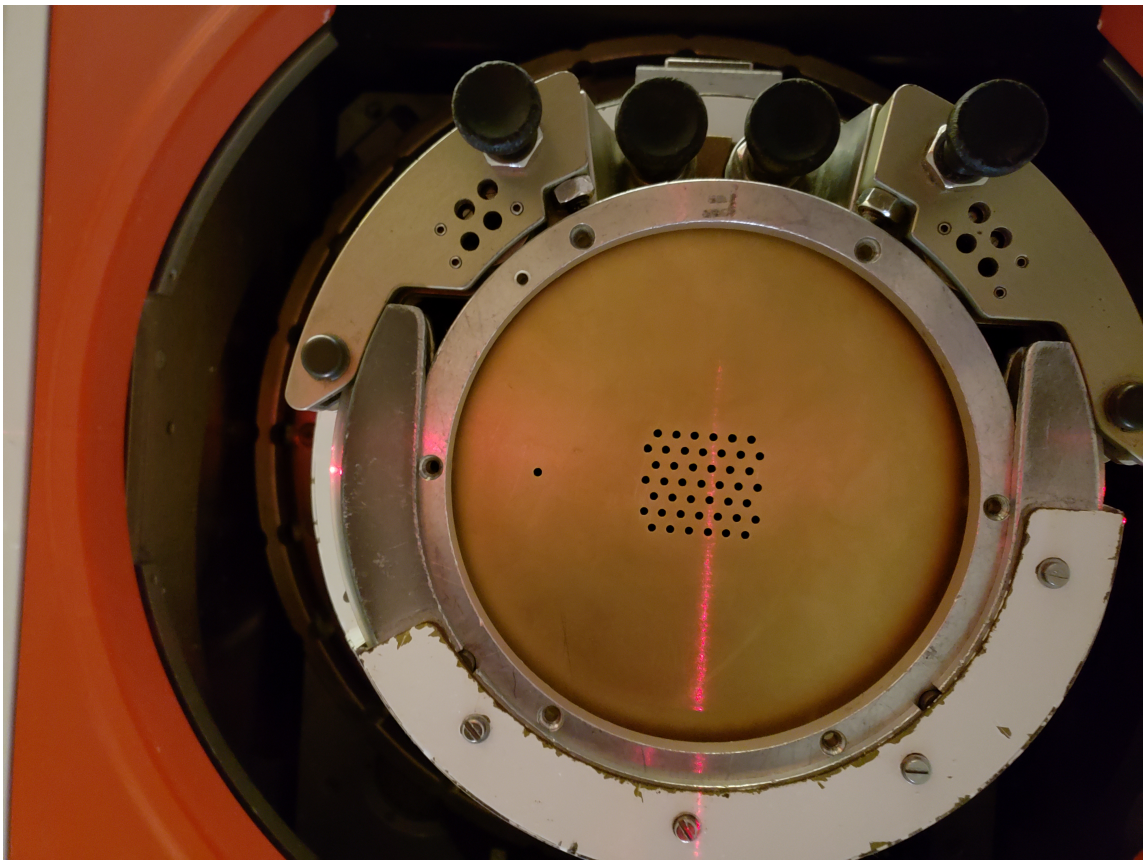

Figure 3.6: Latch for the brass collimator on UFPTI's IBA snout.

Since the availability of different thickness solid water phantoms was limited, the lateral profile of the minibeams, hence the PVDR, in water phantom was measured at the following depths: surface, 5.11, 7.17, 8.19, 9.22, 9.74 and 10.25 cm.

For measurements at EPTC, a total of 255 spots (17 and 15 spots in x and y direction respectively) with 5.3 mm and 6 mm interspot spacing in x and y direction respectively were planned with RayStation to obtain a uniform iso-energy layer of field size of 9 x 9 cm^2 at isocenter. The plans were normalized to deliver 6 Gy at the surface of the water phantom, which was situated at the isocenter.

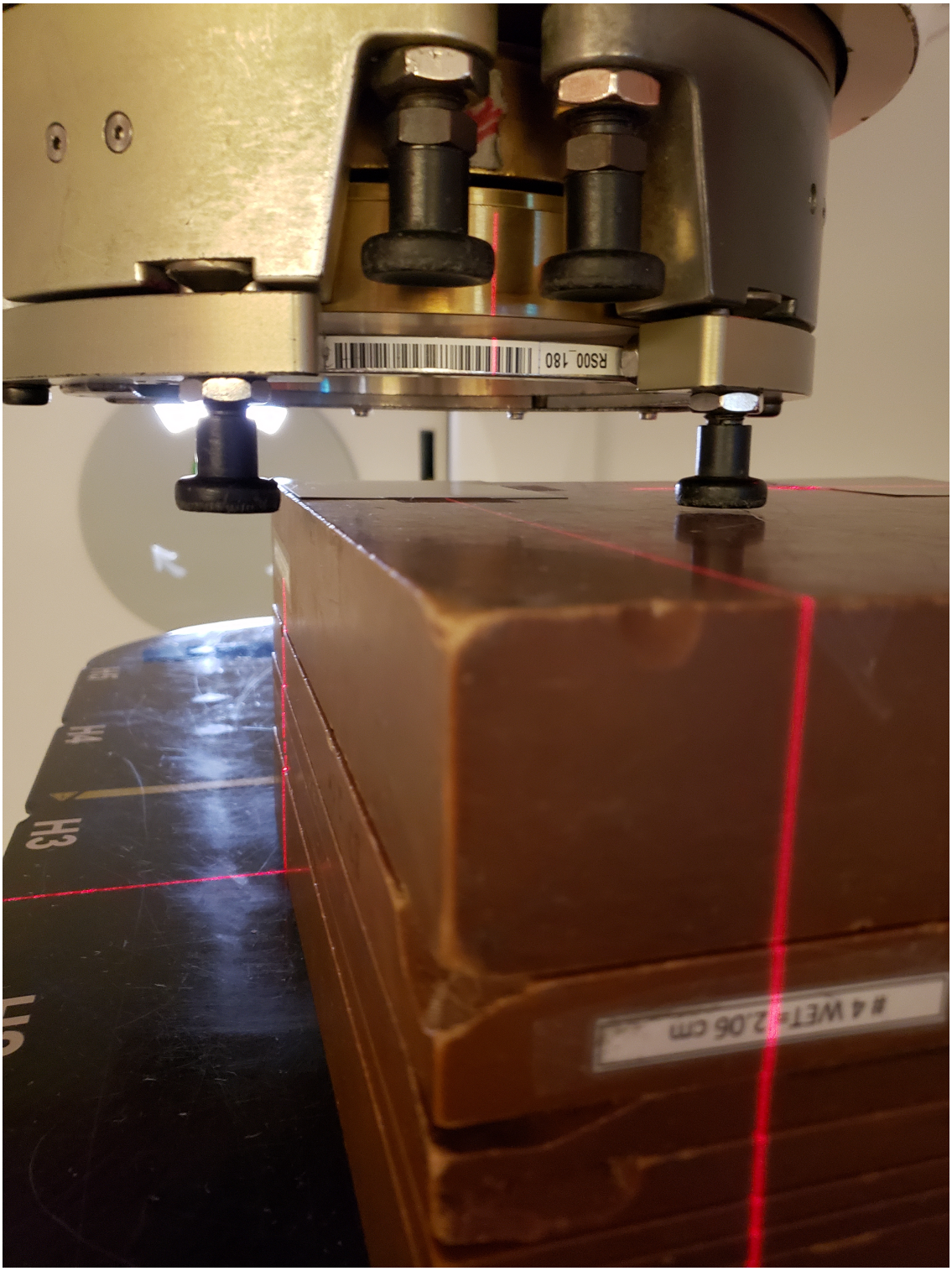

Figure 3.7: Snout and water phantom system at the UFPTI.

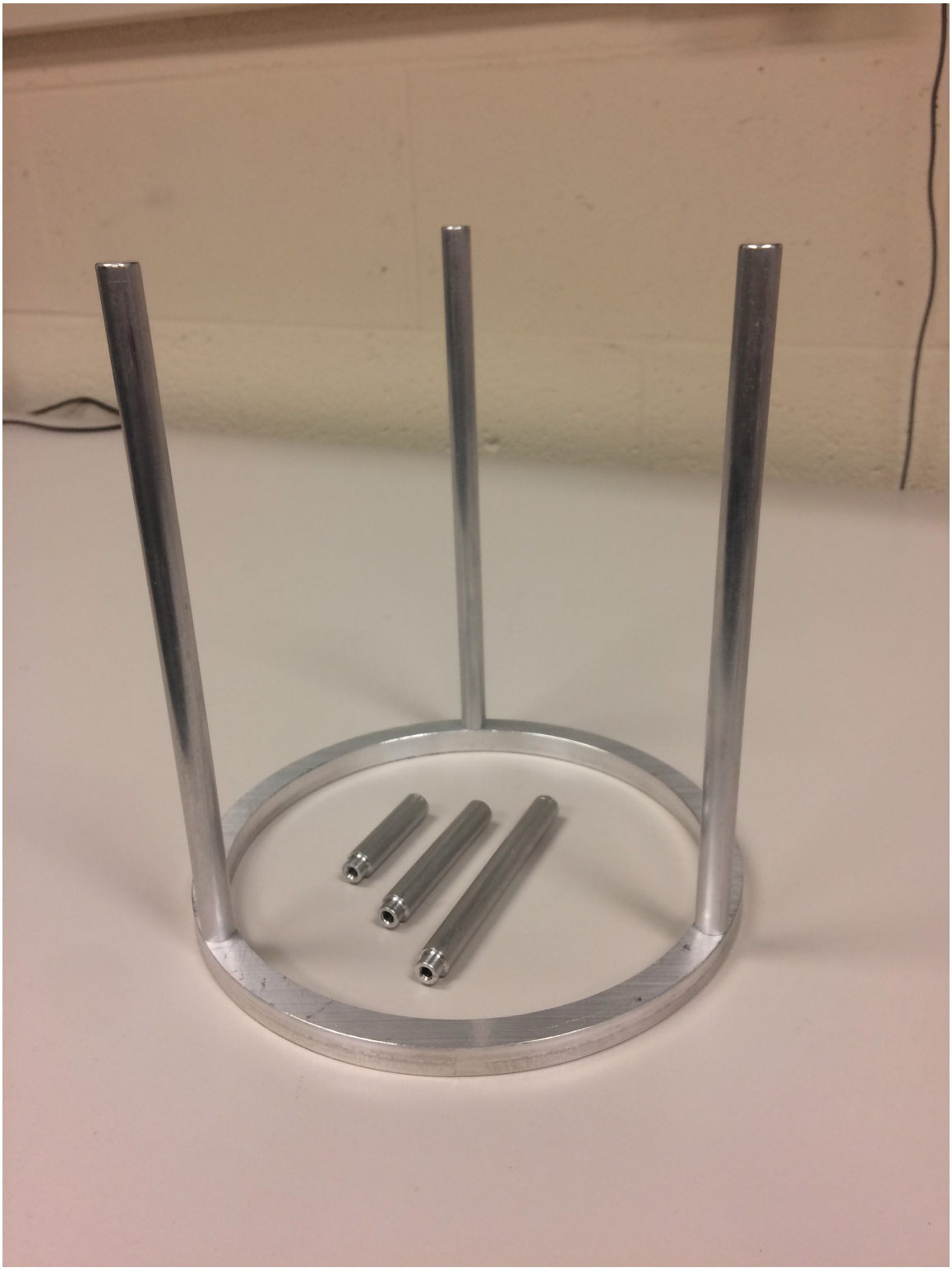

Figure 3.8: The collimator stand with various lengths of legs.

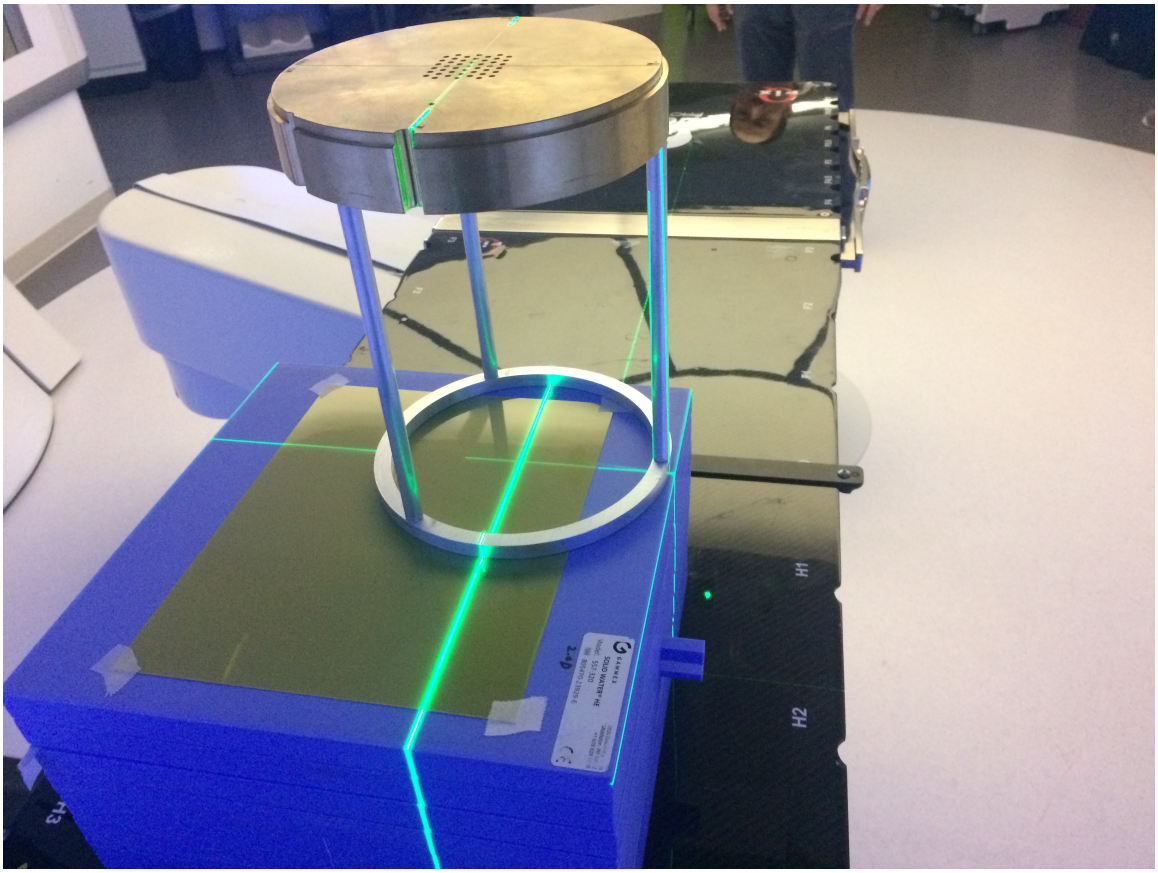

Figure 3.9: The experimental setup at the EPTC including: the stand, the brass collimator and the water phantom.

There was no latch compatible with our brass collimator in the snout of the ProBeam PBS delivery system. Therefore, we designed a stand for the collimator at Georgia Tech's machine shop. The stand was made out of aluminum and had three legs with different lengths which could be screwed to the main body of the stand to give a total height of the assembly of 5, 7, 10 and 20 cm. Figure 3.8 and 3.9 show the stand with 20 cm legs (screwed to the main circular body) together with the shorter legs and the brass collimator placed on top of the stand which is situated on top of the solid water phantom. At EPTC, PVDR values were measured at following depths: surface, 2, 4, 6, 8, 10.6 cm.

3.4 Results and Discussion

This section includes two parts. The first part (Section 3.4.1) shows the PVDR results obtained from TOPAS simulation. The second part (Section 3.4.2) shows the PVDR results obtained from the EBT3 film measurement as well as the comparison between the simulated and the measured results.

3.4.1 Results obtained from TOPAS simulation

A large number of 3-D peak and valley dose profiles were obtained from TOPAS to assess the effect of each design parameter on the PVDR. An example of the 3-D dose profile is shown in Figure 3.10 for proton energy of 120 MeV, collimator hole size of 3 mm, and c-t-c distance of 9 mm. The results are summarized in Figures 3.11-3.16. The proton phase space parameters used for the illustrations in this section are those from the ProBeam unit at the Emory Proton Therapy Center. A separate set of the PVDR results with IBA's phase space parameters were also obtained, and some of those results are presented in Section 3.4.2.

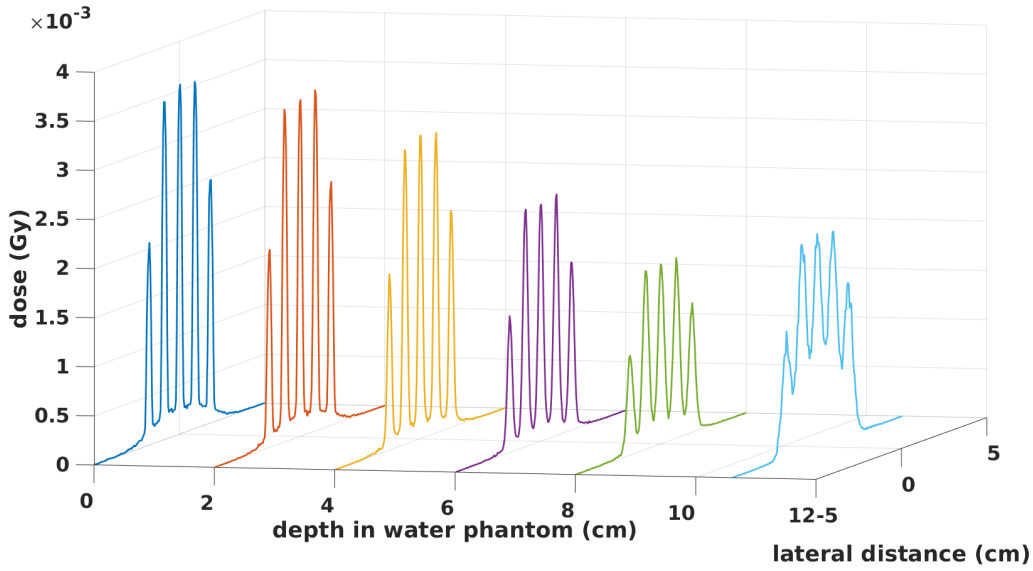

Figure 3.10: Illustration of depth and lateral profile for PVDR calculations.

As discussed in Section 3.1, for SFRT it is desirable to have high PVDR values anywhere outside the tumor volume and to have a PVDR approaching unity in the tumor volume, or Bragg peak. One purpose of this study is to show that high PVDR values at shallower depths and a PVDR value close to unity can be achieved with the proposed minibeams. Experimental evaluation of how high a PVDR needs to be comes from Dilmanian et. al [27], Deman et. al [49] and many others [32, 41]. The PVDR value of $\sim$10 showed minimal damage to the surrounding normal tissue, so this was the baseline target for this project.

Figure 3.11 shows the TOPAS results of PVDR versus depth in phantom for two collimator materials, tungsten and brass. The corresponding values of hole diameter, center-to-center distance, phantom to collimator distance, collimator thickness, energy of the proton beam are, respectively, 3 mm, 6 mm, 7 cm, 3.25 cm, and 120 MeV. Tungsten offers superior PVDR all the way to a depth of 6 cm, where PVDRs equalize. In this sense, tungsten is a better choice than brass.

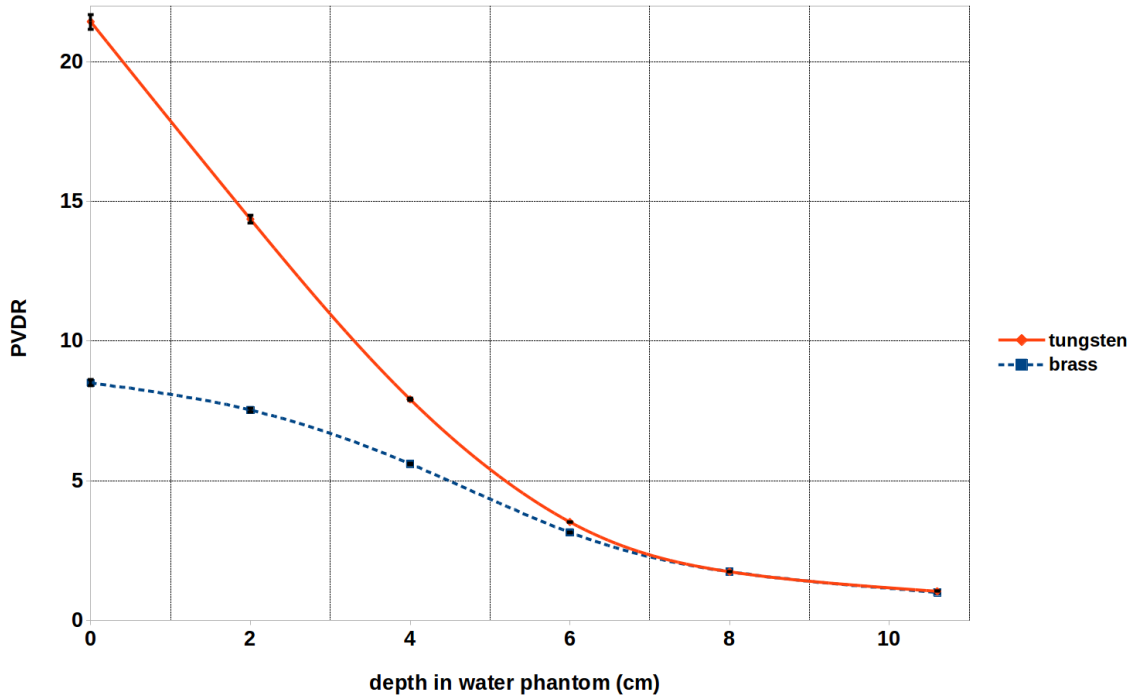

Figure 3.11: The effect of collimator material on PVDR at various depths in the water phantom. The data is based on tungsten and brass collimators of 3.25 cm thickness, 7 cm air gap, 3 mm holes, and 6 mm c-t-c distance. The energy of the proton pencil beam is 120 MeV.

Figure 3.12 shows the effect of c-t-c distance on PVDR. It can clearly be seen that increasing c-t-c distance offers superior PVDR. On average, a c-t-c distance of 12 mm, as compared to 6 mm, results in five fold increase in PVDR. Experimental verification of PVDRs with these parameters is difficult, because valley doses are so low that a very high dose in peak regions must be delivered to obtain readable values in valley regions in the film analysis. However, there is a limit to a high dose that can be delivered to the peak regions before saturating the EBT3 films. With optimum performance range, 0.2-10 Gy, of EBT3 films PVDR values of up to 50 can be measured. Any value above that might be error prone with EBT3 films. For this purpose, further investigations with EBT-XD films with optimum range of 0.4-40 Gy might be useful.

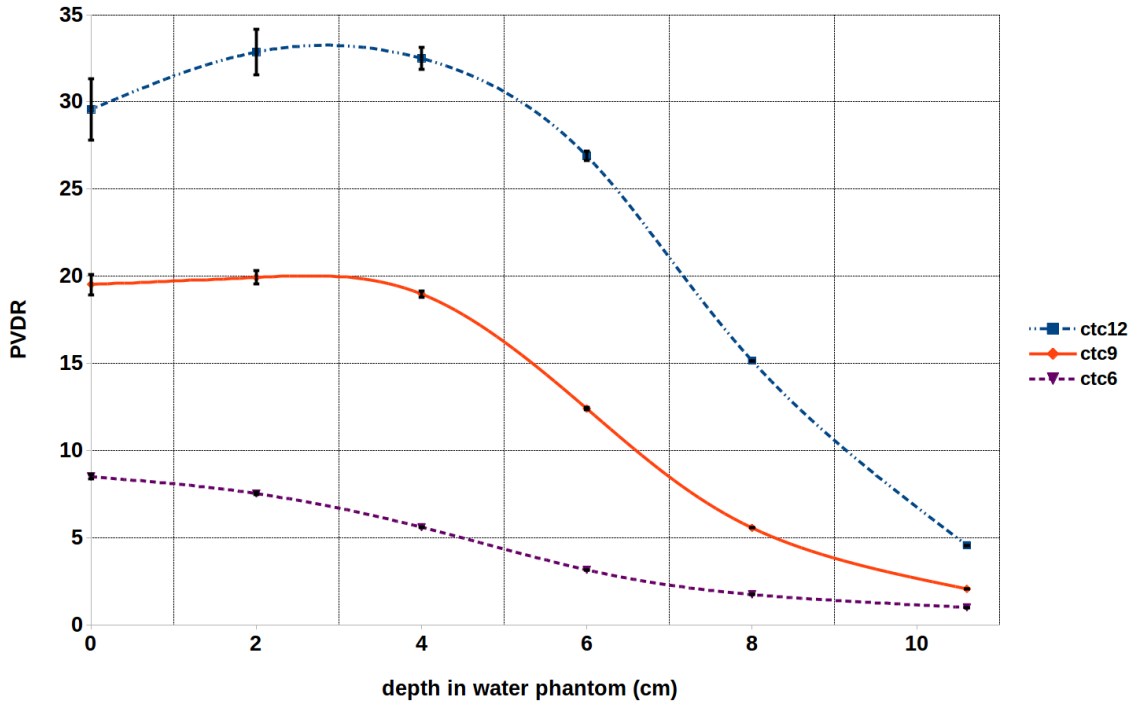

Figure 3.12: The effect of center-to-center distance on PVDR. The data is based on brass collimator of 3.25 cm thickness, 7 cm air gap, and 3 mm holes. The energy of proton pencil beam is 120 MeV.

Determination of PVDRs with larger c-t-c distances is challenging not only in measurements, but also in simulations. In simulations, as the c-t-c distance is increased, less protons are making it to the valley regions, resulting in high ($\sim$ 15%) errors. To minimize that error more than 10^9 proton histories need to be run, which comes with a penalty of increased computing time.

Figure 3.13 shows that as the collimator is made thicker, the PVDR increases. Collimator thickness of 6.5 cm, as compared to 3.25 cm, results in twofold increase in PVDR at shallower depths. The PVDR trend with depth looks much like PVDR trend for ”brass versus tungsten” graph, Figure 3.11.

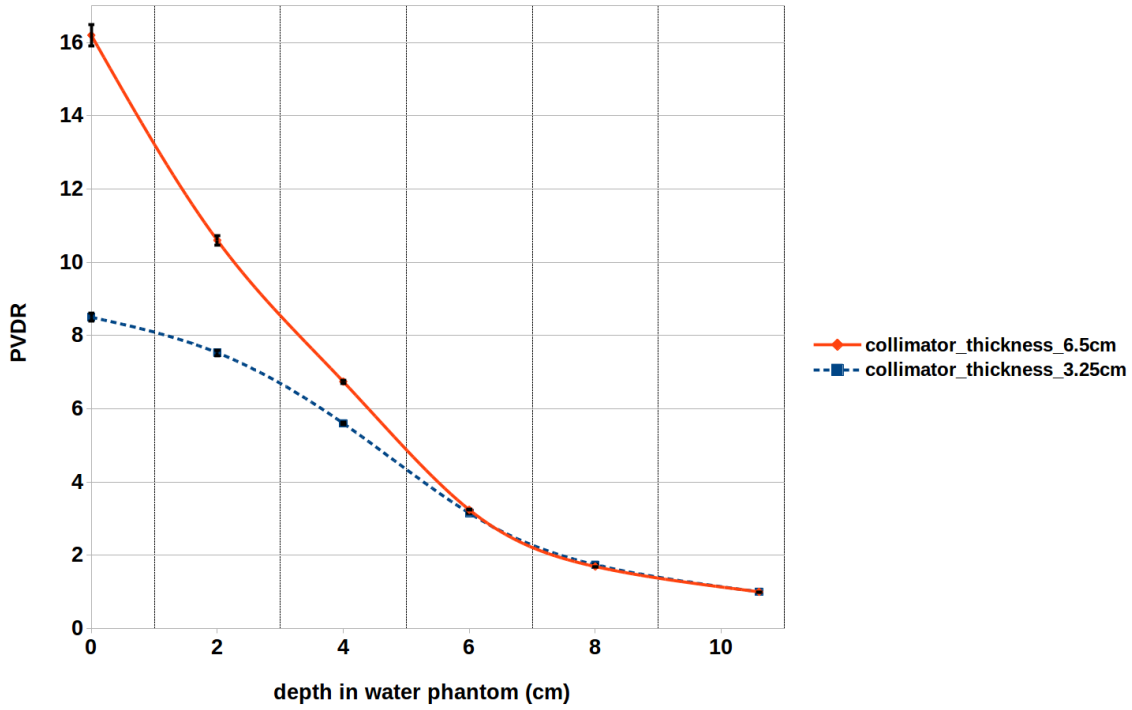

Figure 3.13: The effect of collimator thickness on PVDR. The data is based on brass collimator, 3 mm holes, 6 mm c-t-c distance and 7 cm air gap. The energy of proton pencil beam is 120 MeV.

Intuitively, one would expect the PVDR to be the highest at the surface of the phantom, but Figures 3.12 shows that PVDR starts with lower values, rises to a maximum at a depth of about 3 cm and starts falling after that. This suggests that scattered protons having lesser energies are making their way to the phantom and depositing their dose superficially in the valley regions. This effect (more detailed discussion follows in the next chapter) could be eliminated if a thicker collimator is used (see Figure 3.13). This implies that the thicker collimators than theoretically necessary to stop the protons of a certain energy are needed to achieve sharper penumbras and high modulation. This, of course, is at expense of a slight drop in dose rate with increasing collimator thickness, which is discussed in the next chapter.

TOPAS simulations and measurements also suggest that shorter phantom to collimator distances will result in higher PVDRs. The extent of dependence of the PVDR on air gap is

not as evident as it was in the case of c-t-c distance or collimator thickness for a 120 MeV pencil beam, as shown in Figure 3.14.

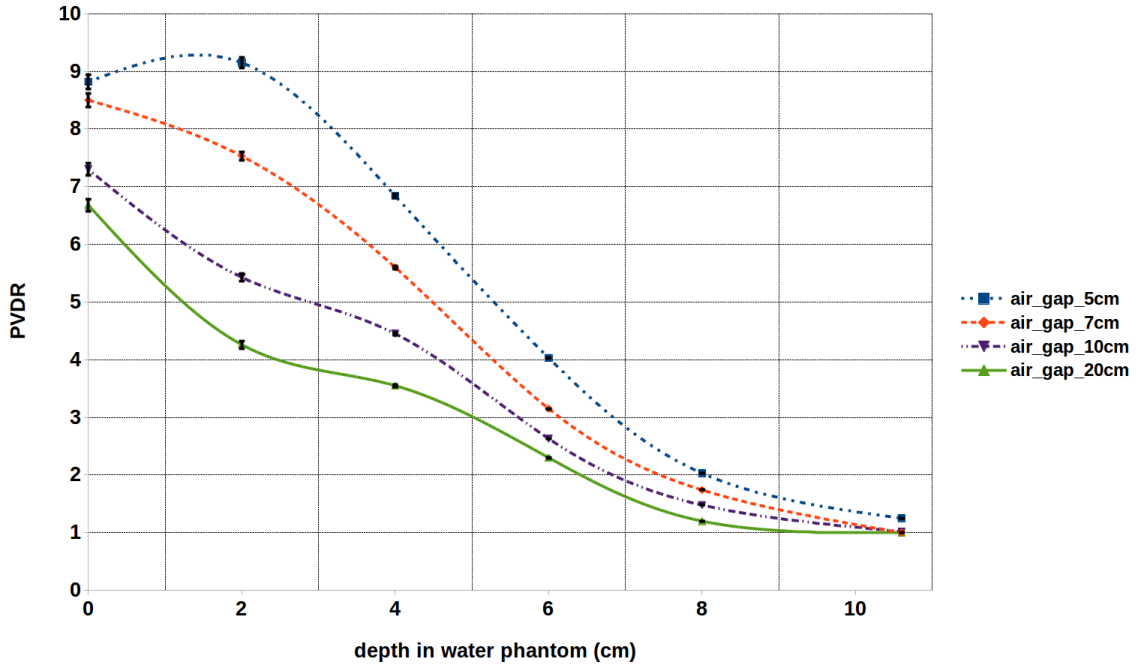

Figure 3.14: The effect of air gap on PVDR. The data is based on brass collimator of 3.25 cm thickness, 3 mm holes, and 6 mm c-t-c distance. The energy of proton pencil beam is 120 MeV.

Figure 3.15 shows that higher PVDRs can be achieved for 3 mm diameter holes as compared to 2 mm diameter holes. To keep the ratio of the hole diameter to the c-t-c distance constant (i.e. 1/2), 4 and 6 mm c-t-c distances were simulated with 2 and 3 mm holes respectively. Even though PVDR values with 2 mm minibeams were lower than those with 3 mm minibeams, they were still above the value of 2 below a depth of 4 cm in the water phantom. This is promising result, because 2 mm minibeams are desirable to gain higher benefit from radiobiology as discussed in Chapter 1.

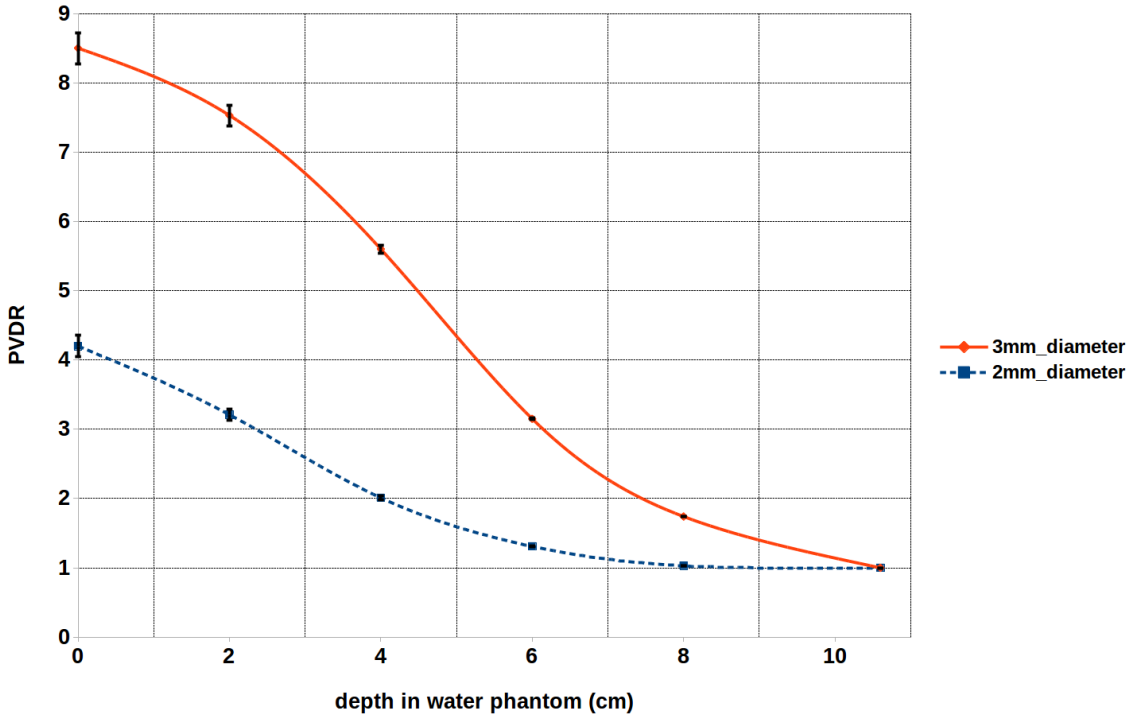

Figure 3.15: The effect of hole diameter on PVDR. The data is based on brass collimator of 3.25 cm thickness, and 7 cm air gap. Hole diameter is either 2 mm or 3 mm and center-to-center distances are: 4 mm (for 2 mm hole) and 6 mm (for 3 mm hole). The energy of proton pencil beam is 120 MeV.

In clinic setups, it is well known that a pristine Bragg peak obtained from single energy layer proton beam is unsuitable for cancer treatment, because it is very narrow longitudinally. It is essential to 'spread out' the Bragg peak to provide uniform dose within the target volume, by providing a suitably weighted energy distribution of the incident beam. In this project, energies from 120 to 140 MeV were modulated and multiplied by their corresponding weights, shown in Table 3.3, to obtain a 4 cm Spread-Out-Bragg-Peak (SOBP).

Table 3.3: Energy and relative weights of Bragg peaks used to obtain Spread-Out-Bragg-Peak.

Energy (MeV)	140	136	132	128	124	120
Relative weight	1	0.33	0.23	0.16	0.125	0.10

The PVDR values for the SOBP scenario are provided in Figure 3.16, in which it can be seen that PVDR values deteriorate slightly as compared to the pristine Bragg peak case. Nevertheless, for 3 mm diameter holes with 6 mm c-t-c distances, the entrance values of PVDR are as high as 6-7, which is below our baseline PVDR as mentioned before in this section. By adopting larger c-t-c distances and collimator thicknesses, the PVDR values can be increased for SOBP cases.

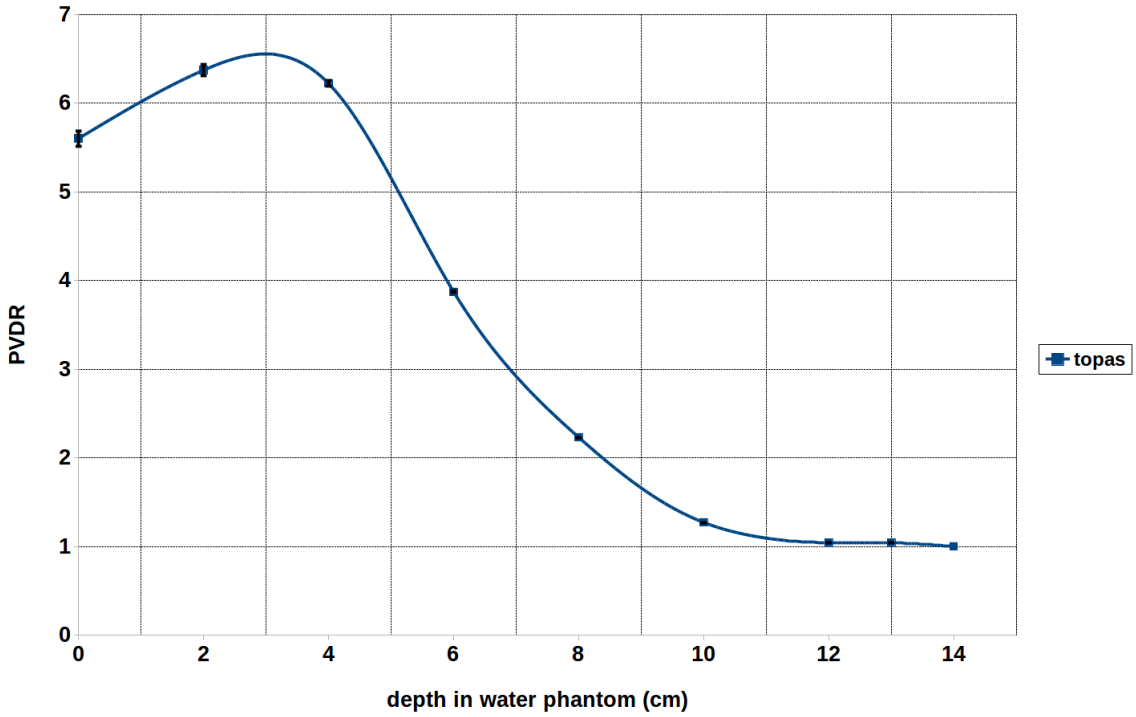

Figure 3.16: The PVDR versus depth in water phantom for the modulated proton beams creating the Spread-Out-Bragg-Peak (SOBP) over the depths of 10-14 cm. The data are based on brass collimator thickness of 3.25 cm, hole diameter of 3 mm, c-t-c distance of 6 mm, and air gap of 7 cm.

3.4.2 Results obtained from EBT3 film measurements

Figure 3.17 shows the dose distribution at different depths of a 150 MeV minibeams.

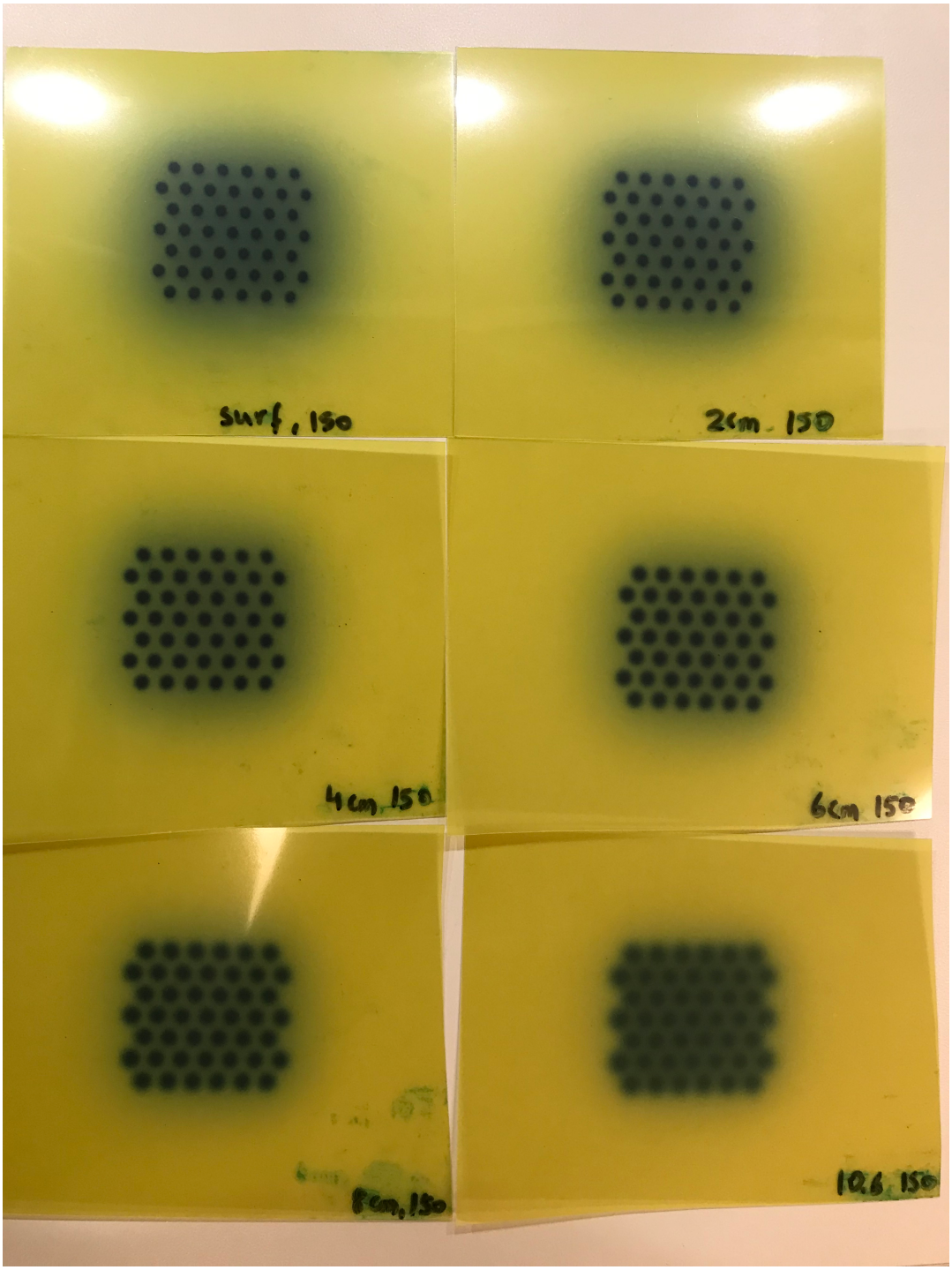

Figure 3.17: Dose distribution of 150 MeV minibeams at different depths.

Figures 3.18-3.20 show the PVDRs versus depth in water phantom for 120 MeV proton minibeams with air gaps 7 cm, 10 cm, and 20 cm, respectively. Figure 3.21 shows the same results for 150 MeV proton minibeams with air gap of 7 cm. Each of the four

figures includes the TOPAS results and the results obtained from both the film measurements made at both UFPTI and EPTC. Figure 3.22 shows the comparison of the TOPAS to the measurement results obtained at EPTC for the PVDR versus depth for the SOBP mentioned in Figure 3.16. The statistical uncertainty in PVDR calculations in film measurements was obtained by propagating the error in peak dose and valley dose used in equation $PVDR = \frac{D_{peak}}{D_{valley}}$. Using error propagation equation for division, Equation 3.8, the percent error at entrance and the Bragg peak was obtained 6.2 % and 1.5 % respectively.

$$\sigma_{PVDR} = PVDR * ((\frac{\sigma_{D_{peak}}}{D_{peak}})^2 + (\frac{\sigma_{D_{valley}}}{D_{valley}})^2) \tag{3.8}$$

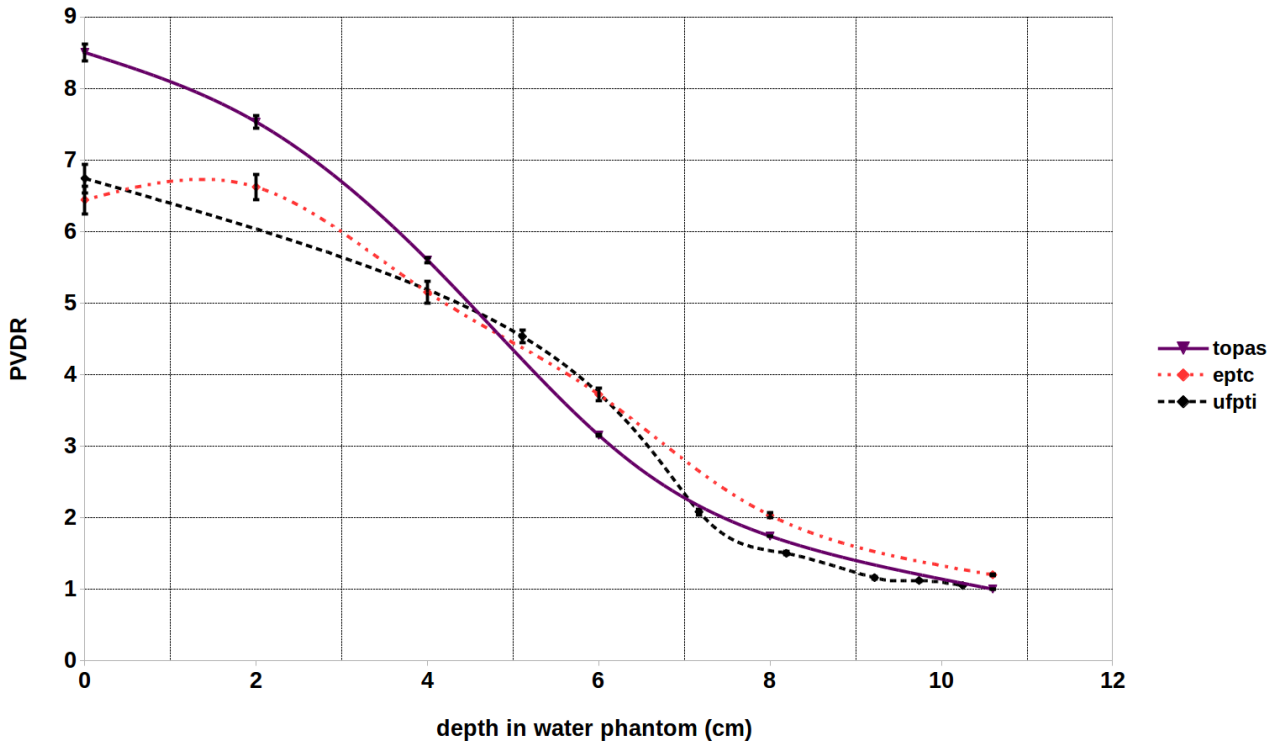

Figure 3.18: Comparison of the PVDR versus depth in water phantom for TOPAS simulations and measurements made at EPTC and UFPTI. The data is based on brass collimators of 3.25 cm thickness, 3 mm hole, 6 mm c-t-c distance and 7 cm air gap. The energy of the proton pencil beam is 120 MeV.

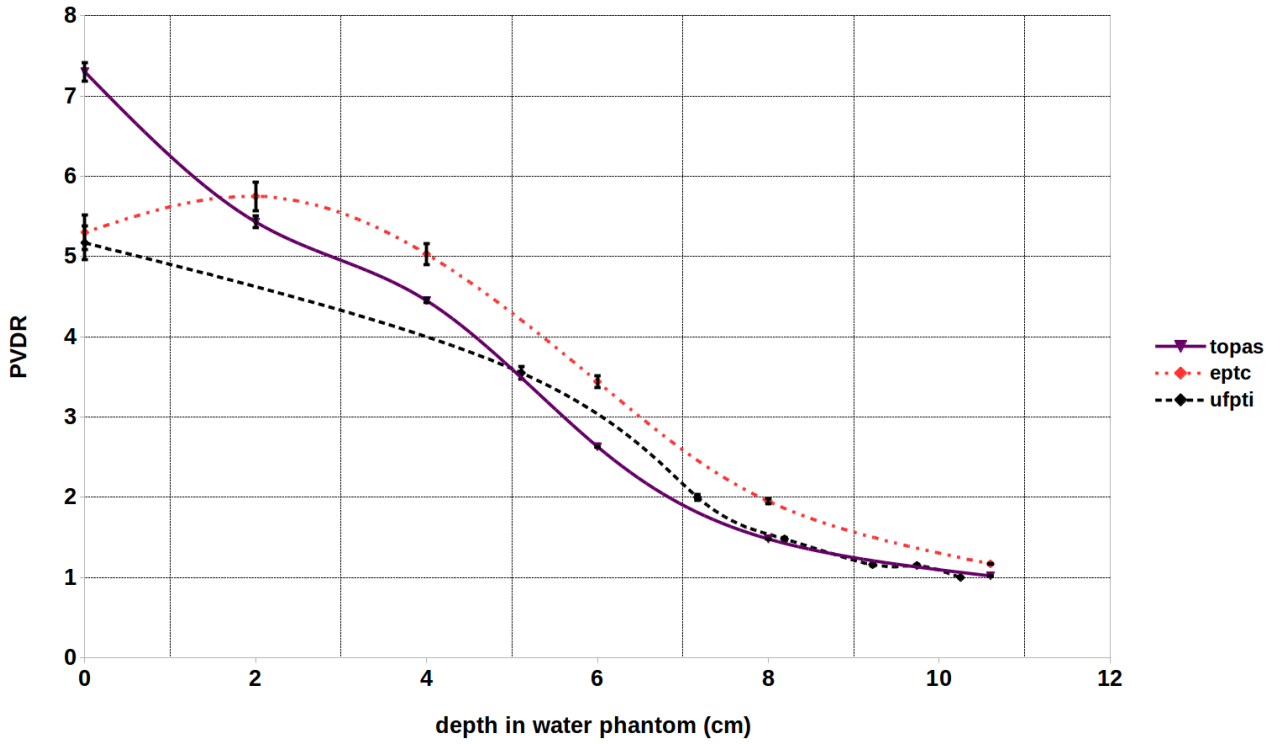

Figure 3.19: Comparison of the PVDR versus depth in water phantom for TOPAS simulations and measurements made at EPTC and UFPTI. The data is based on brass collimators of 3.25 cm thickness, 3 mm hole, 6 mm c-t-c distance and 10 cm air gap. The energy of the proton pencil beam is 120 MeV.

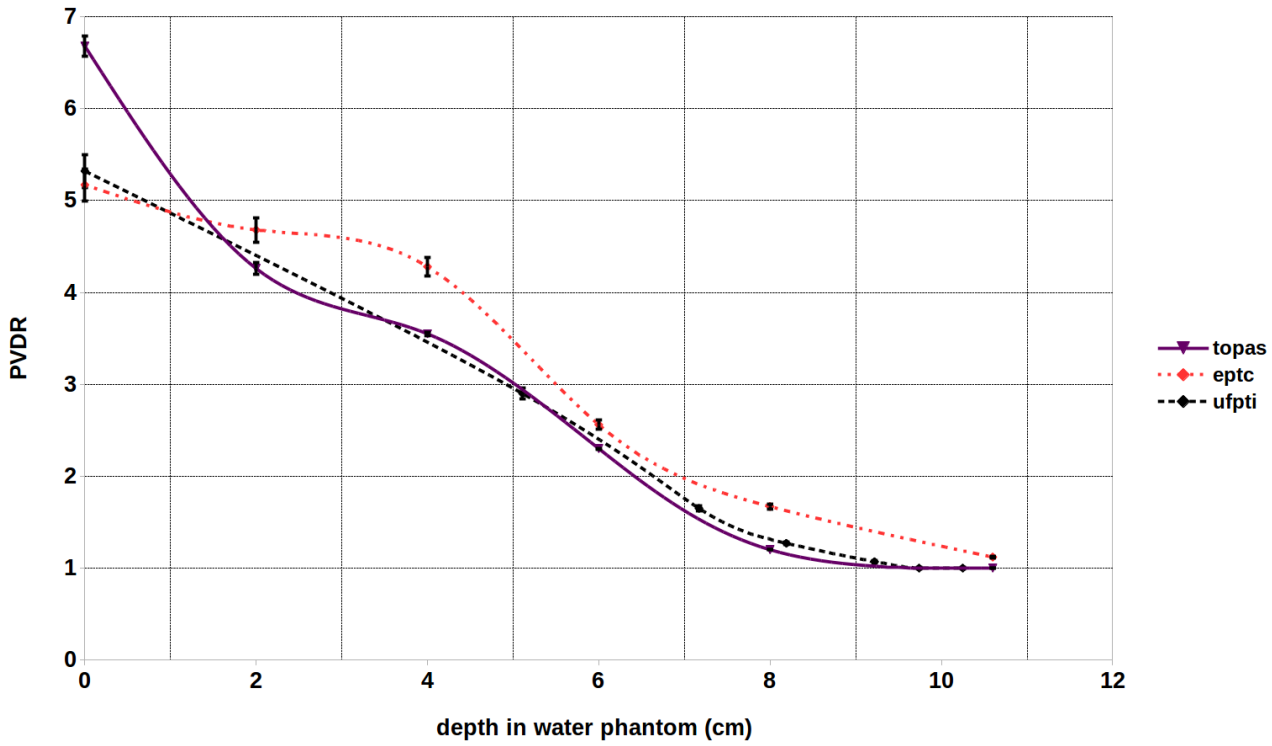

Figure 3.20: Comparison of the PVDR versus depth in water phantom for TOPAS simulations and measurements made at EPTC and UFPTI. The data is based on brass collimators of 3.25 cm thickness, 3 mm hole, 6 mm c-t-c distance and 20 cm air gap. The energy of the proton pencil beam is 120 MeV.

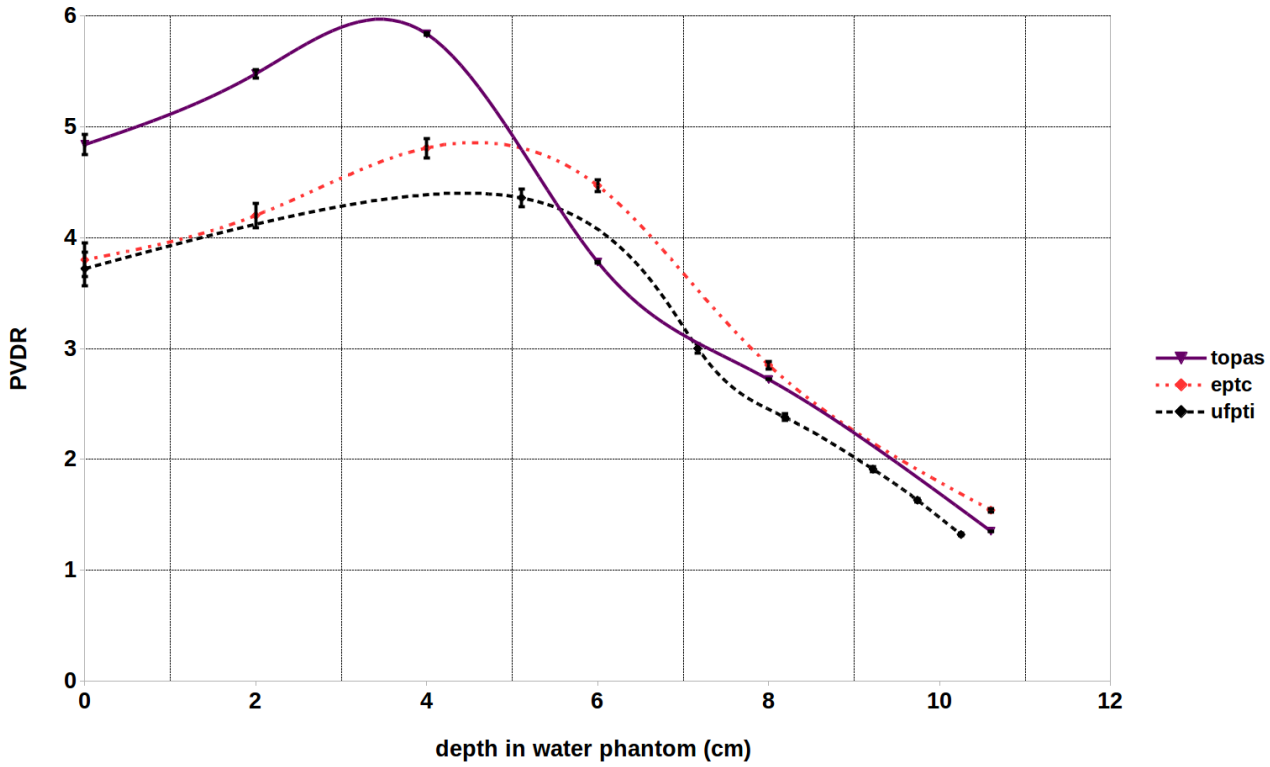

Figure 3.21: Comparison of the PVDR versus depth in water phantom for TOPAS simulations and measurements made at EPTC and UFPTI. The data is based on brass collimators of 3.25 cm thickness, 3 mm hole, 6 mm c-t-c distance and 7 cm air gap. The energy of the proton pencil beam is 150 MeV.

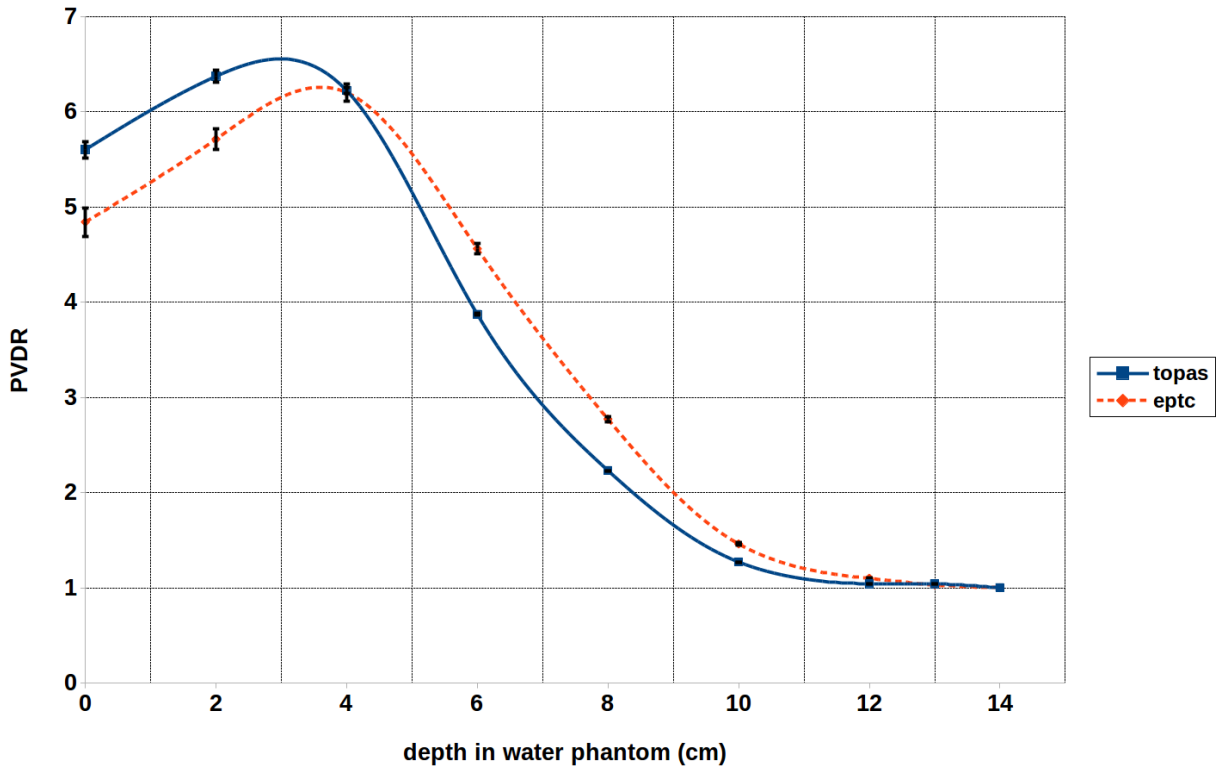

Figure 3.22: Comparison of the PVDR versus depth in water phantom for the TOPAS simulations and measurements made at EPTC. The data is for the modulated proton beams creating the Spread-Out-Bragg-Peak (SOBP) over the depths of 10-14 cm.

In general, measurement results of PVDR agree with TOPAS simulation results with percent difference range of 0.5-14% for both IBA and ProBeam PBS delivery systems. These differences are typical for film dosimetry studies for proton beams [50].

In most of the simulations and measurements performed in this project, lateral dose homogeneity at Bragg peak (i.e. PVDR $\sim$1) is not achieved. This implies that for most of the beam arrangements using single fields it will not be feasible to irradiate the target uniformly. Therefore, instead of a single field, multiple fields should be utilized from different directions making use of interlacing and crossfiring as suggested by literature [27, 51]. Interlacing also solves one other problem associated with minibeams: high entrance dose, resulting in smaller than unity Bragg peak to entrance dose ratio, as discussed in Chapter 2.

Conditions to satisfy the homogeneity constraint are not a trivial matter and sophisticated framework has been done to address the issue [52]. The requirement for dose homogeneity according to ICRU is $0.95 \leq D(x,y,z) / D_o \leq 1.07$, where D(x,y,z) is the local dose and D_o is the mean dose in the tumor [53, 54]. In the context of PVDR, D(x,y,z) attains a minimum value, D_{min}, in the valley region and a maximum value, D_{max}, in the peak region. Moreover, adopting more stringent definition of homogeneity than that of ICRU's, the following condition must be met:

$$0.95 \leq D_{min,max}/Do \leq 1.05 \tag{3.9}$$

The ratio in Equation 3.9 depends on (σ_{depth}/c-t-c distance), with σ_{depth} defined at treatment depth and being a function of energy, hole size, thickness of the collimator, air gap and depth of the target, i.e. σ_{depth}(E, σ_o, t, air gap, depth); hence the complexity.

In this project, this problem was investigated with a technique similar to inverse planning approach. For the same collimator design, constant air gap and energy, TOPAS was used to run simulations with different c-t-c distances until the condition in Equation 3.9 was reached. Results are depicted in Figure 3.23.

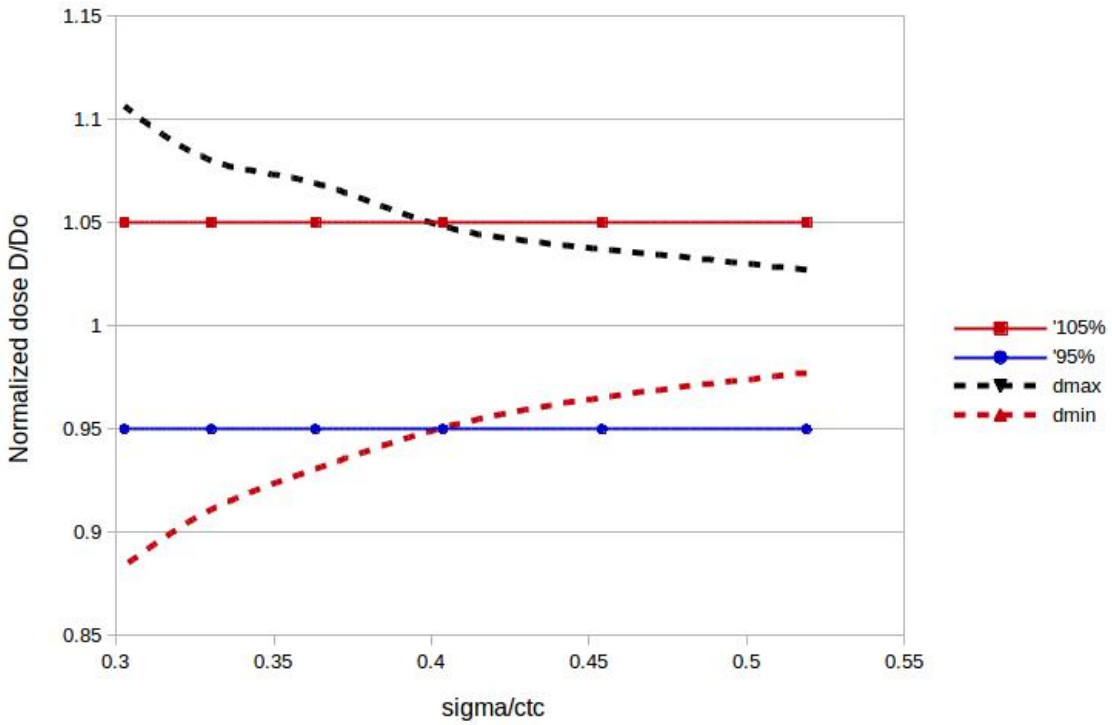

Figure 3.23: Optimal (σ_{depth}/c-t-c distance) to achieve dose homogeneity.

For hexagonal arrangement of holes, inverse planning approach suggests (σ_{depth}/c-t-c distance) = 0.4031 to achieve the dose uniformity between 95-105%. Similar result, 0.444, was obtained by Sammer et. al [52] for hexagonal geometry, except for, their homogeneity was defined more stringently between 97.5-103.5%. Generation of an extensive library of (σ_{depth}/c-t-c distance) for different treatment sites might be an interesting future research topic.

CHAPTER 4

ASSESSMENT OF DOSE RATE AND TREATMENT TIME

As mentioned in Chapter 1, an earlier attempt to produce proton minibeams using a physical collimator resulted in a dose rate that is too low for clinical use. The low dose rate is a necessary result of the collimator blocking most of the incident protons. The low dose rate, in turn, translates to a long treatment time. This becomes a major issue because patient motion during the treatment time may obscure the peak and valley doses, and therefore, may diminish the very benefit of the proposed mnibeam treatment. The issue of low dose rate has also been noted in many previous studies [41, 42, 51, 55].

In this study, mitigation actions have been taken to increase the dose rate: the employment of larger holes (3 mm) than the more ideal (submillimeter) sizes, the use of pencil beam scanning instead of double scattered beam and making center-to-center distances shorter. Sections below first describe the methods used to assess the dose rate at the Bragg peak, and then present and discuss the results.

4.1 Transmission at Bragg peak is a good indicator of dose rate

Measurement of the instantaneous dose rate of the proton pencil beam per spot is not an easy task [56]. It is a comprehensive calculation by itself involving beam current, ESS (energy selection system) efficiency (the ratio of beam current extracted from the cyclotron to that transmitted down the beam line after the energy degrader and energy selection system), interspot dead time, energy layer transition time and etc. The end result is very sensitive and combined with minibeam measurements it would be error-prone. Therefore, we approached the dose rate issue more simplistically by simulating and measuring the transmission of the dose at the Bragg peak. We believe that the transmission measurements will give a good idea about dose rate drop and consequently very close estimate of how

long the treatment time is going to be prolonged. Rationale behind this is twofold. The profile of the pencil beam after passing through the collimator changes both laterally and longitudinally. For the lateral profile, we have shown in the previous chapter that as long as the PVDR approaches unity, the lateral field size at Bragg peak is same for both uncollimated and collimated beam. Figure 4.1 is a good illustration of this. As a side note, there are ways to make PVDR approach unity as discussed in Section 3.6.

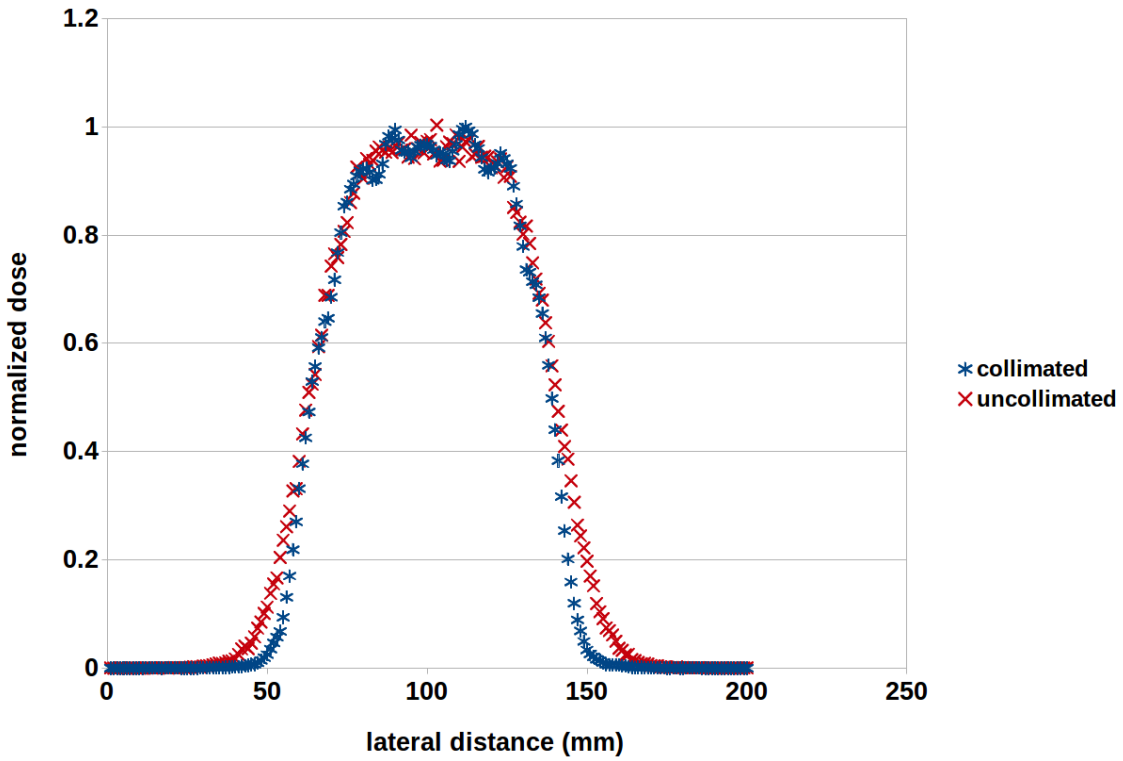

Figure 4.1: Comparison of lateral profiles of collimated and uncollimated beam at the Bragg peak.

As shown in Figure 4.1, the red curve is the normalized lateral profile of uncollimated beam at the Bragg peak, and the blue curve is the normalized lateral profile of collimated beam at the Bragg peak. The two profiles are essentially the same except that the collimated beams produce slightly better penumbra and are noisier due to poor statistics. That being said, by measuring the transmission of the dose we will assess the longitudinal changes in profile of the beam after passing through the collimator. With evidence suggested later in

this chapter it will be clear that longitudinal profile of the collimated beam changes. Hence, the measurement of the transmission is a simplistic and elegant way of assessing the drop in dose rate.

4.2 Definition of percent transmission used in this study

In the context of this study, the percent transmission is defined as the dose ratio of the collimated minibeam to the uncollimated beam at the Bragg peak for a single energy layer proton field, multiplied by 100%. This is illustrated in Figure 4.1 and with Equation 4.1.

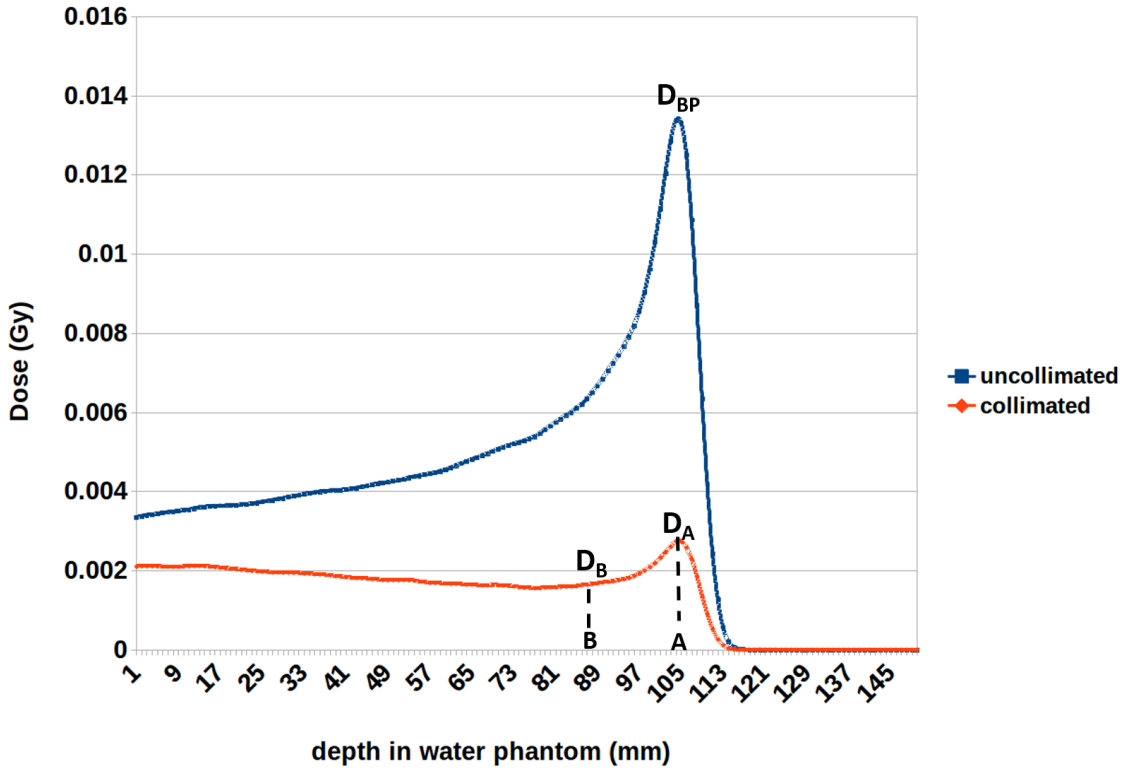

Figure 4.2: Depth dose curves for collimated and uncollimated 120 MeV proton beam.

$$\% \, Transmission \, at \, depth \, A = T_A = \frac{D_A}{D_{BP}} * 100\% \tag{4.1}$$

$$\% \, Transmission \, at \, depth \, B = T_B = \frac{D_B}{D_{BP}} * 100\%$$

4.3 Results and Discussion

4.3.1 Percent transmission of the proton minibeams

In this section simulation results for percent transmission of 120 MeV proton minibeams are presented, both in Table 4.1 and in Figure 4.3.

Table 4.1: Summary of simulation results for the percent transmission of 120 MeV proton minibeams at Bragg peak.

Physical parameter	Values	% transmission at Bragg peak
Hole diameter	3 mm	22.2
	2 mm	9.5
Center-to-center distance	6 mm	22.2
	9 mm	16.1
	12 mm	15.4
Collimator thickness	3.25 cm	22.2
	6.5 cm	20
Air gap	7 cm	22.2
	10 cm	21.4
	20 cm	20.5
Collimator material	brass	22.2
	tungsten	22.1

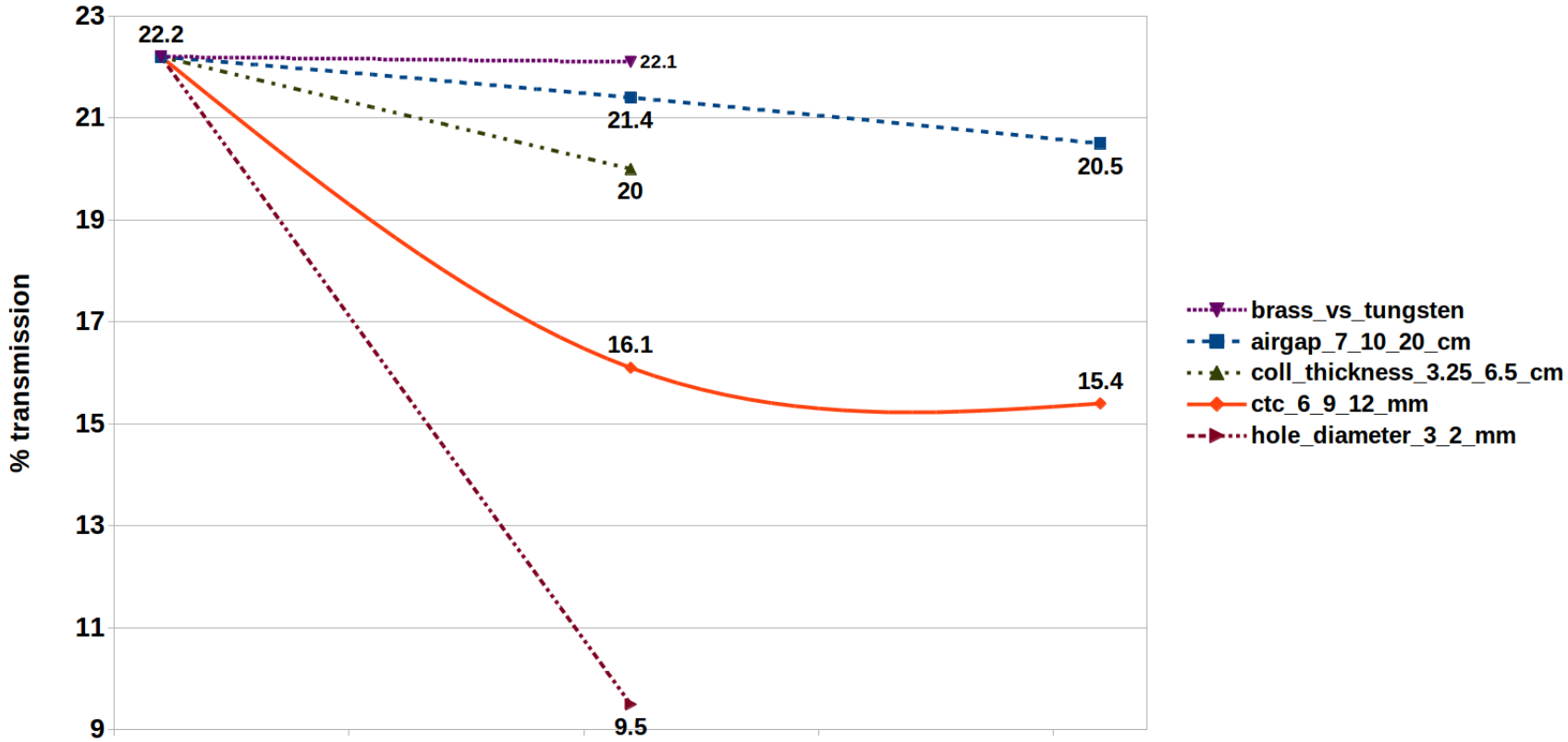

Figure 4.3: Summary of simulation results for the percent transmission of 120 MeV proton minibeams at Bragg peak. Figure shows the dependence of the percent transmission on different physical parameters.

4.3.2 Dependence of beam transmission on physical parameters

Overall, for 120 MeV proton minibeams, created with a collimator with properties: 3 mm hole diameter, 6 mm c-t-c distance, 3.25 cm thick and 7 cm away from water phantom surface; the percent transmission at Bragg peak measures around 20%. Transmission is a strong function of mostly two physical parameters used in this project: hole diameter and c-t-c distance; both of which change the ratio of the open area (where protons can pass) to closed area (where protons are blocked) of the collimator. Figure 4.3 shows that the biggest drop in transmission occurs when 2 mm hole is used instead of 3 mm hole. With 3 and 2 mm holes the percent transmission is 22.2% and 9.5% respectively. This result backs up our hypothesis made in Section 1.4 and shows why sub-millimeter minibeams like in some studies [30, 31, 32, 41] are prohibitive for clinical use despite having exceptional biological benefit.

Using larger c-t-c distances results in the second highest drop in percent transmission at Bragg peak. Percent transmissions with 6, 9 and 12 mm c-t-c distances are 22.2%, 16.1% and 15.4% respectively. Dose rate will benefit from smaller c-t-c distances; however, this will come with an expense of a drop in PVDR as evidenced in Section 3.6.

Figure 4.3 also shows that there will be a drop in percent transmission at Bragg peak, if the thicker collimators are used. 6.5 cm thick collimator results in 20% transmission, only 2% percent drop from the transmission with 3.25 cm thick collimator.

Transmission at Bragg peak is a very weak function of collimator material and air gap. With brass and tungsten the percent transmission is equal to 22.2% and 22.1% respectively. With air gaps of 7, 10 and 20 cm the percent transmission is 22.2%, 21.4% and 20.5% respectively.

4.3.3 Depth dose characteristics of the proton minibeams

One unique characteristic of the depth dose curve of proton minibeams is that the central axis dose decreases rapidly with depth and results in a Bragg peak dose which is lower

than the entrance dose. Hence, the maximum dose of the minibeams is at the entrance. This effect becomes more prominent as the size of the minibeam gets smaller. Figure 4.4 shows that for 3 mm minibeams the Bragg peak dose is 77% of the entrance dose; whereas, for 2 mm minibeams the Brag peak dose is 49% of the entrance dose. This effect is not desirable, but also inevitable. However, because the high entrance dose is delivered to a very narrow area, ∼2-3 mm, it does not pose danger in terms of radiobiology [32, 35, 42], as the damaged area will be able to quickly recover by regeneration of the nearby undamaged tissue.

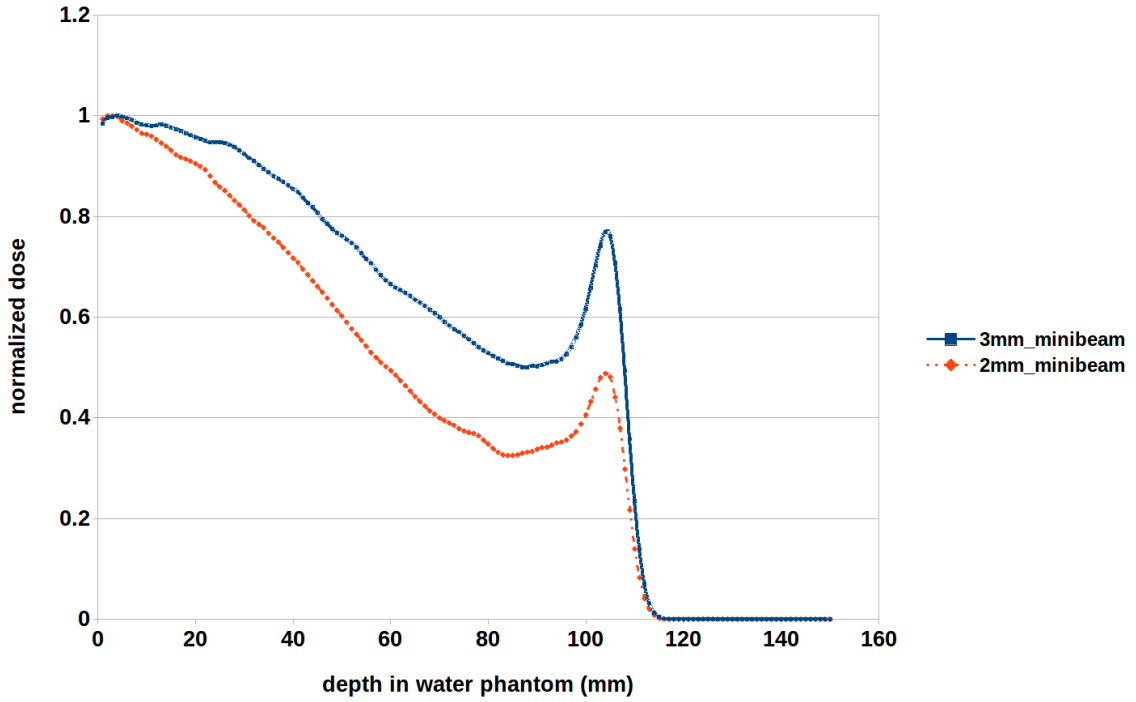

Figure 4.4: Normalized depth dose curve for 3 mm and 2 mm 120 MeV minibeams.

Another interesting characteristic of the depth dose curve of the proton minibeams is that the entrance dose of the minibeams can be slightly higher than that of the uncollimated beam. This is illustrated in Figure 4.5. The effect is known as ”slit scattering” [57], where protons which interact with a collimator do not stop and come out degraded. Those scattered protons can be categorized as inners, protons which entered the hole of the collimator and grazed out the far corner, and outers, protons which did not enter the hole to begin

with, but managed to scatter back into the hole.

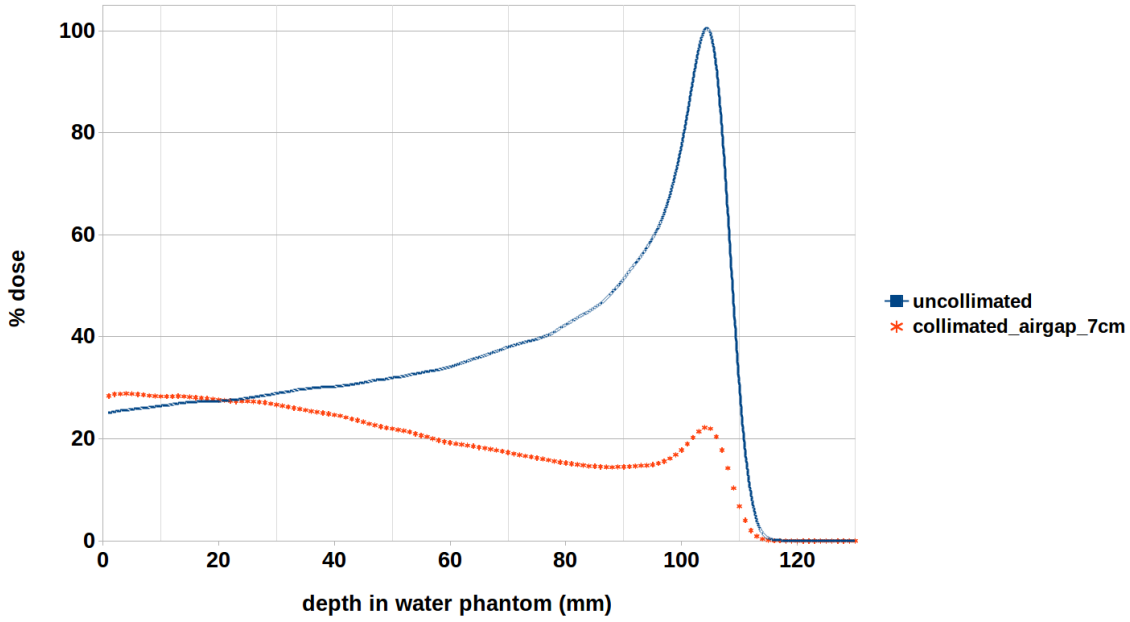

Figure 4.5: Depth dose curve of 120 MeV uncollimated beam compared to collimated beam.The air gap between the collimator and the water phantom is 7 cm.

The outcome of the ”slit scattering” is the enhancement of the dose at entrance up to a few cm depth, and it is even more pronounced with higher energy protons. This effect has been confirmed by the measurements made at both UFPTI and EPTC. For EPTC, the plans (for the uncollimated pencil beam) were normalized to 6 Gy at entrance, but what was measured with films (for the collimated minibeam) was 6.12 Gy for 120 MeV and 7 Gy for 150 MeV proton minibeams, which corresponds to 2% and 17% dose increase at entrance. Gottschalk et al. showed up to 30% increase of the entrance dose with 160 MeV protons [57]. The slight drop of PVDR at phantom surface discussed in Section 3.6 is the result of ”slit scattering”. With numbers being so significant, special care needs to be practiced when designing plans with collimators. One way to decrease the ”slit scattering” is to increase the collimator thickness.

4.3.4 Comparison of TOPAS simulations to measurement results

Figure 4.6: Comparison of percent transmission at Bragg peak, simulation versus measurement, for different air gaps. For this set of data constant physical parameters are: 3 mm hole diameter, 6 mm c-t-c distance, 3.25 cm thick brass collimator, 120 MeV energy of the of the proton beam.

Figure 4.6 shows the results for percent transmission at Bragg peak measurements of 120 MeV proton minibeams for different air gaps and compares them with TOPAS simulation results. There is about 30% departure of measurement results from the simulation results, with former being lower than the latter. The films that measured dose at Bragg peak were placed at 10.6 cm depth sandwiched between two neighboring solid water phantom slabs. It is quite possible that we missed the location of the Bragg peak, considering the possible experimental positioning error of the films, laser indicator, solid phantom thickness and range uncertainties, and rapid dose fall-off after Bragg peak. One way to test this was to compare simulation and measurement results of the percent transmission at other depths, preferably with flatter dose gradient. Figure 4.7 and Figure 4.8 compare simulation and measurement results of the percent transmission in water phantom at 8 and 6 cm depth respectively.

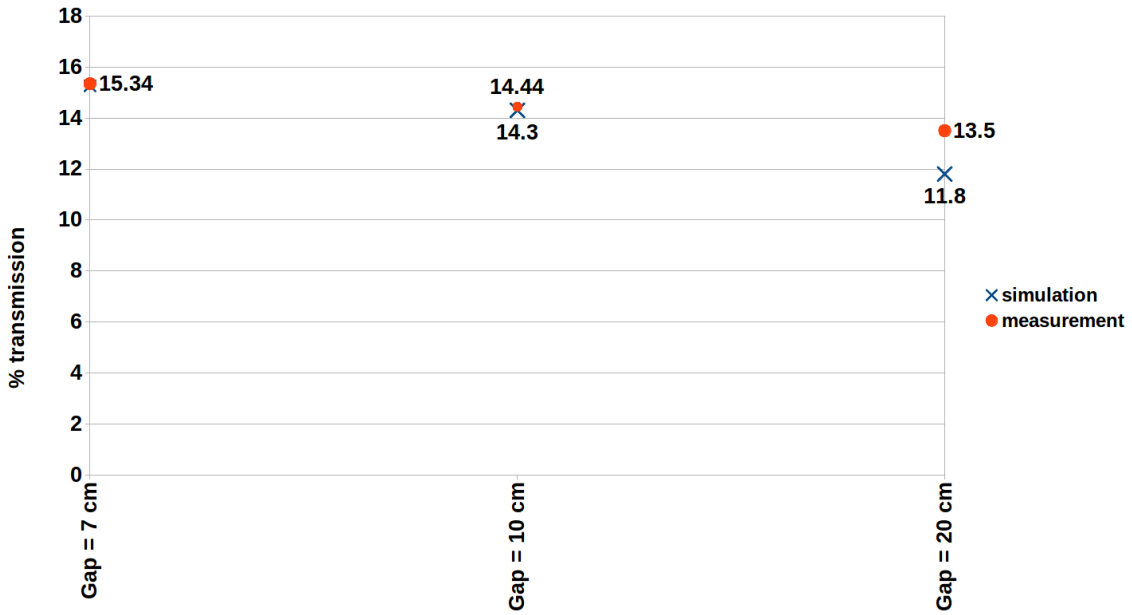

Figure 4.7: Comparison of percent transmission at 8 cm in water phantom, simulation versus measurement, for different air gaps. For this set of data constant physical parameters are: 3 mm hole diameter, 6 mm c-t-c distance, 3.25 cm thick brass collimator, 120 MeV energy of the of the proton beam.

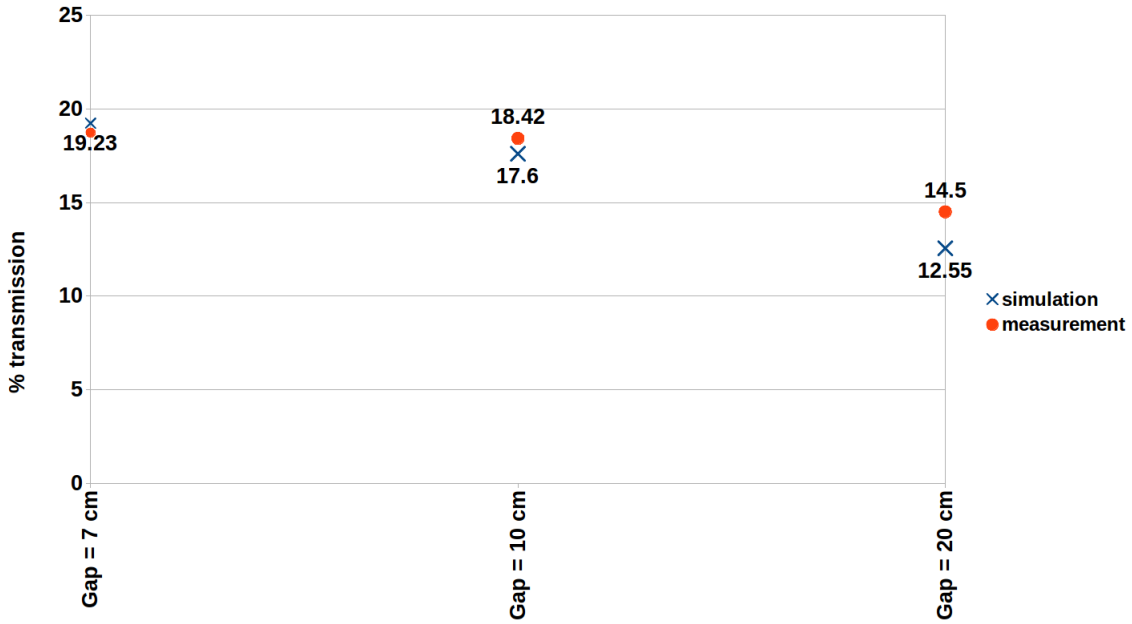

Figure 4.8: Comparison of percent transmission at 6 cm in water phantom, simulation versus measurement, for different air gaps. For this set of data constant physical parameters are: 3 mm hole diameter, 6 mm c-t-c distance, 3.25 cm thick brass collimator, 120 MeV energy of the of the proton beam.

Figure 4.7 and Figure 4.8 show that the measurement results agree better with simulation results at other depths, signaling that measurement at Bragg peak may have not been successful due to the positioning errors.

In conclusion, the transmission of the proton beams at Bragg peak was simulated and measured. Transmission at Bragg peak strongly correlates with dose rate at Bragg peak as shown in Section 4.1. Therefore, we conclude that the dose rate at Bragg peak for 120 MeV 3 mm minibeams with c-t-c distance of 6 mm will drop to about 1/5 of the uncollimated dose rate. If 2 mm minibeams are used instead of the 3 mm ones, then the dose rate will drop to 1/10 of the uncollimated dose rate. With the existing ProBeam dose rate ranges of 1-2 Gy/s, this translates to 0.2-0.4 Gy/s for 3 mm minibeams and 0.1-0.2 Gy/s for 2 mm minibeams. With current investigations going on with ultra high dose rate (FLASH) radiotherapy, it is known that very high dose rates are achievable [58]. FLASH dose rate ranges are 40-120 Gy/s as compared to typical ProBeam dose ranges of 1-2 Gy/s. Since the dose rate is one of the main issues hindering the clinical application of the proton minibeams, availability of such high dose rates is encouraging.

CHAPTER 5
SECONDARY NEUTRON DOSE

Secondary particles, from now on just secondaries, are unavoidable in proton radiotherapy and they cause additional unwanted dose to the patient. Owing to the complex shaping and modulation of the beam in proton therapy, secondaries of different types and energies are produced, including but not limited to: neutrons, alpha particles, protons, and heavier nuclear fragments. Among these, neutrons are of a particular importance for several reasons: they have high relative biological effectiveness (RBE) in terms of causing mutations, carcinogenesis, and secondary cancer; they are neutral and not subject to Coulomb forces and are highly penetrating; they are the main cause of secondary dose in proton therapy [59]. Especially for children who have long life expectancy after the treatment, the increase of the risk of secondary cancer due to neutrons could be significant [60]. Accordingly, it is important that one carefully assesses the additional secondary neutron dose produced by the use of physical collimator for the proposed proton minibeam system.

5.1 Production of secondary neutrons in proton radiotherapy

A wide range of neutron doses from proton therapy units has been reported [60, 61, 62, 63, 64, 65, 66] showing that neutron dose equivalent, NDE, per treatment proton dose is strongly system and conditions dependent; to be general, the amount of neutrons produced varies with the design of the beamline.

There are two approaches in the design of the proton therapy beamline to deliver the necessary dose: passive scattering and pencil beam scanning, PBS. The first method uses scatterers, energy modulating and beam flattening devices and collimators to obtain the homogenous dose in the target and sharp lateral penumbra. In the second technique, protons are actively scanned over the target volume with the aid of computers and scanning magnets

without the need for scattering, flattening and compensating devices to achieve the same goal as in the first method [67].

In PBS technique, most of the secondary neutrons are formed inside the patient. It has been shown that the NDE during proton radiotherapy using the PBS technique for a medium sized target volume is almost always below 1% of the treatment dose and can be neglected [63]. However, in this proposed work, since an additional collimation is used together with the PBS, the system will partially act like passive scattering. It has been shown that the most of the neutron dose in such type of delivery comes from the last collimating component, i.e. the brass collimator [68]. Hence, we performed calculations of ambient NDE with and without the presence of the collimator to evaluate if the collimator has significant neutron dose contribution.

5.1.1 Kinematics of the neutron production

Most of the modern proton delivery systems employ protons with energies ranging from 70-240 MeV. In this energy range, two nuclear processes, intranuclear cascade and nuclear evaporation are responsible for the production of the secondary neutrons [69].

For proton energies greater than 50 MeV, the dominant process is intranuclear cascade where protons, neutrons, alpha particles and sometimes heavier nuclei are formed as a result of interaction between the primary proton beam and the target. Produced secondary particles are expected to be mainly emitted in the forward direction, i.e. in the direction of the primary beam [70]. In theory, these particles can initiate further nuclear interactions called extra nuclear cascade; however, the probability to undergo extra nuclear interactions in clinical proton energy range is very low, because the energy required for such events is greater than a few hundred MeV [69]. Nevertheless, the energy of neutrons formed due to the intranuclear cascade can start around $\sim$10 MeV and can be as high as the energy of the primary proton beam.

Another possibility of neutron production is evaporation processes in which incident

primary or secondary proton or neutron is absorbed by the target and left in an excited state, known as compound nucleus. To achieve stability the compound nucleus emits protons, alpha particles and neutrons isotropically with varying energies from few keVs to around 10 MeV [60, 70].

As a result of two nuclear processes discussed in this subsection, the energy of secondary neutrons created in proton radiotherapy will have two peaks: due to evaporation and due to intranuclear cascade. Regardless, less than 3% of the neutron dose is produced by neutrons with energies less than 10 MeV and more than about 2/3 of the dose comes from neutrons with energies higher than 100 MeV [71]. Therefore, in the proton therapy context, the detection of higher energy (fast) neutrons is important.

5.1.2 Interaction of neutrons with matter

Neutrons have no net charge and therefore, are not subject to Coulomb force when traveling through matter. Their interaction cross section mainly depends on the type of target nucleus and neutron energy, with cross section being inversely proportional to their energy. The mean free path, the distance a particle travels between two interactions, of neutrons is inversely proportional to neutron cross section. As a result, fast neutrons are highly penetrating.

Neutron capture, elastic and inelastic scattering are three processes relevant in proton therapy.

Neutron capture is mostly dominated by thermal neutrons and relevant neutron capture reactions in proton therapy are: ^{14}N(n,p)^{14}C and p(n,γ)d [72]. In the former, the secondary dose is delivered via the radioactive isotope ^{14}C which is produced as a result of neutron activation. In the latter, the secondary dose is delivered in the form of delta rays and recoil deuterons [73].

In elastic scattering total kinetic energy is conserved in interaction between the neutron and the target nucleus. Kinetic energy may be transferred to the target, but no excitation

occurs. The recoiling target will lose its energy through ionizations. This type of interaction is dominated by intermediate neutrons [73].

Inelastic scattering results in absorption of neutron and possible re-emission of secondary particles including neutrons. The neutron absorption excites the target nucleus briefly and the nucleus will de-excite by emitting photons. Inelastic scattering is mostly dominated by fast neutrons [73].

5.2 Ambient neutron dose equivalent

Since the measurement of some radiation protection quantities like effective neutron dose is difficult, operational quantities are commonly used instead to conservatively estimate the protection quantities. In the context of this project, the operational quantity ambient dose equivalent, $H^*(10)$, was reported. $H^*(10)$ is used for area monitoring and defined as the dose equivalent that would be produced by the corresponding expanded and aligned field in the ICRU (International Commission on Radiation Units and Measurements) sphere (15 cm radius) at a depth of 10 mm on the radius opposing the direction of the aligned field [74]. Ambient dose equivalent can be calculated as shown in Equation 5.1.

$$H^*(10) = h^*(10) * \Phi \tag{5.1}$$

where Φ is the neutron fluence and $h^*(10)$, defined as $h^*(10) = (\frac{H^*(10)}{\Phi})$, is fluence-to-dose-equivalent conversion coefficient taken from ICRP Publication 74 [75]. The $H^*(10)$ is not tissue or organ specific; but, in most of the cases, it gives a considerable estimate of the effective dose.

5.3 Simulation of ambient neutron dose equivalent

It is notoriously hard to measure high-energy neutron doses in a mixed radiation field. A practical alternative for neutron dose estimation is to use a Monte Carlo approach which

was well validated by many groups [60, 65, 76].

Monte Carlo code TOPAS was used to simulate the geometry and to score the $H^*(10)$. The scorer "AmbientDoseEquivalent" ($s : Sc/scorer/Quantity = "AmbientDoseEquivalent"$) was used in TOPAS to prompt the tallying of the ambient dose equivalent. Only the ambient dose from neutrons will be considered by setting the filter "OnlyIncludeParticlesNamed" as $sv : Sc/scorer/OnlyIncludeParticlesNamed = 1"neutron"$.

Using summation notation, i.e. summing neutron spectral fluence over all energy bins, the Equation 5.1 can be expressed as in Equation 5.2.

$$H^*(10) = \sum_{i=1}^{n} h^*(10)_i * \Phi_i \tag{5.2}$$

where i and n are the index and the total number of neutron energy bins, respectively; $h^*(10)_i$ is the fluence-to-dose-equivalent conversion coefficient; and Φ_i is the neutron fluence in the the i^{th} energy bin determined from simulations. Equation 5.2 gives the ambient NDE at point of interest. There are twelve volumes, explained in detail in the next subsection, where $H^*(10)$ was tallied.

Pencil beam characteristics like spatial beam spread, angular divergence, the coefficient of correlation and energy spread were modeled as discussed previously in detail in section 3.2.2.

A uniform iso-energy layer of field size of 9 x 9 cm^2 at isocenter, similar to the one discussed in section 3.4.3, was simulated.

5.3.1 Geometry and Scoring

Figure 5.1 shows the geometry simulated with the collimator and Figure 5.2 shows the geometry simulated without the collimator.

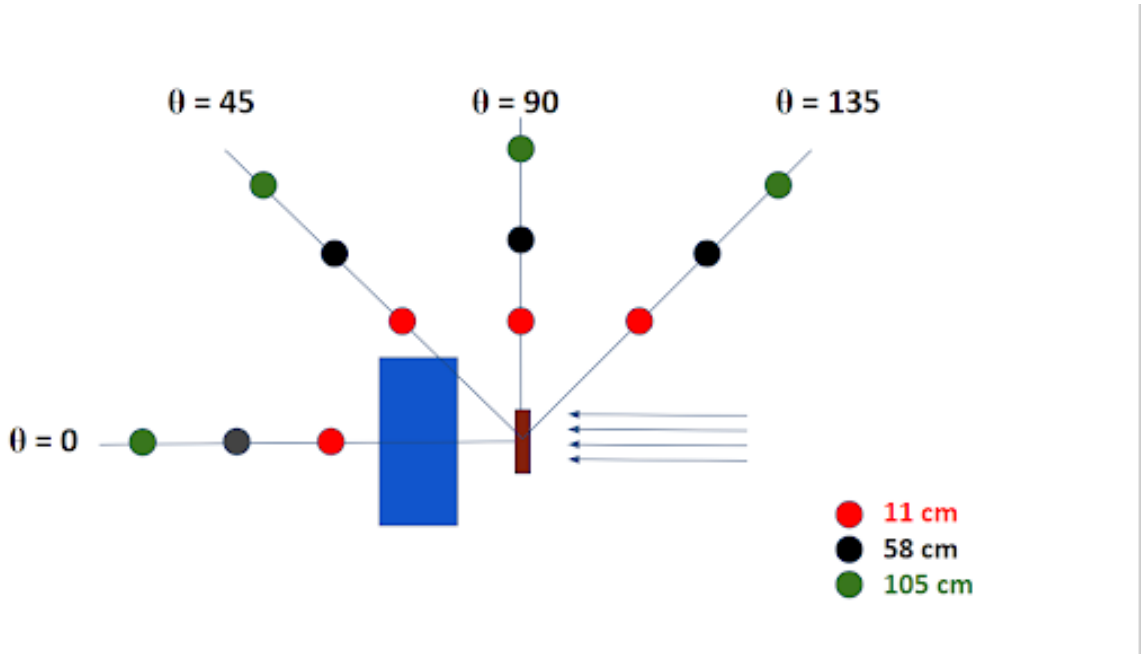

Figure 5.1: Geometric configurations and locations used in TOPAS to calculate the ambient neutron dose equivalent with the collimator.

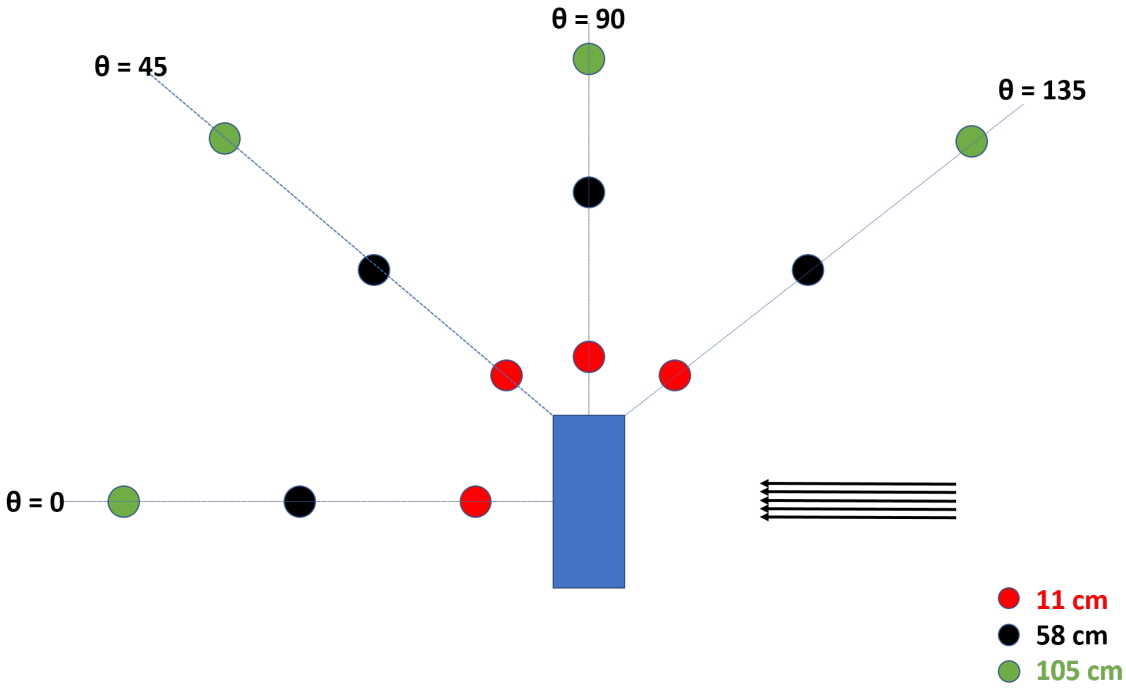

Figure 5.2: Geometric configurations and locations used in TOPAS to calculate the ambient neutron dose equivalent without the collimator.

The thickness of the collimator is either 3.25 or 6.5 cm. Air gap varies as 5, 7, 10 or 20

cm. Solid water phantom is a box with 30 x 30 x 15 cm^3 of volume. The collimator design is as shown in Figure 3.3. The ambient neutron dose equivalent was tallied at different angles: 0, 45, 90 and 135 degrees and varying distances: 11, 58 and 105 cm from one of the faces of the water phantom. The neutron tally volumes were in spherical shape with radii of 1 cm.

In this project, the ambient NDE per therapeutic proton dose will be reported. Therefore, a 4 x 4 x 4 mm^3 tally volume was placed in the water phantom along the central axis of a pristine peak or SOBP such that the volume scores the proton dose, D, at Bragg peak for pristine peak or middle of the SOBP plateau. $H^*(10)/D$ was obtained by taking the ratio of the ambient NDE tally at point of interest to proton dose tally. 100 million proton histories were simulated on a multiprocessor Linux workstation.

5.4 Measurements of ambient neutron dose equivalent

The geometry setup as discussed in Figures 5.1 and 5.2 was carefully reproduced at EPTC. Total of eight data points were recorded, 4 without collimator and 4 with the collimator. A rem counter Wide Energy Neutron Detection Instrument, WENDI-II (Thermo Scientific, Waltham, MA), was used as the neutron detector in this project, Figure 5.3.

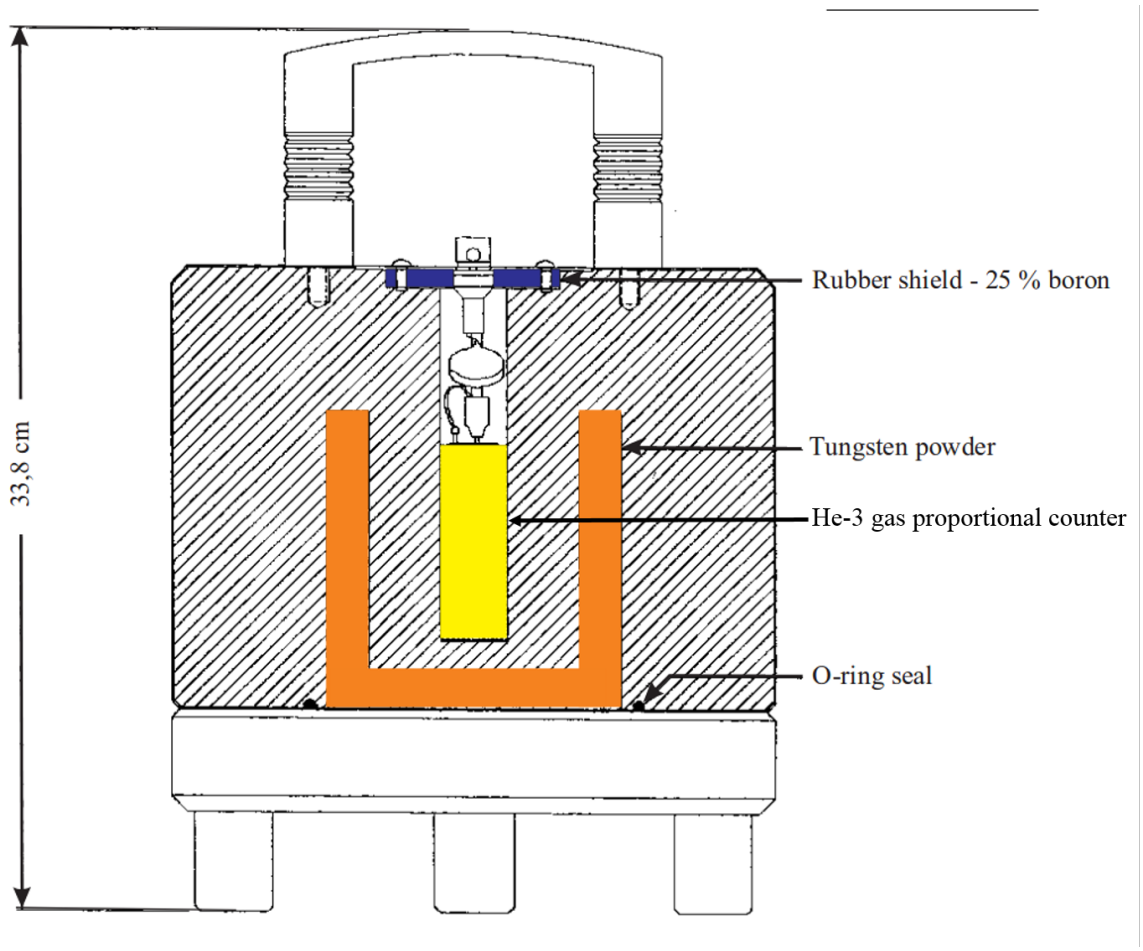

Figure 5.3: Cross sectional view of the neutron detector WENDI-II.

5.4.1 Neutron rem meter

As shown in Figure 5.3, the WENDI-II rem meter is based on the use of a proportional counter filled with He-3 gas situated at the center of a cylindrically shaped polyethylene moderator. The neutron interaction is a (n,p) reaction, Equation 5.3.

$$He^3 + n^1(thermal) - - > H^1 + H^3 + Q \tag{5.3}$$

Inside the polyethylene moderator there is also a shell of tungsten powder. The moderator and the tungsten layer are in pot-shaped form to allow the mounting of the proportional counter through one open side. This side is protected by a small boron doped rubber shield

in order to prevent the over response to low energy neutrons coming from that direction [77]. All components considered, the detector is moderately portable weighing about 13.5 kgs. The detector can be operated in rate meter mode or integrate mode. The latter, with units of Sievert (Sv), was used for all measurements in this project.

Conventionally, rem counters with hydrogen containing moderator alone generally have very low response for neutrons with energies above 10-15 MeV [78]; however, with the addition of the tungsten layer high-energy neutrons can be moderated through spallation reaction, consequently enhancing the response for high-energy neutrons, up to 5 GeV [79]. Figure 5.4 shows the response function of the WENDI-II alongside with the conversion function for the ambient dose equivalent from ICRP-74 [77].

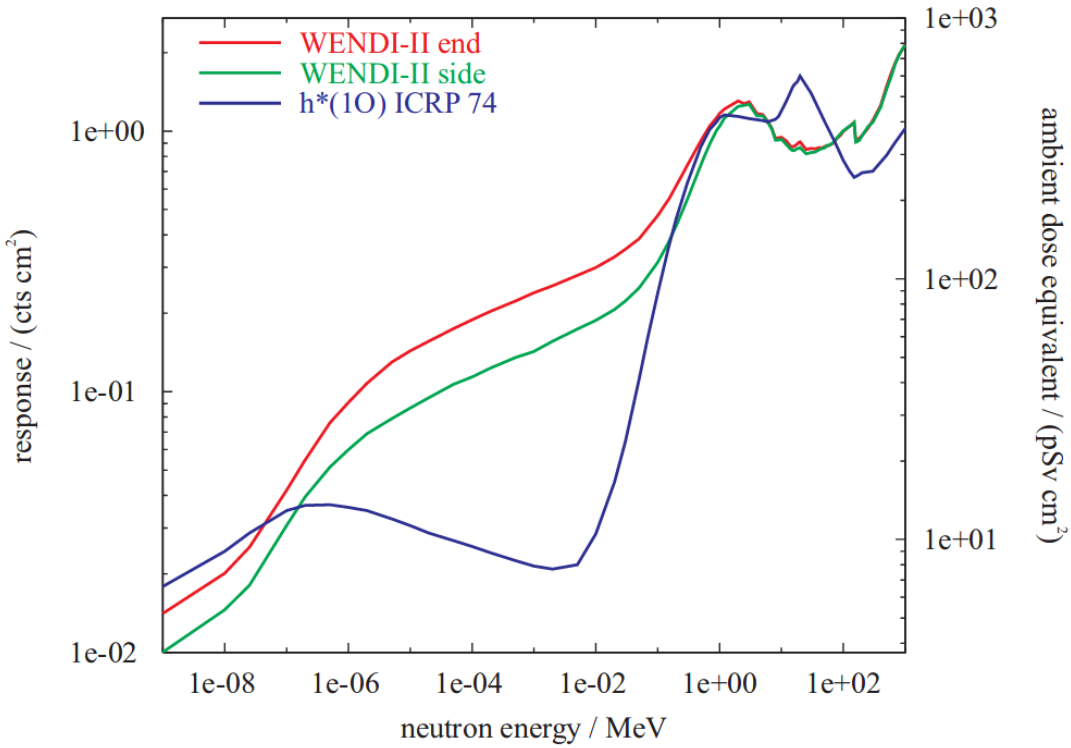

Figure 5.4: Comparison of the response function of the neutron detector WENDI-II and the conversion function for the ambient dose equivalent from ICRP-74.

The response function of WENDI-II agree with $\frac{H^*(10)}{\Phi}$ of the ICRP-74 in the neutron energy region between 0.1-10 MeV, but there is uncertainty in other regions. WENDI-II

overestimates in the energy regions below 0.1 MeV and above 100 MeV, and underestimates in the energy region between 10 and 100 MeV [80]. As a result of this difference between two response functions, we expect significant amount of difference between simulated and measured $H^*(10)$ values. Regardless, the energy response of the WENDI-II is well-balanced and gives ambient neutron dose equivalent directly as the measured output independent of the neutron energy spectrum [81].

5.5 Results and Discussion

5.5.1 Ambient neutron dose equivalent simulation results

The aim of this chapter of the project is to assess secondary neutron production for proton minibeams when a physical collimator has to be used. In this context, the $H^*(10)/D$ at different angles and locations was scored in the simulations.

Without collimation $H^*(10)/D$ varied from 0.0013 mSv/Gy (at θ=135 degrees and 105 cm distance) to 0.242 mSv/Gy (at θ=0 degrees and 11 cm distance). With collimation $H^*(10)/D$ varied from 0.017 (at θ=0 degrees and 105 cm distance) to 3.23 mSv/Gy (at θ=135 degrees and 11 cm distance). This means when brass collimator is introduced, it results in anywhere between 1.5 to 40 times higher $H^*(10)/D$ than without the collimator scenario, Figure 5.5. Without the collimation, most of the neutrons are created at the distal end of the phantom owing to the forward directedness of the secondary neutrons. With the collimation, most of the secondary neutrons are created in the periphery of the collimator.

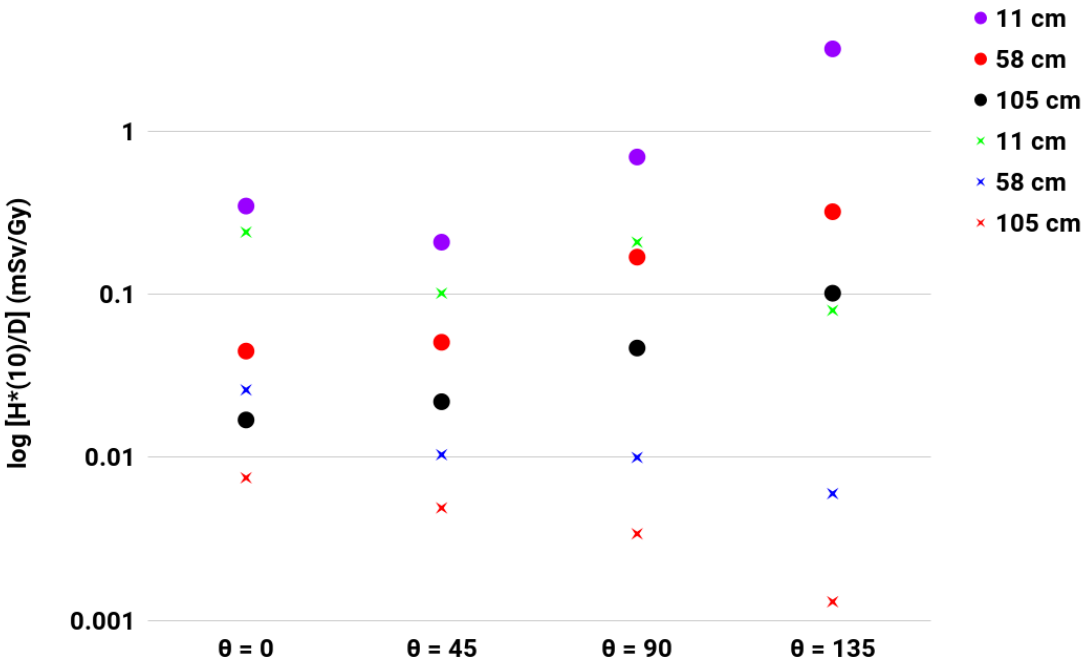

Figure 5.5: Comparison of $H^*(10)/D$ at different distances: 11, 58 and 105 cm from the surfaces of the water phantom and different angles: 0, 45, 90 and 135 degrees with respect to the central axis of the beam. This set of data compares the $H^*(10)/D$ with (circles) and without (crosses) the collimator. When the collimator is in place, it is 3.25 cm thick, 5 cm away from the phantom surface and has 3 mm holes with center-to-center distances of 6 mm.The energy of the proton pencil beam is 120 MeV.

Without the collimator, the neutron dose is in the order of few hundreds of μSv/Gy. This result is in well agreement with the literature for neutrons produced with spot scanned protons [63, 82, 83]. It was already mentioned that with the collimation the system will partially act like passive scattering system. With the collimation, the neutron dose is in the order of few mSv/Gy, resonating with well-established results for neutrons produced with passively scattered protons [60, 61, 63, 84, 85]. Minor differences in results from published work are due to the beamline model, geometry setup, scoring and assumptions differences.

Figure 5.6 compares tungsten and brass collimators of 3.25 cm thickness, 5 cm away from the phantom surface and which have 3 mm holes with center-to-center distances of 6 mm. In the periphery of the collimators, i.e. at angles θ=135 and θ=90 degrees, tungsten produces significantly more neutrons. The $H^*(10)/D$ is almost three times greater

at θ=135 degrees, and almost two times greater at θ=90 degrees than $H^*(10)/D$ produced with brass collimator at all distances. At angles θ=45 and θ=0 degrees, the neutron dose produced by tungsten collimator is less than the brass collimator, suggesting that higher energy and forward-directed neutrons are slowed down in tungsten. Considering that the same thickness brass and tungsten collimators were used for comparison purposes and also remembering that much thinner tungsten is enough to stop 120 MeV protons, it is expected that much of the tungsten collimator material will also serve as a self-shield. Nevertheless, brass must be preferred over the tungsten to decrease the overall dose from secondary neutrons.

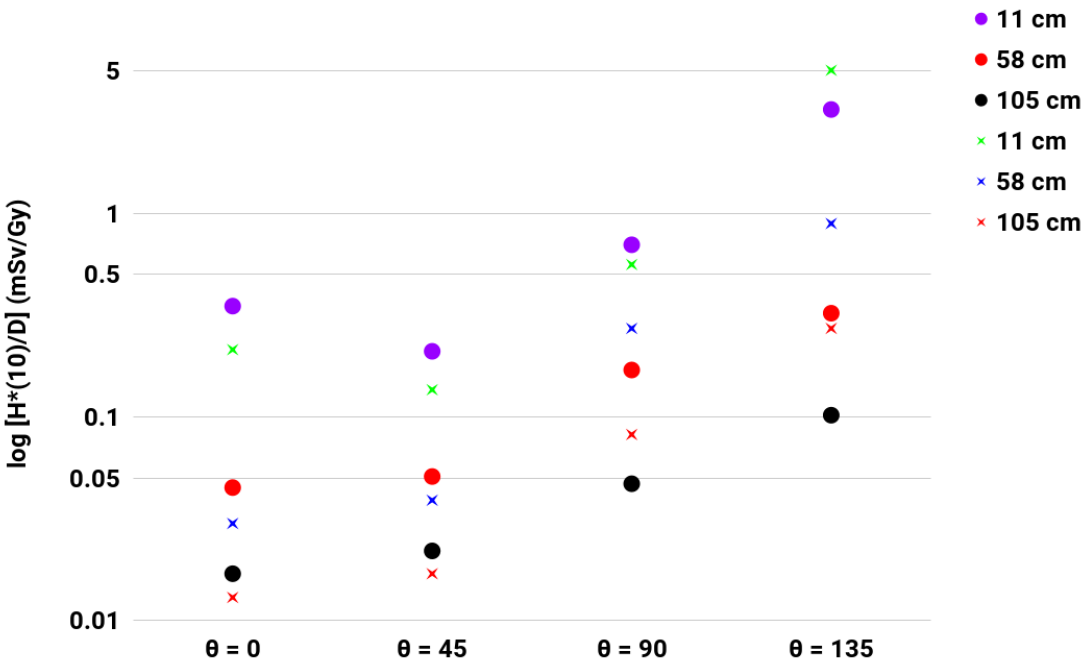

Figure 5.6: Comparison of $H^*(10)/D$ at different distances: 11, 58 and 105 cm from the surfaces of the water phantom and different angles: 0, 45, 90 and 135 degrees with respect to the central axis of the beam. This set of data compares brass (circles) and tungsten (crosses) collimators of 3.25 cm thickness, 5 cm away from the phantom surface and which have 3 mm holes with center-to-center distances of 6 mm. The energy of the proton pencil beam is 120 MeV.

To see the effect of collimator thickness on $H^*(10)/D$, the collimator thickness was doubled from 3.25 cm to 6.5 cm, Figure 5.7. At angles θ=45 and θ=0 degrees, the neutron

dose produced by the thicker collimator is less than the neutron dose produced by the thinner collimator; a very similar result to "brass versus tungsten" case. For the 6.5 cm collimator, high energy neutrons produced in the first half of the collimator are self-shielded in the second half. On the other hand, at angles θ=135 and θ=90 degrees, the neutron doses from the thin and the thick collimator are almost the same, with thicker collimator producing slightly higher neutron dose at farther distances from the water phantom.

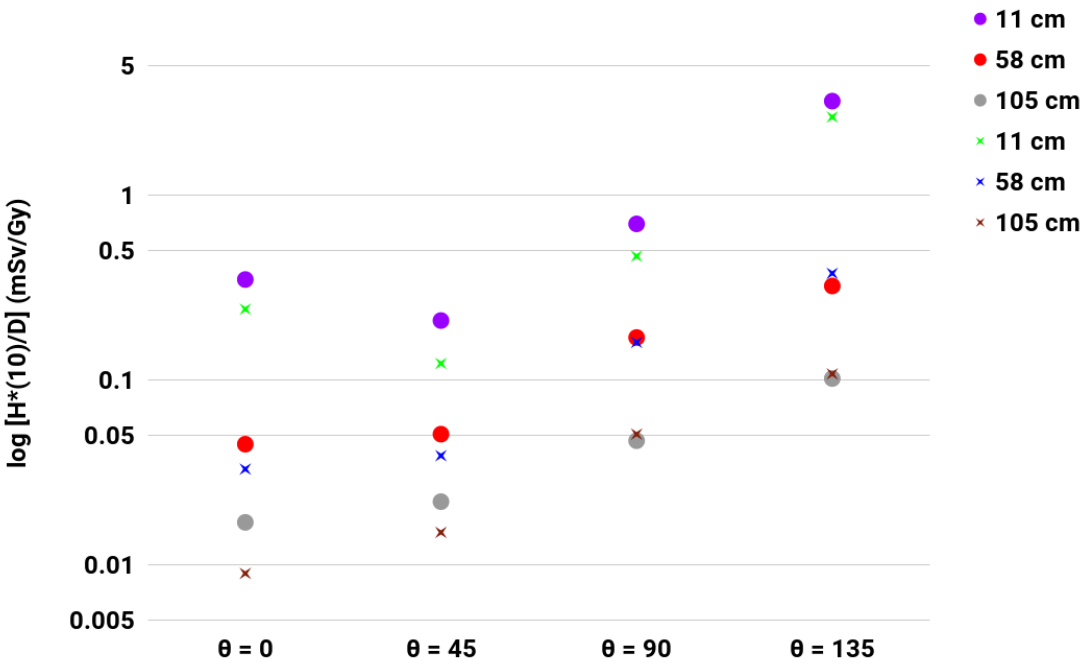

Figure 5.7: Comparison of $H^*(10)/D$ at different distances: 11, 58 and 105 cm from the surfaces of the water phantom and at different angles: 0, 45, 90 and 135 degrees with respect to the central axis of the beam. This set of data compares two brass collimators with different thicknesses: 3.25 cm (circles) and 6.5 cm (crosses), both of which are 5 cm away from the phantom surface and have 3 mm holes with center-to-center distances of 6 mm. The energy of the proton pencil beam is 120 MeV.

Secondary neutron production is not affected drastically by the air gap changes, between the collimator and the water phantom, considered in this project. No extra neutrons are produced, but their distribution is affected by the air gap changes. Changing the air gap from 5 cm to 10 cm resulted in a consistent 20% decrease in $H^*(10)/D$ in the neutron tally volumes closest to the water phantom at all angles, Figure 5.8. This suggests that to

decrease the neutron dose to the patient, the air gap can be increased. At farther away distances, 58 cm and 105 cm from water phantom surface, the $H^*(10)/D$ is almost unchanged with air gap change of 5 cm. At those locations 5 cm change in air gap becomes much smaller than the distance itself.

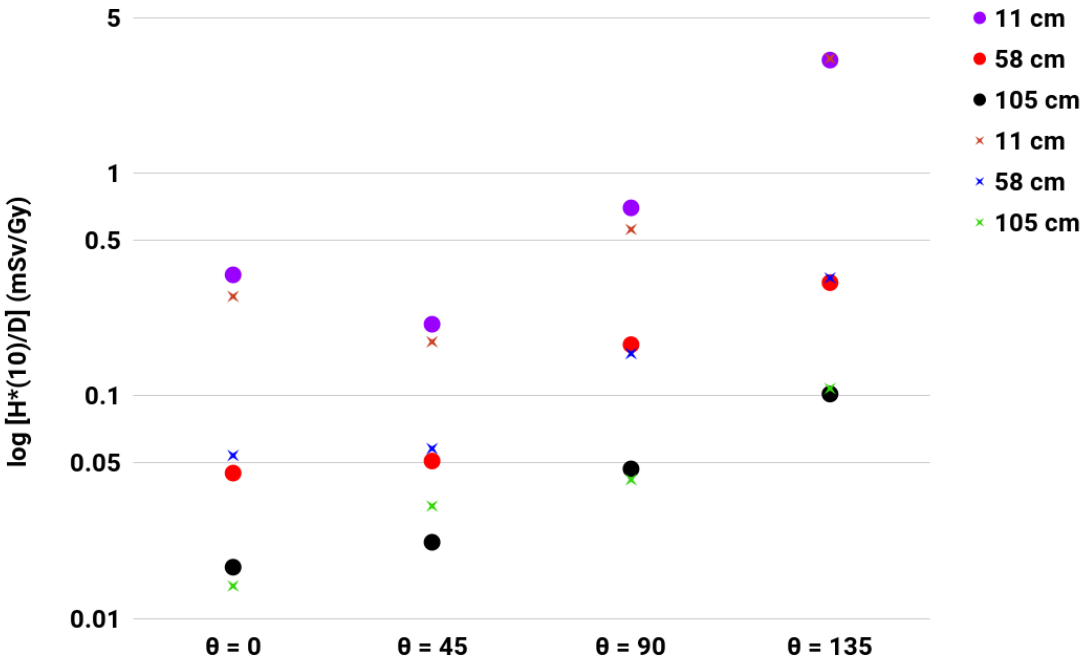

Figure 5.8: Comparison of $H^*(10)/D$ at different distances: 11, 58 and 105 cm from the surfaces of the water phantom and at different angles: 0, 45, 90 and 135 degrees with respect to the central axis of the beam. This set of data is for a brass collimator with 3.25 cm thickness placed at 5 (circles) and 10 (crosses) cm away from the phantom surface and which has 3 mm holes with center-to-center distances of 6 mm. The energy of the proton pencil beam is 120 MeV.

Figure 5.9 compares two brass collimators with 3 mm holes and two different center-to-center (c-t-c) distances: 6 versus 9 mm. Both collimators are 3.25 cm thick and are placed 5 cm away from the phantom surface. There is a consistent increase of 50% in neutron dose at all angles and distances going from 6 mm c-t-c distance to 9 mm c-t-c distance. It was pointed out in Chapter 3 and 4 that increasing the c-t-c distance will result in drop of the proton dose rate. As a result, to deliver the same amount of dose to the target more protons are necessary for 9 mm c-t-c distance scenario than 6 mm c-t-c distance scenario; which in

turn results in higher neutron dose. In addition to that, with holes 6 mm apart, the ratio of the open area (where protons can pass) to closed area (where protons are blocked) is about 51%, whereas with holes 9 mm apart, that ratio is equal to 18%. Consequently, there is more collimator material on protons' path that can produce neutrons.

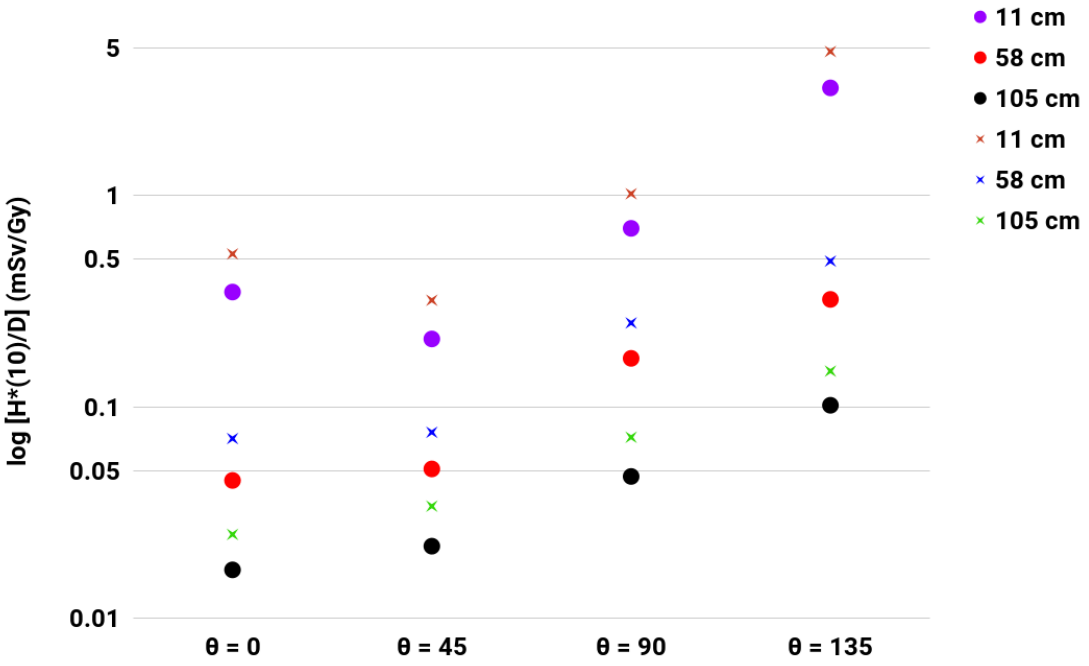

Figure 5.9: Comparison of $H^*(10)/D$ at different distances: 11, 58 and 105 cm from the surfaces of the water phantom and at different angles: 0, 45, 90 and 135 degrees with respect to the central axis of the beam. This set of data compares two brass collimators with 3 mm holes and two different center-to-center distances: 6 mm (circles) and 9 mm (crosses). Collimators are 3.25 cm thick and are placed 5 cm away from the phantom surface. The energy of the proton pencil beam is 120 MeV.

To study the dependence of $H^*(10)/D$ on energy of the primary proton beam, the $H^*(10)/D$ resulting from 120 MeV proton beam impinging on the collimator was compared to $H^*(10)/D$ resulting from 150 MeV proton beam. There is a significant increase, 2-2.5 times, in $H^*(10)/D$ values with 150 MeV proton beam, Figure 5.10, at all angles and locations. This is expected because more energetic protons will produce more neutrons when they undergo nuclear interactions in the collimator material and in the water phantom.

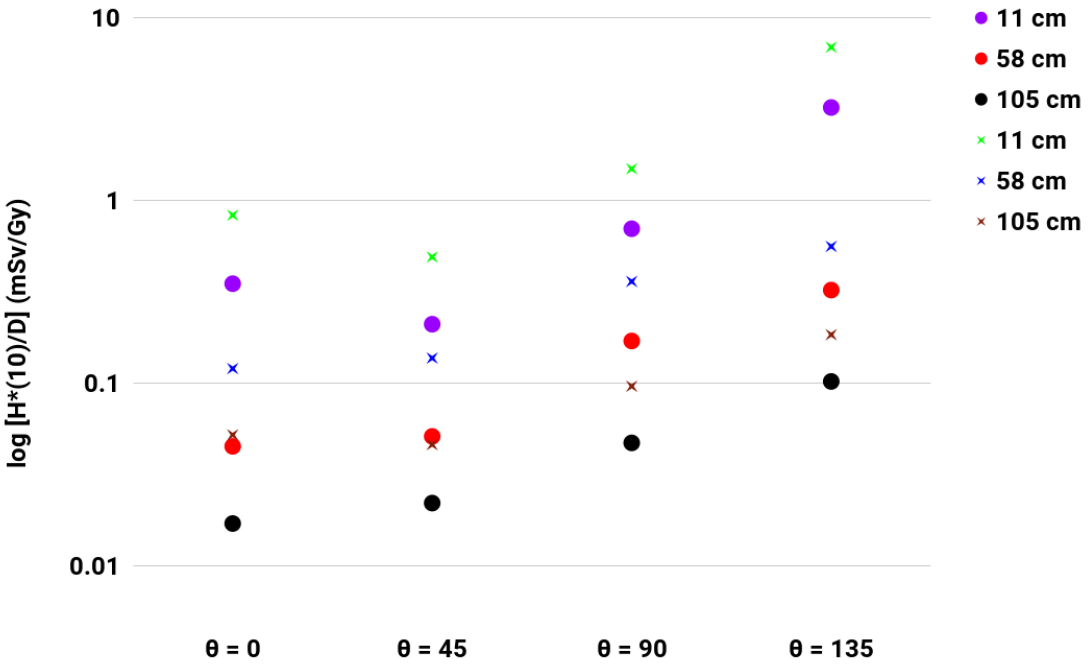

Figure 5.10: Comparison of $H^*(10)/D$ at different distances: 11, 58 and 105 cm from the surfaces of the water phantom and different angles: 0, 45, 90 and 135 degrees with respect to the central axis of the beam. This set of data compares two proton pencil beam energies: 120 MeV (circles) versus 150 MeV (crosses). Brass collimator is 3.25 cm thick, 5 cm away from the phantom surface and has 3 mm holes with center-to-center distances of 6 mm.

Since tumor volumes are not two dimensional, neutrons produced with the depth modulation of the energy of the proton beam is of particular interest in this project. For that reason, a Spread-Out-Bragg-Peak (SOBP) of 4 cm length was simulated with minibeams with energies ranging from 120 to 140 MeV, in increments of 2-3 MeV. The weight factors for each individual energy to achieve +/-3% flatness are the same as provided in Table 3.3. The results obtained for $H^*(10)/D$ values were compared to the results from pristine peak, Figure 5.11.

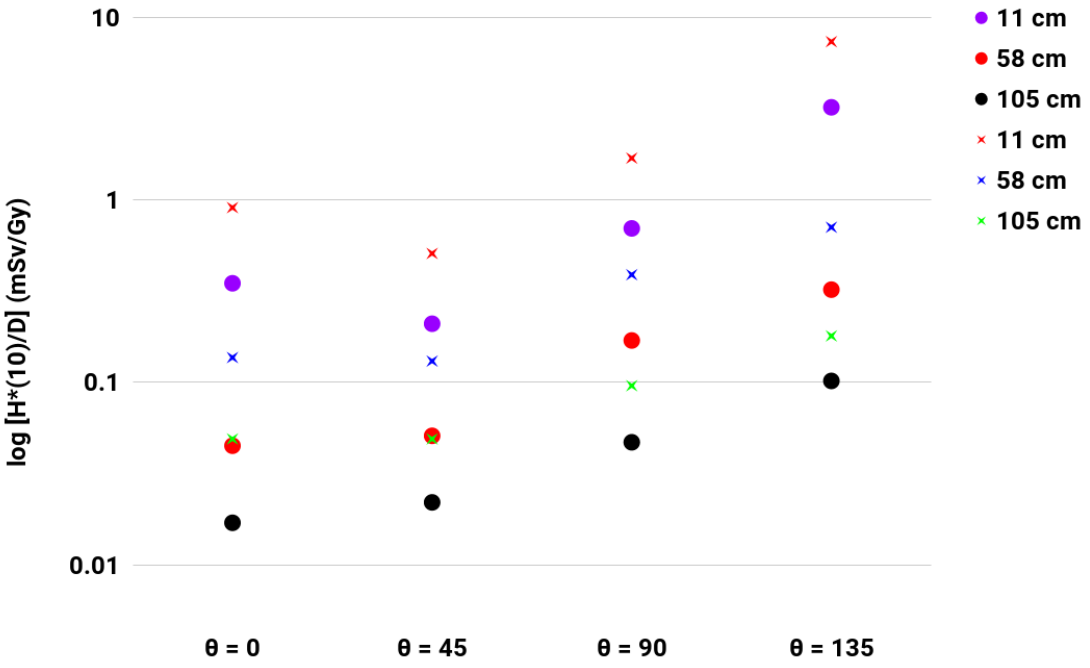

Figure 5.11: Comparison of $H^*(10)/D$ at different distances: 11, 58 and 105 cm from the surfaces of the water phantom and different angles: 0, 45, 90 and 135 degrees with respect to the central axis of the beam. This set of data compares two energy modulation cases: pristine Bragg peak (circles) versus Spread-Out-Bragg-Peak (crosses). Brass collimator is 3.25 cm thick, 5 cm away from the phantom surface and has 3 mm holes with center-to-center distances of 6 mm.

There is a 150% increase in $H^*(10)/D$ values when proton energy has to be modulated to obtain an SOBP as opposed to the pristine Bragg peak. $H^*(10)/D$ results for SOBP case were also compared to published results and reported in Table 5.1.

Table 5.1: Comparison of $H^*(10)/D$ data for SOBP scenario obtained in this project to results obtained by different groups.

Author	Energy (MeV)	Beam delivery method	SOBP width (cm)	Off-axis distance (cm)	$H^*(10)/D$ (mSv/Gy)
this project	140	pencil (with aperture)	4 cm	26 cm	2.63
this project	140	pencil (with aperture)	4 cm	73 cm	0.34
Schneider et al., 2002	177	pencil	10 cm	50 cm	0.12
Zheng et al., 2012	78	uniform	4 cm	35 cm	0.35
Islam, 2013	162	uniform	4 cm	50 cm	3.79
Yan et al., 2002	151	passive	8.2 cm	50 cm	4.8
Polf et al., 2005	160	passive	3 cm	50 cm	3.9

5.5.2 Ambient neutron dose equivalent measurement results

Verification measurements with WENDI-II detector were performed at EPTC. Regardless of the uncertainty issue discussed in section 5.4.1, simulation and measurement results agreed well with each other, with minimum and maximum percent error of 9% and 60% respectively.

Table 5.2: Comparison of $H^*(10)/D$. This set of data compares simulation results to measurement results of $H^*(10)/D$ produced when 120 MeV proton field of size 9x9 cm^2 is incident on 3.25 cm thick brass collimator placed 7 cm away from the phantom surface. Detector is placed at θ=90 degrees, refer to Figure 5.1.

Location	TOPAS			Measurement		
	w/o coll.	with coll.	difference	w/o coll.	with coll.	difference
11 cm	0.21 mSv/Gy	0.7 mSv/Gy	x 3.3	0.113 mSv/Gy	0.96 mSv/Gy	x 8.5
58 cm	0.01 mSv/Gy	0.17 mSv/Gy	x 17	0.0176 mSv/Gy	0.187 mSv/Gy	x 10.6

Table 5.3: Comparison of $H^*(10)/D$. This set of data compares simulation results to measurement results of $H^*(10)/D$ produced when 150 MeV proton field of size 9x9 cm^2 is incident on 3.25 cm thick brass collimator placed 7 cm away from the phantom surface. Detector is placed at θ=90 degrees, refer to Figure 5.1.

Location	TOPAS			Measurement		
	w/o coll.	with coll.	difference	w/o coll.	with coll.	difference
11 cm	0.45 mSv/Gy	1.46 mSv/Gy	x 3.24	0.201 mSv/Gy	1.76 mSv/Gy	x 8.76
58 cm	0.021 mSv/Gy	0.36 mSv/Gy	x 17.1	0.0305 mSv/Gy	0.2 mSv/Gy	x 6.56

In conclusion, the primary goal of this section of the project was to quantify $H^*(10)/D$ due to the secondary neutrons when physical collimator is used to achieve desired minibeams. Investigations suggest that the range for $H^*(10)/D$ values (when the physical collimator is used to collimate broad pencil beam into minibeams) is between 0.009-7.4 mSv/Gy and is strongly dependent on proton energy, c-t-c distance between holes, collimator material, en-

ergy modulation. In this project the field size was set to constant 9 x 9 cm^2; but it should be highlighted that $H^*(10)/D$ value is a very strong function of field size as well. $H^*(10)/D$ values also depend on collimator thickness and air gap but not to that extent as it was in case of the other physical parameters. These values are 20-30 times higher (on average) than the $H^*(10)/D$ values obtained without the collimation. While most of the neutrons are produced in the water phantom itself when no collimation is used, it is not the case with the collimation; the periphery of the collimator gets the most of the neutron dose.

Considering elevated neutron production, high cost and difficult machinery associated with tungsten, brass should be chosen to produce proton minibeams. To further decrease the neutron production, a hybrid collimator can be designed, where the brass part extends just enough to cover the field size and the rest of the collimator is made out of aluminum or nickel.

5.6 Future Work

$H^*(10)$ is an operational quantity and gives a conservative idea about protection quantities. A more thorough work, both computational and experimental, must be done to quantify effective neutron dose using anthropomorphic phantom.

The neutron doses obtained in this work do not cause classic early or late radiation effects; however, even low neutron doses can pose high potential for carcinogenesis. In the absence of relevant high-energy neutron carcinogenesis data and uncertainties associated with the low-dose RBE of the very high-energy neutrons, an estimation study of the secondary cancer risk from neutrons in proton minibeam irradiation should be performed.

CHAPTER 6
CONCLUSIONS

In conclusion, this project investigated, computationally and experimentally, the feasibility of using 2-3 mm proton minibeams for SFRT. The optimal design of the proton minibeam array was based on FOM parameters: PVDR, transmission at Bragg peak and secondary neutron dose. We optimized the proton minibeam design by considering different combinations of parameters: beam energy, beam size (hole diameter), collimator material, c-t-c distance, air gap and collimator thickness. Monte Carlo code TOPAS was used to simulate proton pencil-beams that mimic those available at cyclotron-based clinical facilities and subsequently produced particles. Verification measurements of the PVDRs and the beam transmission using radiochromic films and neutron dose using WENDI-II neutron detector were conducted at two proton therapy facilities: UFPTI and EPTC.

PVDR values of >8 at the entrance and >3 for phantom depths up to 6 cm for 120 MeV proton beams were achieved both in simulations and measurements. PVDR values were affected strongly by changes in c-t-c distance, collimator material and thickness, moderately by changes in hole diameter and weakly by changes is air gap between the collimator and the water phantom. To have higher PVDRs at all depths, increasing the c-t-c distance is suggested. If high PVDRs at shallower depths and more uniform dose, i.e. PVDRs close to unity, is desired, then using thicker collimator made of tungsten is better option. Measurement results of PVDR agree with TOPAS simulation results with percent difference range of 0.5-14% for both UFPTI's IBA and EPTC's ProBeam PBS delivery systems.

Transmission at Bragg peak strongly correlates with dose rate at Bragg peak, if PVDR approaches unity at Bragg peak. Therefore, by simulating and measuring the transmission at Bragg peak we were able to predict the magnitude of the dose rate drop. We concluded that the dose rate at Bragg peak for 120 MeV 3 mm minibeams with c-t-c distance of 6

mm will drop to about 1/5 of the uncollimated dose rate. If 2 mm minibeams are used instead of the 3 mm ones, then the dose rate will drop to 1/10 of the uncollimated dose rate. Transmission is a strong function of mostly two physical parameters used in this project: hole diameter and c-t-c distance; both of which change the ratio of the open to closed area of the collimator. Transmission decreases with smaller hole diameter and larger c-t-c distances. Transmission depends moderately on changes in collimator thickness and weakly on changes in air gap. For the sake of higher dose rate, shorter c-t-c distances and wider hole diameters are suggested. For transmission at Bragg peak, there is about 30% departure of measurement results from the simulation results. Measurement results agree better with simulation results at other depths, signaling that measurement at Bragg peak may have not been successful due to the positioning errors.

Investigations suggest that the range for ambient neutron dose equivalent per proton dose, $H^*(10)/D$, values (when the physical collimator is used to collimate broad pencil beam into minibeams) is between 0.009-7.4 mSv/Gy and is strongly dependent on proton energy, c-t-c distance between holes, collimator material, energy modulation. In this project the field size was set to constant 9 x 9 cm^2; but it should be highlighted that $H^*(10)/D$ value is a very strong function of field size as well. $H^*(10)/D$ values also depend on collimator thickness and air gap but not to that extent as it was in case of the other physical parameters. These values are 20-30 times higher (on average) than the $H^*(10)/D$ values obtained without the collimation. While most of the neutrons are produced in the water phantom itself when no collimation is used, it is not the case with the collimation; the periphery of the collimator gets the most of the neutron dose. Considering elevated neutron production, high cost and difficult machinery associated with tungsten, brass should be chosen to produce proton minibeams. To further decrease the neutron production, a hybrid collimator can be designed, where the brass part extends just enough to cover the field size and the rest of the collimator is made out of aluminum or nickel.

Appendices

APPENDIX A

TOPAS PARAMETER FILE

TOPAS is controlled through the TOPAS Parameter System. In order for a simulation to make sense, the parameter file should have: Overall Control Components, Geometry Components, Particle Sources, Physics list, Scoring tally and optionally Graphics and Time Features Components. TOPAS has default parameters built-in compiled in the code rather than set from a parameter file, so that all users have the same starting point. All positions are set relative to Geometry Components. All time dependent behaviors are controlled through the Time Features system. The order of lines within a parameter file does not matter. A given parameter name may not be defined more than once in a single file. The TOPAS takes a set of ”Parameters Files,” simple text files made up of lines of key/value pairs:

```
Parameter_Type : Parameter_Name = Parameter_Value # Optional comment
```

A Parameter Name can be almost any string, but TOPAS has prefix conventions to keep things clear:

```
Ma/for Materials
El/for Elements
Is/for Isotopes
Ge/for Geometry Components
So/for Particle Sources
Ph/for Physics
Vr/for Variance Reduction
Sc/for Scoring
Gr/for Graphics
```

```
Tf/for Time Features
Ts/for TOPAS overall control
```

The Parameter Type tells TOPAS what type of data will be in this parameter:

```
d for Dimensioned Double
u for Unitless Double
i for Integer
b for Boolean
s for String
dv for Dimensioned Double Vector
similarly for uv,iv,bv and sv
```

An example input is given below:

```
d:Ge/Phantom/HLX           = 10. cm     # Dimensioned Double
u:Ge/Magnet/Dipole/MagneticFieldDirectionX = 1.0        # Unitless
Double
i:Sc/DoseScorer/ZBins                      = 100        # Integer
b:Sc/DoseScorer/Active                     = "True"     # Boolean
s:Ge/Phantom/Material                      = "G4_WATER" # String
dv:Ge/RMW_Track1/Angles = 2 92.2 111.0 deg      # Dimensioned
Double Vector
uv:Ma/Phantom_Plastic/Fractions = 1 0.05549     # Unitless Double
Vector
iv:Gr/Color/yellow         = 3 225 255 0        # Integer Vector
bv:Tf/ScoringOnOff/Values  = 2 "true" "false"   # Boolean Vector
sv:Ma/MyPlastic/Components = 1 "Hydrogen"       # String Vector
```

APPENDIX B

PARAMETER FILE USED IN THIS PROJECT

A geometry input showing how to make a collimator with hexagonal hole arrangement (to be concise only seven perforations are demonstrated):

```
# Collimator hole 1
s:Ge/Hole1/Type              = "TsCylinder"
s:Ge/Hole1/Parent            = "World"
s:Ge/Hole1/Material          = "G4_W"
d:Ge/Hole1/TransX            = 0 mm
d:Ge/Hole1/TransY            = 0 mm
d:Ge/Hole1/TransZ            = -86.25 mm
d:Ge/Hole1/RotX              = 0 deg
d:Ge/Hole1/RotY              = 0 deg
d:Ge/Hole1/RotZ              = 0 deg
d:Ge/Hole1/RMin              = 1.5 mm
d:Ge/Hole1/RMax              = 90 mm
d:Ge/Hole1/HL                = 16.25 mm
d:Ge/Hole1/SPhi              = 0 deg
d:Ge/Hole1/DPhi              = 360 deg
s:Ge/Hole1/Color             = "grey"
s:Ge/Hole1/DrawingStyle      = "FullWireFrame"

# Collimator hole 2
s:Ge/Hole2/Type              = "TsCylinder"
s:Ge/Hole2/Parent            = "Hole1"
```

```
s:Ge/Hole2/Material          = "Air"
d:Ge/Hole2/TransX            = 6 mm
d:Ge/Hole2/TransY            = 0 cm
d:Ge/Hole2/TransZ            = 0 cm
d:Ge/Hole2/RotX              = 0 deg
d:Ge/Hole2/RotY              = 0 deg
d:Ge/Hole2/RotZ              = 0 deg
d:Ge/Hole2/RMin              = 0 mm
d:Ge/Hole2/RMax              = 1.5 mm
d:Ge/Hole2/HL                = 1.625 cm
d:Ge/Hole2/SPhi              = 0 deg
d:Ge/Hole2/DPhi              = 360 deg
s:Ge/Hole2/Color             = "grey"
s:Ge/Hole2/DrawingStyle      = "FullWireFrame"

# Collimator hole 3
s:Ge/Hole3/Type              = "TsCylinder"
s:Ge/Hole3/Parent            = "Hole1"
s:Ge/Hole3/Material          = "Air"
d:Ge/Hole3/TransX            = -6 mm
d:Ge/Hole3/TransY            = 0 cm
d:Ge/Hole3/TransZ            = 0 cm
d:Ge/Hole3/RotX              = 0 deg
d:Ge/Hole3/RotY              = 0 deg
d:Ge/Hole3/RotZ              = 0 deg
d:Ge/Hole3/RMin              = 0 mm
d:Ge/Hole3/RMax              = 1.5 mm
```

```
d:Ge/Hole3/HL                = 1.625 cm
d:Ge/Hole3/SPhi              = 0 deg
d:Ge/Hole3/DPhi              = 360 deg
s:Ge/Hole3/Color             = "grey"
s:Ge/Hole3/DrawingStyle      = "FullWireFrame"

# Collimator hole 4
s:Ge/Hole4/Type              = "TsCylinder"
s:Ge/Hole4/Parent            = "Hole1"
s:Ge/Hole4/Material          = "Air"
d:Ge/Hole4/TransX            = 6 mm
d:Ge/Hole4/TransY            = 10.39230485 mm
d:Ge/Hole4/TransZ            = 0 cm
d:Ge/Hole4/RotX              = 0 deg
d:Ge/Hole4/RotY              = 0 deg
d:Ge/Hole4/RotZ              = 0 deg
d:Ge/Hole4/RMin              = 0 mm
d:Ge/Hole4/RMax              = 1.5 mm
d:Ge/Hole4/HL                = 16.25 mm
d:Ge/Hole4/SPhi              = 0 deg
d:Ge/Hole4/DPhi              = 360 deg
s:Ge/Hole4/Color             = "grey"
s:Ge/Hole4/DrawingStyle      = "FullWireFrame"

# Collimator hole 5
s:Ge/Hole5/Type              = "TsCylinder"
s:Ge/Hole5/Parent            = "Hole1"
```

```
s:Ge/Hole5/Material           = "Air"
d:Ge/Hole5/TransX             = -6 mm
d:Ge/Hole5/TransY             = 10.39230485 mm
d:Ge/Hole5/TransZ             = 0 cm
d:Ge/Hole5/RotX               = 0 deg
d:Ge/Hole5/RotY               = 0 deg
d:Ge/Hole5/RotZ               = 0 deg
d:Ge/Hole5/RMin               = 0 mm
d:Ge/Hole5/RMax               = 1.5 mm
d:Ge/Hole5/HL                 = 16.25 mm
d:Ge/Hole5/SPhi               = 0 deg
d:Ge/Hole5/DPhi               = 360 deg
s:Ge/Hole5/Color              = "grey"
s:Ge/Hole5/DrawingStyle       = "FullWireFrame"

# Collimator hole 6
s:Ge/Hole6/Type               = "TsCylinder"
s:Ge/Hole6/Parent             = "Hole1"
s:Ge/Hole6/Material           = "Air"
d:Ge/Hole6/TransX             = 6 mm
d:Ge/Hole6/TransY             = -10.39230485 mm
d:Ge/Hole6/TransZ             = 0 cm
d:Ge/Hole6/RotX               = 0 deg
d:Ge/Hole6/RotY               = 0 deg
d:Ge/Hole6/RotZ               = 0 deg
d:Ge/Hole6/RMin               = 0 mm
d:Ge/Hole6/RMax               = 1.5 mm
```

```
d:Ge/Hole6/HL                = 16.25 mm
d:Ge/Hole6/SPhi              = 0 deg
d:Ge/Hole6/DPhi              = 360 deg
s:Ge/Hole6/Color             = "grey"
s:Ge/Hole6/DrawingStyle      = "FullWireFrame"

# Collimator hole 7
s:Ge/Hole7/Type              = "TsCylinder"
s:Ge/Hole7/Parent            = "Hole1"
s:Ge/Hole7/Material          = "Air"
d:Ge/Hole7/TransX            = -6 mm
d:Ge/Hole7/TransY            = -10.39230485 mm
d:Ge/Hole7/TransZ            = 0 cm
d:Ge/Hole7/RotX              = 0 deg
d:Ge/Hole7/RotY              = 0 deg
d:Ge/Hole7/RotZ              = 0 deg
d:Ge/Hole7/RMin              = 0 mm
d:Ge/Hole7/RMax              = 1.5 mm
d:Ge/Hole7/HL                = 16.25 mm
d:Ge/Hole7/SPhi              = 0 deg
d:Ge/Hole7/DPhi              = 360 deg
s:Ge/Hole7/Color             = "grey"
s:Ge/Hole7/DrawingStyle      = "FullWireFrame"
```

A source definition input showing how to define a proton spot using phase space parameters (parameters are not accurate):

```
s:So/MyBeam/Type = "Emittance"
s:So/MyBeam/Component = "BeamPosition"
```

```
s:So/MyBeam/BeamParticle = "proton"
s:So/MyBeam/Distribution = "BiGaussian"
d:So/MyBeam/BeamEnergy   =  120 MeV
u:So/MyBeam/BeamEnergySpread   =   0.8
d:So/MyBeam/SigmaX   =   3 mm
u:So/MyBeam/SigmaXPrime   =   0.0048
u:So/MyBeam/CorrelationX    =   0.1578
d:So/MyBeam/SigmaY   =   3 mm
u:So/MyBeam/SigmaYPrime   =   0.0045
u:So/MyBeam/CorrelationY    =   0.3922
```

This block of TOPAS input shows how to set up energies and fluence-to-dose conversion coefficients to calculate the ambient neutron dose equivalent:

```
dv:Sc/scorerAmbDosePerSource9/FluenceToDoseConversionEnergies
= 55
1e-09 1e-08 2.53e-08 1e-07 2e-07 5e-07 1e-06 2e-06 5e-06 1e-05
2e-05 5e-05 1e-04 2e-04 5e-04 1e-03 2e-03 5e-03
1e-02 2e-02 3e-02 5e-02 7e-02 1e-01 1.5e-01 2e-01 3e-01 5e-01
7e-01 9e-01 1 1.2 2 3 4 5 6 7 8 9 10 12 14 15 16
18 20 30 50 75 100 125 150 175 201  MeV
dv:Sc/scorerAmbDosePerSource9/FluenceToDoseConversionValues
= 55
6.6e-10 9e-10 10.6e-10 12.9e-10 13.5e-10 13.6e-10 13.3e-10 12.9e-10
12e-10 11.3e-10 10.6e-10 9.9e-10 9.4e-10
8.9e-10 8.3e-10 7.9e-10 7.7e-10 8e-10 10.5e-10 16.6e-10 23.7e-10
41.1e-10 60e-10 88e-10 132e-10 170e-10
233e-10 322e-10 375e-10 400e-10 416e-10 425e-10 420e-10 412e-10
408e-10 405e-10 400e-10 405e-10 409e-10
```

420e-10 440e-10 480e-10 520e-10 540e-10 555e-10 570e-10 600e-10

515e-10 400e-10 330e-10 285e-10 260e-10

245e-10 250e-10 260e-10 Sv*mm2

REFERENCES

[1] J. A. Laissue, H. Blattmann, and D. N. Slatkin, "Alban khler (1874-1947): Erfinder der gittertherapie", *Zeitschrift fr Medizinische Physik*, vol. 22, no. 2, pp. 90 –99, 2012.

[2] H. P. Bijl, P. van Luijk, R. P. Coppes, J. M. Schippers, A. W. Konings, and A. J. van der Kogel, "Unexpected changes of rat cervical spinal cord tolerance caused by inhomogeneous dose distributions", *International Journal of Radiation Oncology*Biology*Physics*, vol. 57, no. 1, pp. 274 –281, 2003.

[3] A. Bouchet, B. Lemasson, G. L. Duc, C. Maisin, E. Bruer-Krisch, E. A. Siegbahn, L. Renaud, E. Khalil, C. Rmy, C. Poillot, A. Bravin, J. A. Laissue, E. L. Barbier, and R. Serduc, "Preferential effect of synchrotron microbeam radiation therapy on intracerebral 9l gliosarcoma vascular networks", *International Journal of Radiation Oncology*Biology*Physics*, vol. 78, no. 5, pp. 1503 –1512, 2010.

[4] Y. Prezado, G. Jouvion, A. Patriarca, C Nauraye, C. Guardiola, M. Juchaux, C. Lamirault, D. Labiod, L. Jourdain, C. Sébrié, R. Dendale, W. Gonzalez, and F. Pouzoulet, "Proton minibeam radiation therapy widens the therapeutic index for high-grade gliomas", in *Scientific Reports*, 2018.

[5] F. Libeson, "Letter concerning the value of a multi-perforated screen in deep x-ray therapyi", *Radiology*, vol. 22, no. 1, pp. 110–111, 1934.

[6] H. Marks, "Clinical experience with irradiation through a grid", *Radiology*, vol. 58, no. 3, pp. 338–342, 1952, PMID: 14900413.

[7] W. Haring, "Siebstrahlung", *Strahlentherapie*, vol. 51, pp. 154–163, 1934.

[8] E. Schltke, J. Balosso, T. Breslin, G. Cavaletti, V. Djonov, F. Esteve, M. Grotzer, G. Hildebrandt, A. Valdman, and J. Laissue, "Microbeam radiation therapy grid therapy and beyond: A clinical perspective", *The British Journal of Radiology*, vol. 90, no. 1078, p. 20 170 073, 2017, PMID: 28749174.

[9] M. Mohiuddin, J. H. Stevens, J. E. Reiff, M. S. Huq, and N. Suntharalingam, "Spatially fractionated (grid) radiation for palliative treatment of advanced cancer", *Radiation Oncology Investigations*, vol. 4, no. 1, pp. 41–47, 1996.

[10] W. Zeman, H. Curtis, E. Gebhard, and W. Haymaker, "Tolerance of mouse-brain tissue to high-energy deuterons", *Science*, vol. 130, no. 3391, pp. 1760–1761, 1959.

[11] H. P. Bijl, P. van Luijk, R. P. Coppes, J. M. Schippers, A. W. Konings, and A. J. van der Kogel, "Influence of adjacent low-dose fields on tolerance to high doses of protons in rat cervical spinal cord", *International Journal of Radiation Oncology*Biology*Physics*, vol. 64, no. 4, pp. 1204 –1210, 2006.

[12] H. P. Bijl, P. van Luijk, R. P. Coppes, J. M. Schippers, A. W. Konings, and A. J. van der Kogel, "Dose-volume effects in the rat cervical spinal cord after proton irradiation", *International Journal of Radiation Oncology*Biology*Physics*, vol. 52, no. 1, pp. 205 –211, 2002.

[13] J. A. Laissue, S. Bartzsch, H. Blattmann, E. Bruer-Krisch, A. Bravin, D. Dallry, V. Djonov, A. L. Hanson, J. W. Hopewell, B. Kaser-Hotz, J. Keyrilinen, P. P. Laissue, M. Miura, R. Serduc, A. E. Siegbahn, and D. N. Slatkin, "Response of the rat spinal cord to x-ray microbeams", *Radiotherapy and Oncology*, vol. 106, no. 1, pp. 106 –111, 2013.

[14] J. W. Hopewell and K.-R. Trott, "Volume effects in radiobiology as applied to radiotherapy", *Radiotherapy and Oncology*, vol. 56, no. 3, pp. 283 –288, 2000.

[15] G. J. van den Aardweg, J. W. Hopewell, and E. M. Whitehouse, "The radiation response of the cervical spinal cord of the pig: Effects of changing the irradiated volume", *International Journal of Radiation Oncology*Biology*Physics*, vol. 31, no. 1, pp. 51 –55, 1995.

[16] B. E. Powers, H. D. Thames, S. M. Gillette, C. Smith, E. R. Beck, and E. L. Gillette, "Volume effects in the irradiated canine spinal cord: Do they exist when the probability of injury is low?", *Radiotherapy and Oncology*, vol. 46, no. 3, pp. 297 –306, 1998.

[17] B. Jolles, "The study of connective-tissue reaction to radiation. the sieve or chess method", *British Journal of Cancer*, vol. 3, no. 1, pp. 27 –31, 1949.

[18] H. Shirato, M. Mizuta, and K. Miyasaka, "A mathematical model of the volume effect which postulates cell migration from unirradiated tissues", *Radiotherapy and Oncology*, vol. 35, no. 3, pp. 227 –231, 1995.

[19] R. J. Yaes and A. Kalend, "Local stem cell depletion model for radiation myelitis", *International Journal of Radiation Oncology*Biology*Physics*, vol. 14, no. 6, pp. 1247 –1259, 1988.

[20] E. C. Mackonis, N Suchowerska, M Zhang, M Ebert, D. R. McKenzie, and M Jackson, "Cellular response to modulated radiation fields", *Physics in Medicine and Biology*, vol. 52, no. 18, pp. 5469–5482, Aug. 2007.

[21] A. Bouchet, R. Serduc, J. A. Laissue, and V. Djonov, "Effects of microbeam radiation therapy on normal and tumoral blood vessels", *Physica Medica*, vol. 31, no. 6, pp. 634 –641, 2015, Radiation Therapy with Synchrotron Radiation: Achievements and Challenges.

[22] A. Bouchet, B. Lemasson, G. L. Duc, C. Maisin, E. Bruer-Krisch, E. A. Siegbahn, L. Renaud, E. Khalil, C. Rmy, C. Poillot, A. Bravin, J. A. Laissue, E. L. Barbier, and R. Serduc, "Preferential effect of synchrotron microbeam radiation therapy on intracerebral 9l gliosarcoma vascular networks", *International Journal of Radiation Oncology*Biology*Physics*, vol. 78, no. 5, pp. 1503 –1512, 2010.

[23] P. P. M. I. A. S. P. A. W. R. Yuqing Yang Jeffrey C. Crosbie, "In vitro study of genes and molecular pathways differentially regulated by synchrotron microbeam radiotherapy", *Radiation Research*, vol. 182, pp. 182 –182 –14, 2014.

[24] A. Bouchet, N. Sakakini, M. E. Atifi, C. Le Clec'h, E. Bruer-Krisch, L. Rogalev, J. A. Laissue, P. Rihet, G. Le Duc, and L. Pelletier, "Identification of areg and plk1 pathway modulation as a potential key of the response of intracranial 9l tumor to microbeam radiation therapy", *International Journal of Cancer*, vol. 136, no. 11, pp. 2705–2716,

[25] D. N. Slatkin, P. Spanne, F. A. Dilmanian, and M. Sandborg, "Microbeam radiation therapy", *Medical Physics*, vol. 19, no. 6, pp. 1395–1400, 1992.

[26] A. Fuchs, B. Ren, E. M. Rosen, F. A. Dilmanian, F. P. Recksiek, G. Le Duc, J. A. Niederer, J. Tammam, J. A. Smith, J. Kalef-Ezra, L. A. Pena, M. M. Nawrocky, N. Zhong, P. L. Micca, P. M. Farmer, S. R. Martinez, T. M. Button, and T. Bacarian, "Response of rat intracranial 9l gliosarcoma to microbeam radiation therapy", *Neuro-Oncology*, vol. 4, no. 1, pp. 26–38, Jan. 2002.

[27] F. A. Dilmanian, Z. Zhong, T. Bacarian, H. Benveniste, P. Romanelli, R. Wang, J. Welwart, T. Yuasa, E. M. Rosen, and D. J. Anschel, "Interlaced x-ray microplanar beams: A radiosurgery approach with clinical potential", *Proceedings of the National Academy of Sciences*, vol. 103, no. 25, pp. 9709–9714, 2006. eprint: `https://www.pnas.org/content/103/25/9709.full.pdf`.

[28] J. A. O. Z. Z. J. Y. P. N. R. D. S. S. G. R. F. C. R. M. M. M. S. D. H. L. T. S. A. N. S. P. K. C. A. G. M. M. K. O. F. Avraham Dilmanian Arthur L. Jenkins, "X-ray microbeam irradiation of the contusion-injured rat spinal cord temporarily improves hind-limb function", *Radiation Research*, vol. 179, pp. 179 –179 –13, 2012.

[29] Y. Prezado, S. Sarun, S. Gil, P. Deman, A. Bouchet, and G. Le Duc, "Increase of lifespan for glioma-bearing rats by using minibeam radiation therapy", *Journal of Synchrotron Radiation*, vol. 19, no. 1, pp. 60–65, Jan. 2012.

[30] M. Kodowska, P. Olko, and M. Waligrski, "Proton microbeam radiotherapy with scanned pencil-beams monte carlo simulations", *Physica Medica*, vol. 31, no. 6, pp. 621 –626, 2015, Radiation Therapy with Synchrotron Radiation: Achievements and Challenges.

[31] O. Zlobinskaya, S. Girst, C. Greubel, V. Hable, C. Siebenwirth, D. W. M. Walsh, G. Multhoff, J. J. Wilkens, T. E. Schmid, and G. Dollinger, "Reduced side effects by proton microchannel radiotherapy: Study in a human skin model", *Radiation and Environmental Biophysics*, vol. 52, no. 1, pp. 123–133, Mar. 2013.

[32] Y. Prezado and G. R. Fois, "Proton-minibeam radiation therapy: A proof of concept", *Medical Physics*, vol. 40, no. 3, p. 031 712,

[33] F. A. Dilmanian, J. G. Eley, and S. Krishnan, "Minibeam therapy with protons and light ions: Physical feasibility and potential to reduce radiation side effects and to facilitate hypofractionation", *International Journal of Radiation Oncology*Biology*Physics*, vol. 92, no. 2, pp. 469 –474, 2015.

[34] C. Peucelle, C. Nauraye, A. Patriarca, E. Hierso, N. Fournier-Bidoz, I. Martnez-Rovira, and Y. Prezado, "Proton minibeam radiation therapy: Experimental dosimetry evaluation", *Medical Physics*, vol. 42, no. 12, pp. 7108–7113, 2015.

[35] H. D. e. a. Prezado Y Jouvion G, "Proton minibeam radiation therapy spares normal rat brain: Long-term clinical, radiological and histopathological analysis", *Scientific Reports*, vol. 7, no. 1, p. 14 403, 2017.

[36] J. L. Fair, "Spatially fractionated proton therapy: a monte carlo verification", Master's thesis, Georgia Institute of Technology, Atlanta, USA, 2016.

[37] M. Gao, M. M. Mohiuddin, W. F. Hartsell, and M. Pankuch, "Spatially fractionated (grid) radiation therapy using proton pencil beam scanning (pbs): Feasibility study and clinical implementation", *Medical Physics*, vol. 45, no. 4, pp. 1645–1653, 2018.

[38] T. Henry, A. Ureba, A. Valdman, and A. Siegbahn, "Proton grid therapy: A proof-of-concept study", *Technology in Cancer Research & Treatment*, vol. 16, no. 6, pp. 749–757, 2017, PMID: 28592213.

[39] J. B. Farr, V. Moskvin, R. C. Lukose, S. Tuomanen, P. Tsiamas, and W. Yao, "Development, commissioning, and evaluation of a new intensity modulated minibeam proton therapy system", *Medical Physics*, vol. 45, no. 9, pp. 4227–4237, 2018.

[40] S. Charyyev, C. Wang, and G. Szalkowski, "Scientific abstracts and sessions", *Medical Physics*, vol. 45, no. 6, e488, 2018. eprint: `https://aapm.onlinelibrary.wiley.com/doi/pdf/10.1002/mp.12938`.

[41] L. De marzi, A. Patriarca, C. Nauraye, E. Hierso, R. Dendale, C Guardiola, and Y. Prezado, "Implementation of planar proton minibeam radiation therapy using a pencil beam scanning system: A proof of concept study", *Medical Physics*, vol. 45, Sep. 2018.

[42] J. Meyer, J. Eley, T. E. Schmid, S. E. Combs, R. Dendale, and Y. Prezado, "Spatially fractionated proton minibeams", *The British Journal of Radiology*, vol. 92, no. 1095, p. 20 180 466, 2019, PMID: 30359081.

[43] J. Perl, J. Shin, J. Schmann, B. Faddegon, and H. Paganetti, "Topas: An innovative proton monte carlo platform for research and clinical applications", *Medical Physics*, vol. 39, no. 11, pp. 6818–6837, 2012.

[44] L. Lin, S. Huang, M. Kang, P. Hiltunen, R. Vanderstraeten, J. Lindberg, S. Siljamaki, T. Wareing, I. Davis, A. Barnett, J. McGhee, C. B. Simone II, T. D. Solberg, J. E. McDonough, and C. Ainsley, "A benchmarking method to evaluate the accuracy of a commercial proton monte carlo pencil beam scanning treatment planning system", *Journal of Applied Clinical Medical Physics*, vol. 18, no. 2, pp. 44–49, 2017.

[45] L. Lin, M. Kang, T. D. Solberg, C. G. Ainsley, and J. E. McDonough, "Experimentally validated pencil beam scanning source model in TOPAS", *Physics in Medicine and Biology*, vol. 59, no. 22, pp. 6859–6873, Oct. 2014.

[46] S. Huang, M. Kang, K. Souris, C. Ainsley, T. D. Solberg, J. E. McDonough, C. B. Simone II, and L. Lin, "Validation and clinical implementation of an accurate monte carlo code for pencil beam scanning proton therapy", *Journal of Applied Clinical Medical Physics*, vol. 19, no. 5, pp. 558–572, 2018.

[47] E. Courant and H. Snyder, "Theory of the alternating-gradient synchrotron", *Annals of Physics*, vol. 3, no. 1, pp. 1 –48, 1958.

[48] M. Fuss, E. Sturtewagen, C. D. Wagter, and D. Georg, "Dosimetric characterization of GafChromic EBT film and its implication on film dosimetry quality assurance", *Physics in Medicine and Biology*, vol. 52, no. 14, pp. 4211–4225, Jun. 2007.

[49] P. Deman, M. Vautrin, M. Edouard, V. Stupar, L. Bobyk, R. Farion, H. Elleaume, C. Rmy, E. L. Barbier, F. Estve, and J.-F. Adam, "Monochromatic minibeams radiotherapy: From healthy tissue-sparing effect studies toward first experimental glioma bearing rats therapy", *International Journal of Radiation Oncology*Biology*Physics*, vol. 82, no. 4, e693 –e700, 2012.

[50] L. Zhao and I. J. Das, "Gafchromic EBT film dosimetry in proton beams", *Physics in Medicine and Biology*, vol. 55, no. 10, N291–N301, Apr. 2010.

[51] T. Henry, N. Bassler, A. Ureba, T. Tsubouchi, A. Valdman, and A. Siegbahn, "Development of an interlaced-crossfiring geometry for proton grid therapy", *Acta Oncologica*, vol. 56, no. 11, pp. 1437–1443, 2017, PMID: 28826311.

[52] M. Sammer, C. Greubel, S. Girst, and G. Dollinger, "Optimization of beam arrangements in proton minibeam radiotherapy by cell survival simulations", *Medical Physics*, vol. 44, no. 11, pp. 6096–6104, 2017.

[53] ICRU, "Prescribing, recording and reporting photon beam therapy", ICRU, 50, 1993.

[54] ——, "Prescribing, recording and reporting photon beam therapy", ICRU, 1999, Supplement to Report 50.

[55] G. Szalkowski, C. Wang, and S. Charyyev, "Scientific abstracts and sessions", *Medical Physics*, vol. 45, no. 6, e614, 2018. eprint: `https://aapm.onlinelibrary.wiley.com/doi/pdf/10.1002/mp.12938`.

[56] M. Artz, "Development of a patient machine time model to evaluate dose perturbation by respiratory tumor motion in pencil beam scanning proton radiation therapy", PhD thesis, University of Tennessee, Knoxville, USA, 2016.

[57] M. C. S. Gottschalk B Koehler A M and W. M. S, "Proton beam technology: Slit scattering and penumbra", *Proton Therapy Co-Operative Group XX Meeting (Abstract)*, 1994.

[58] A. Patriarca, C. Fouillade, M. Auger, F. Martin, F. Pouzoulet, C. Nauraye, S. Heinrich, V. Favaudon, S. Meyroneinc, R. Dendale, A. Mazal, P. Poortmans, P. Verrelle, and L. D. Marzi, "Experimental set-up for flash proton irradiation of small animals using a clinical system", *International Journal of Radiation Oncology*Biology*Physics*, vol. 102, no. 3, pp. 619 –626, 2018.

[59] W. D. Newhauser and R. Zhang, "The physics of proton therapy", *Physics in Medicine and Biology*, vol. 60, no. 8, R155–R209, Mar. 2015.

[60] Y. Zheng, J. Fontenot, P. Taddei, D. Mirkovic, and W. Newhauser, "Monte carlo simulations of neutron spectral fluence, radiation weighting factor and ambient dose equivalent for a passively scattered proton therapy unit", *Physics in Medicine and Biology*, vol. 53, no. 1, pp. 187–201, Dec. 2007.

[61] P. Binns and J. Hough, "Secondary dose exposures during 200 mev proton therapy", *Radiation Protection Dosimetry*, vol. 70, no. 1-4, pp. 441–444, Apr. 1997.

[62] S. Agosteo, C. Birattari, M Caravaggio, M. Silari, and G. Tosi, "Secondary neutron and photon dose in proton therapy.", *Radiotherapy and oncology : Journal of the*

European Society for Therapeutic Radiology and Oncology, vol. 48 3, pp. 293–305, 1998.

[63] U. Schneider, S. Agosteo, E. Pedroni, and J. Besserer, "Secondary neutron dose during proton therapy using spot scanning", *International Journal of Radiation Oncology*Biology*Physics*, vol. 53, no. 1, pp. 244 –251, 2002.

[64] J. C. Polf and W. D. Newhauser, "Calculations of neutron dose equivalent exposures from range-modulated proton therapy beams", *Physics in Medicine and Biology*, vol. 50, no. 16, pp. 3859–3873, Aug. 2005.

[65] J. Fontenot, P. Taddei, Y. Zheng, D. Mirkovic, T. Jordan, and W. Newhauser, "Equivalent dose and effective dose from stray radiation during passively scattered proton radiotherapy for prostate cancer", *Physics in Medicine and Biology*, vol. 53, no. 6, pp. 1677–1688, Feb. 2008.

[66] G. Mesoloras, G. A. Sandison, R. D. Stewart, J. B. Farr, and W. C. Hsi, "Neutron scattered dose equivalent to a fetus from proton radiotherapy of the mother", *Medical Physics*, vol. 33, no. 7Part1, pp. 2479–2490,

[67] U. Schneider, R. A. Hlg, G. Baiocco, and T. Lomax, "Neutrons in proton pencil beam scanning: Parameterization of energy, quality factors and RBE", *Physics in Medicine and Biology*, vol. 61, no. 16, pp. 6231–6242, Aug. 2016.

[68] B. R. Smith, D. E. Hyer, P. M. Hill, and W. S. Culberson, "Secondary neutron dose from a dynamic collimation system during intracranial pencil beam scanning proton therapy: A monte carlo investigation", *International Journal of Radiation Oncology Biology Physics*, vol. 103, no. 1, pp. 241–250, Jan. 2019.

[69] M. R. Islam, "Study of secondary neutrons from uniform scanning proton beams by means of experiment and simulation", PhD thesis, Oklahoma State University, Stillwater, USA, 2013.

[70] S. Trinkl, V. Mares, F. S. Englbrecht, J. J. Wilkens, M. Wielunski, K. Parodi, W. Rhm, and M. Hillbrand, "Systematic out-of-field secondary neutron spectrometry and dosimetry in pencil beam scanning proton therapy", *Medical Physics*, vol. 44, no. 5, pp. 1912–1920, 2017.

[71] D. J. Brenner and E. J. Hall, "Secondary neutrons in clinical proton radiotherapy: A charged issue", *Radiotherapy and Oncology*, vol. 86, no. 2, pp. 165 –170, 2008.

[72] Y. A. van Grenou, "Monte carlo simulations of neutron doses from pencil beam scanning proton therapy", Master's thesis, University of Bergen, Bergen, Norway, 2017.

[73] S. Park and J. Kang, "Basics of particle therapy i: Physics", *Radiat Oncol J.*, vol. 29, no. 3, pp. 135 –146, 2011.

[74] ICRP, "1990 recommendations of the international commission on radiological protection", ICRP, 21, 1991.

[75] ——, "Conversion coefficients for use in radiological protection against external radiation", ICRP, 74, 1996.

[76] P. Rodrigues, A. Trindade, L. Peralta, C. Alves, A. Chaves, and M. Lopes, "Application of geant4radiation transport toolkit to dose calculations in anthropomorphic phantoms", *Applied Radiation and Isotopes*, vol. 61, no. 6, pp. 1451 –1461, 2004.

[77] F. Gutermuth, T. Radon, G. Fehrenbacher, and R. Siekmann, "Test of the rem-counter wendi-ii from eberline in different energy-dispersed neutron fields.", *EXT-2004-085*, 2004.

[78] Y.-C. Lin, C.-C. Lee, T.-C. Chao, and H.-Y. Tsai, "Ambient neutron dose equivalent during proton therapy using wobbling scanning system: Measurements and calculations", *Radiation Physics and Chemistry*, vol. 140, pp. 290 –294, 2017, 2nd International Conference on Dosimetry and its Applications (ICDA-2) University of Surrey, Guildford, United Kingdom, 3-8 July 2016.

[79] O. R.H., H. H.H., B. A., K. J.H., C. W.H., V. D.G., and D. R.T., "Wendi: An improved neutron rem meter.", *Health Phys.*, vol. 79, no. 2, pp. 170–81, 2000.

[80] S. Yonai, N. Matsufuji, T. Kanai, Y. Matsui, K. Matsushita, H. Yamashita, M. Numano, T. Sakae, T. Terunuma, T. Nishio, R. Kohno, and T. Akagi, "Measurement of neutron ambient dose equivalent in passive carbon-ion and proton radiotherapies", *Medical Physics*, vol. 35, no. 11, pp. 4782–4792, 2008.

[81] Y. Zheng, Y. Liu, O. Zeidan, A. N. Schreuder, and S. Keole, "Measurements of neutron dose equivalent for a proton therapy center using uniform scanning proton beams", *Medical Physics*, vol. 39, no. 6Part1, pp. 3484–3492, 2012.

[82] C. Geng, M. Moteabbed, J. Seco, Y. Gao, X. G. Xu, J. Ramos-Méndez, B. Faddegon, and H. Paganetti, "Dose assessment for the fetus considering scattered and secondary radiation from photon and proton therapy when treating a brain tumor of the mother", *Physics in Medicine and Biology*, vol. 61, no. 2, pp. 683–695, 2015.

[83] X. Wang, F. Poenisch, N. Sahoo, R. X. Zhu, M. Lii, M. T. Gillin, J. Li, and D. Grosshans, "Spot scanning proton therapy minimizes neutron dose in the setting of radiation therapy administered during pregnancy", *Journal of Applied Clinical Medical Physics*, vol. 17, no. 5, pp. 366–376, 2016.

[84] R. M. Howell and E. A. Burgett, “Secondary neutron spectrum from 250-mev passively scattered proton therapy: Measurement with an extended-range bonner sphere system”, *Medical Physics*, vol. 41, no. 9, 2014.

[85] S.-E. Han, G. Cho, and S. B. Lee, “An assessment of the secondary neutron dose in the passive scattering proton beam facility of the national cancer center”, *Nuclear Engineering and Technology*, vol. 49, no. 4, pp. 801 –809, 2017.